# Engineering Aspects of Terahertz Time-Domain Spectroscopy

by

**Withawat Withayachumnankul**

B Eng (Electronic Engineering, Honours)
King Mongkut's Institute of Technology Ladkrabang, Thailand, 2001

M Eng (Electronic Engineering)
King Mongkut's Institute of Technology Ladkrabang, Thailand, 2003

Thesis submitted for the degree of

**Doctor of Philosophy**

in

School of Electrical & Electronic Engineering
Faculty of Engineering, Computer & Mathematical Sciences
The University of Adelaide, Australia

December, 2009

Chapter 6

# Classification of THz-TDS Signals with Subtle Features

TERAHERTZ or T-ray signals obtained from THz-TDS carry information on the optical properties of a given sample under test. Thus, the signals can be useful in classification, recognition, and characterisation of materials. Many materials exhibit distinctive spectral responses, which are often easily recognisable. However, among similar samples, such as biological samples, which are lacking in distinct T-ray spectral features, differences in the characteristic signals are subtle and thus do not lend themselves to simple discrimination. Hence, the introduction of machine learning to automated classification of T-ray data is called for. This chapter investigates the possibility of applying support vector machines (SVMs) to classification of biological samples via their response to T-rays. To reduce the large number of classification features, wavelet coefficients representing the signals are selected as an input to the classifier.

## 6.1 Introduction

A typical THz-TDS system can be used in the application of material characterisation. Furthermore, the data obtainable from the system can also be useful for classification and recognition of materials. A number of experiments have demonstrated the use of T-ray pulses for the classification of gases (Jacobsen *et al.* 1996, Lin *et al.* 2007), chemical substances (Fischer *et al.* 2005b), biological tissue (Löffler *et al.* 2002), etc., which may be hidden beneath an optically-opaque barrier, yet penetrable by T-rays. Often, target materials produce T-ray spectral responses that have unique fingerprints due to molecular rotational or vibrational transitions, allowing simple classification via pattern matching.

In many cases, materials under study do not exhibit distinctive spectral features. Examples are large biomolecules, such as DNA and RNA (Fischer *et al.* 2005c), the vibrational modes of which are affected by the inhomogeneity of the sample and the high density of the modes (Markelz 2008). This prohibits a direct detection of the presence of molecules. In this chapter, supervised machine learning is introduced to the classification of biological samples.

Even though several hundred classification features are available directly from T-ray signals, the use of so many features should be avoided in the task of classification, due to what is known as the *curse of dimensionality* (Bellman 1961). A compact representation of the signal is important in improving the classification accuracy and generalisation capability, and in reducing the calculation complexity. Wavelet multiresolution analysis is very suitable in this regard, because the wavelet transform of a pulsed T-ray signal results in a compact set of coefficients. In this work, many mother wavelets and decomposition levels are trialled to find the best representation for a given set of signals. In order to lessen the influence of the model selection on the classification accuracy, support vector machines (SVMs), which are virtually self-optimising, are adopted for the task of classification.

The chapter is organised as follows. Previous work relevant to the applications of the wavelet transform to T-ray signals is reviewed in Section 6.3. The properties of wavelets that are favourable in the classification of T-ray signals are discussed in Section 6.4. The principle of SVMs, along with a scheme to assess the accuracy, are briefly covered in Section 6.5. Data acquisition for THz-TDS is explained in Section 6.6. In

Section 6.7 the classification results are reported. Further analysis of the results is presented in Section 6.8.

## 6.2 Research objective and framework

### Objective

To demonstrate the feasibility of using supervised machine learning for classification of T-ray signals that contain broad rather than distinct spectral features. The classification features that we exploit are the wavelet coefficients of T-ray signals, and the classifiers are linear-kernel SVMs. The wavelet transform of a measured T-ray signal is known to provide a compact yet informative feature set, suitable for the classification problem.

### Framework

T-ray signals are obtained from THz-TDS with transmission-mode measurements. The employed mother wavelets are limited to a series of Daubechies, Symlets, Coiflets, and Biorthogonal wavelets. The classifiers used in this work are linear-kernel SVMs, which rely on supervised learning. The available dataset is relatively small, compared to the number of features.

## 6.3 Applications of wavelets to T-ray signals

Although THz-TDS is relatively new, many applications of wavelets to T-ray signals obtained from THz-TDS have been suggested. Mittleman *et al.* (1996) described the similarity between wavelets and T-ray waveforms, and demonstrated the feasibility of using wavelet compression for compressing T-ray data. They further suggested using wavelet transforms for rapid parameter extraction and multiresolution analysis of T-ray signals. Handley *et al.* (2002) determined the maximum compressible level of wavelet compression that has no substantial impact on optical parameters extracted from the compressed T-ray signals. Interestingly, it was found that significant information is still preserved with only 20% of the wavelet coefficients.

Mittleman *et al.* (1998) discussed an application of the multiresolution analysis to denoising T-ray signals, and showed the superiority of the analysis to a parabolic Fourier

filter. Ferguson and Abbott (2001b) and Ferguson and Abbott (2001a) tested a wavelet denoising technique with T-ray signals, particularly when they are strongly absorbed by a biological sample. Soft-thresholding wavelet denoising can improve the SNRs of the signals at the maximum of 10 dB when the fourth-order Coiflet wavelet is used.

Handley *et al.* (2004) exploited wide-band cross ambiguity functions (WBCAFs) for estimating the absorption coefficient and refractive indices of materials. For the transformation, instead of using a regular wavelet, a WBCAF adopts an arbitrary signal, in this case the reference T-ray pulse, as a mother function. One major disadvantage arises from the uncertainty principle of the representation. Wavelets and WBCAFs are localised in neither the time nor frequency domain, and thus the material parameters that are frequency-dependent are not accessible using such a representation. In addition, Handley *et al.* (2004) describe a wavelet analysis for T-ray signals containing multiple reflections.

It can be seen that many applications for T-rays, such as denoising or compression, gain advantages using wavelet representation. The compact representation of wavelets is a particular aspect that motivates us to use the wavelet transformation in reduction of the classification features of T-ray signals prior to the classification process.

## 6.4 Wavelet decomposition of T-ray signals

The reasonable number of features is important in the task of classification. A large number of classification features inevitably leads to the occurrence of *the curse of dimensionality* (Bellman 1961). It is relevant to the slow convergence to the optimum of a discriminant function in a high-dimensional space. More significantly, it causes the problem of a classifier overfitting to a specific training set, and thus prohibits good generalisation of a classifier. A way to avoid the overfitting problem is to use a large training dataset. But in some cases, such as in biomedical applications, the number of available observations in a dataset tends to be small, compared with the number of features. Alternatively, feature subset selection methods (Ferguson *et al.* 2004, Kohavi and John 1997) can also be used to avoid the problem at the expense of computational cost. Another possibility is to use a compact representation of the signals, such as a wavelet representation, in order to reduce the number of classification features.

A pulsed T-ray signal is very similar to a wavelet, because, as is the case for wavelets, a T-ray waveform is localised in the scale-space domain—namely, the majority of T-ray power is emitted in a short period of the order of picoseconds, whereas the power spectrum distributes around a resonant frequency. In addition, the properties of T-ray waveforms coincide with two characteristics of wavelets (Mittleman *et al.* 1996), which are the admissibility and the regularity. The *admissibility condition* implies a zero mean value of a function. The *regularity condition* assures that the first low-order moments vanish. The significance of the close resemblance is that a T-ray pulse can then be decomposed into a small number of wavelet coefficients. Thus the original signal power is spread over a few coefficients and is not overly *diluted*—this is desirable so that signal coefficients remain well above noise coefficients.

From the viewpoint in the time domain, a wavelet coefficient is a measure of correlation between a signal $f(t)$ and a daughter wavelet $\psi_{a,b}(t)$, which is a scaled, $a$, and shifted, $b$, version of a mother wavelet $\psi(t)$. A daughter wavelet is defined as

$$\psi_{a,b}(t) \;=\; \frac{1}{\sqrt{|a|}}\psi\left(\frac{t-b}{a}\right) \;;\quad a,b \in \mathbb{R},\; a \neq 0\,. \tag{6.1}$$

The wavelet transform for a discrete signal $f(k),\ k \in 0,\ldots,N-1$ with respect to a daughter wavelet $\psi_{a,b}(k)$ is given by

$$W_\psi(f)(a,b) \;=\; \sum_{k=0}^{N-1} f(k)\psi_{a,b}(k) = \langle f,\psi\rangle\ . \tag{6.2}$$

In this work, only discrete wavelet families are considered owing to their compact support. These wavelet families include Daubechies, Coiflets, Symlets, and some Biorthogonal wavelets with high smoothness.

The scaling, $a$, and shifting, $b$, of a wavelet can take on every possible value, resulting in a large number of coefficients. This situation poses the problem of redundant coefficients, defeating our intent of compact representation. Hence, a dyadic grid, i.e., $a = 2^{-j}$ and $b/a = l$, where $j,l \in \mathbb{Z}$ is preferred in construction of wavelet bases (Daubechies 1990). As a result, the coefficients generated according to the grid are unlikely to be redundant.

In our implementation, Mallat's multiresolution analysis (Mallat 1989) is used to decompose T-ray signals into multilevel approximations and details. As shown by a wavelet decomposition tree in Figure 6.1, an original signal $f$ is decomposed into several sets of approximation and detail coefficients, $cA$ and $cD$, respectively. At the first

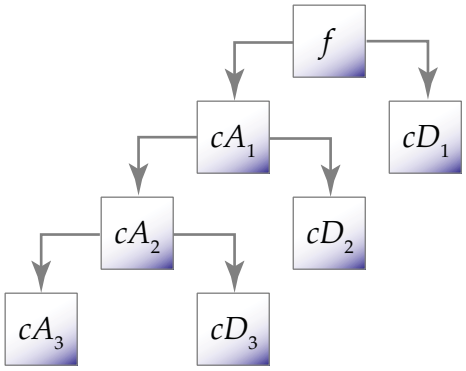


**Figure 6.1. Wavelet decomposition tree.** A signal, $f$, is decomposed by wavelet transform into several sets of approximation and detail coefficients, represented by $cA$ and $cD$, respectively. Those approximation coefficients hold the low-frequency information of the signal, whilst the detail coefficients hold the high-frequency information. The subscript denotes the level of decomposition.

step the signal is decomposed into $cD_1$ and $cA_1$. A sequence $cD_1$ is associated with the high frequency components of the signal. On the other hand, a sequence $cA_1$ is associated with the low frequency components. Subsequently, $cA_1$ becomes an input to the next decomposition level, giving $cA_2$ and $cD_2$. The decomposition process is recursive until it reaches the last possible level, which depends on each wavelet. The length of a sequence at a succeeding level is half of the length at a preceding level, i.e., if an original signal contains 200 points, $cD_1$ or $cA_1$ contains 100 points; $cD_2$ or $cA_2$ 50 points; and so on. The classification of T-ray signals in the experiment is performed with a sequence of detail or approximation coefficients at a particular level.

Since T-ray signals have a finite duration, a padding process (Liao *et al.* 2004) is necessary to correct border distortion. Periodic padding is appropriate for a T-ray signal, because the signal amplitude near the beginning and the end is close to zero, and hence the signal can be concatenated periodically without introducing any significant artefact. In addition, periodic padding can handle different sizes of decomposed sequences resulting from different mother wavelets. It is worth noting that zero padding is not recommended, as it may introduce irrelevant features to the classification problem.

## 6.5 Support vector machines and accuracy assessment

Essentially, the learning process for pattern classification attempts to determine the unknown parameters of a discriminant function, with the expectation that the optimised

function can correctly assign classes or labels to unseen patterns. In supervised learning, a two-class discriminant function is constructed using a given training set that includes input vectors (signals) $\mathbf{x}_i$ and their corresponding labels $y_i$;

$$(\mathbf{x}_i, y_i) \quad \in \quad \mathbb{R}^k \times \{-1, +1\} \qquad i = 1, \ldots, \ell, \tag{6.3}$$

assuming that the pairs are drawn independently, identically distributed (iid) from an unknown probability distribution $P(\mathbf{x}, y)$.

The concept of SVMs, laid out by Boser *et al.* (1992), is that the machine maps the input vectors onto a higher-dimensional space—the so-called feature space, $\mathbf{x} \mapsto \Phi(\mathbf{x}) \in \mathcal{H}$, and constructs an optimal hyperplane in that space. The mapping idea allows a linear discriminant function to perform on a nonlinear problem. Mathematically, the hyperplane in a high-dimensional space is given by

$$f(\mathbf{x}) \quad = \quad \mathbf{w} \cdot \Phi(\mathbf{x}) + b \,, \tag{6.4}$$

where $\mathbf{w} \in \mathcal{H}$ is the normal vector of the hyperplane, and $b$ is an offset between the hyperplane and the origin. A point that lies on the hyperplane satisfies the condition $\mathbf{w} \cdot \Phi(\mathbf{x}) + b = 0$. In the case of perfect separation, i.e., no training error, the following condition is held:

$$y_i \left(\mathbf{w} \cdot \Phi(\mathbf{x}_i) + b\right) \quad \geq \quad 1 \qquad \forall i \,. \tag{6.5}$$

Thus a margin, or a perpendicular distance from the hyperplane to any closest point, equals $1/\|\mathbf{w}\|$. The optimal hyperplane is constructed by maximising this distance, according to the structural risk minimisation (SRM) principle (Vapnik 1998). This can be formulated as a quadratic optimisation problem (Müller *et al.* 2001)

$$W^2 \quad = \quad \min_{\mathbf{w},b} \; \frac{1}{2}\|\mathbf{w}\|^2 \,, \tag{6.6}$$

subject to Equation 6.5. As $\mathbf{w}$ lies in the feature space, the minimisation problem cannot be solved for $\mathbf{w}$ and $b$ directly. By introducing Lagrange multipliers $\alpha_i$, $i = 1, \ldots, l$, corresponding to the input vector $\mathbf{x}_i$, we form the following Lagrangian with respect to the primary variables,

$$\begin{aligned} L_P \quad &= \quad W^2(\mathbf{w}, b, \boldsymbol{\alpha}) \\ &= \quad \max_{\boldsymbol{\alpha}} \min_{\mathbf{w},b} \; \frac{1}{2}\|\mathbf{w}\|^2 \; - \sum_{i=1}^{l} \alpha_i (y_i(\mathbf{w} \cdot \Phi(\mathbf{x}_i) + b) - 1) \qquad ; \alpha_i \geq 0 \quad \forall i \,. \end{aligned} \tag{6.7}$$

The saddle points of the Lagrangian with respect to $\mathbf{w}$ and $b$ are

$$\frac{\partial L_P}{\partial \mathbf{w}} = \mathbf{w} - \sum_{i=1}^{l} \alpha_i y_i \Phi(\mathbf{x}_i) = 0 \quad \Rightarrow \quad \mathbf{w} = \sum_{i=1}^{l} \alpha_i y_i \Phi(\mathbf{x}_i) \,, \tag{6.8a}$$

$$\frac{\partial L_P}{\partial b} = -\sum_{i=1}^{l} \alpha_i y_i = 0 \quad \Rightarrow \quad \sum_{i=1}^{l} \alpha_i y_i = 0 \,. \tag{6.8b}$$

By substituting Equations 6.8a and 6.8b back into Equation 6.7 and replacing $\Phi(\mathbf{x}_i) \cdot \Phi(\mathbf{x}_j)$ with the kernel function $\mathrm{K}(\mathbf{x}_i, \mathbf{x}_j)$, we have the Lagrangian with respect to the dual variable,

$$L_D = W^2(\boldsymbol{\alpha}) = \max_{\boldsymbol{\alpha}} \sum_{i=1}^{l} \alpha_i - \frac{1}{2} \sum_{i=1}^{l} \sum_{j=1}^{l} \alpha_i \alpha_j y_i y_j \mathrm{K}(\mathbf{x}_i, \mathbf{x}_j) \,, \tag{6.9}$$

subject to

$$\alpha_i \geq 0 \quad \forall i \qquad \text{and} \qquad \sum_{i=1}^{l} \alpha_i y_i = 0 \,. \tag{6.10}$$

Using ordinary quadratic programming (QP) methods to solve for a set of Lagrange multipliers, $\boldsymbol{\alpha}$, is not feasible for a large matrix. Particular methods designed for such problems are chunking (Boser *et al.* 1992) or Osuna's decomposition (Osuna *et al.* 1997). In this work the method of sequential minimal optimisation (SMO), proposed by Platt (1999), is employed to solve the Lagrangian in Equation 6.9.

Once a set of Lagrange multipliers is obtained, a non-linear discriminant function via the kernel can be constructed from the hyperplane, or Equation 6.4, with the weights $\mathbf{w}$ given by Equation 6.8a,

$$f(\mathbf{x}) = \mathrm{sgn}\left( \sum_{i=1}^{l} y_i \alpha_i \Phi(\mathbf{x}_i) \cdot \Phi(\mathbf{x}) + b \right) = \mathrm{sgn}\left( \sum_{i=1}^{l} y_i \alpha_i \mathrm{K}(\mathbf{x}_i, \mathbf{x}) + b \right) \,. \tag{6.11}$$

In the case of linear-kernel SVMs, which are used throughout this work, the discriminant function is simplified to

$$f(\mathbf{x}) = \mathrm{sgn}\left(\mathbf{w} \cdot \mathbf{x} + b\right); \qquad \mathbf{w} = \sum_{i=1}^{l} y_i \alpha_i \mathbf{x}_i \,. \tag{6.12}$$

Equation 6.12 represents a trained classifier, and can therefore assign a label, $f(\mathbf{x})$, to a given input data, $\mathbf{x}$. For further discussion on SVMs, please refer to, e.g., Burges (1998) or Müller *et al.* (2001).

### Leave-one-out cross validation

To assess the accuracy of a trained classifier, many methods are available, such as the hold-out estimate or $\nu$-fold cross validation. However, for a small dataset such as that provided in this work, these methods are prone to extreme bias. Leave-one-out cross validation is more suitable, because it gives a nearly unbiased estimate of the expected generalisation error (Kohavi 1995).

The procedure for leave-one-out cross validation is as follows. Given that there are $\ell$ vectors, the training process repeats $\ell$ times. For the first time, one particular vector is held out, leaving the remaining $\ell - 1$ vectors as a training set. Once the first training process is completed, the classifier is tested with the holdout vector. By repeating this procedure $\ell$ times with a different vector held out each time, all vectors are tested and the classifier accuracy is achievable based on the $\ell - 1$ training vectors.

## 6.6 Sample data acquisition

The measurement is performed using a standard THz-TDS system arranged in a transmission mode (Ferguson and Zhang 2002). The T-ray emitter is a 2-mm-thick $\langle 110 \rangle$-oriented ZnTe crystal, and the T-ray beam is detected using electro-optic sampling in a 4-mm-thick (110) ZnTe crystal. The laser illuminating the emitter and detector is a regeneratively amplified mode-locked Ti:sapphire laser producing 130 fs pulses with a 1 kHz repetition rate and an average power of 0.7 W. A lock-in amplifier time constant of 10 ms is used.

Two types of biological cells, one is normal human bone (NHB) and the other is human osteosarcoma (HOS), are used in the experiment. Both are grown in identical polyethylene flasks, transparent to T-ray radiation and thus enable spectroscopic measurement of the live cells in a transmission geometry. A set of T-ray signals is obtained providing spectroscopic information at 48 different locations for each flask. A signal at each location contains 200 data points, with a total duration of 13.33 ps, sampled every 0.067 ps. The FWHM of the main pulse is approximately 0.5 ps, corresponding to the signal bandwidth of 2 THz. Figure 6.2 shows average T-ray signals for the NHB and HOS cells. The similarity between the two responses is obvious from the plot of the difference signal.

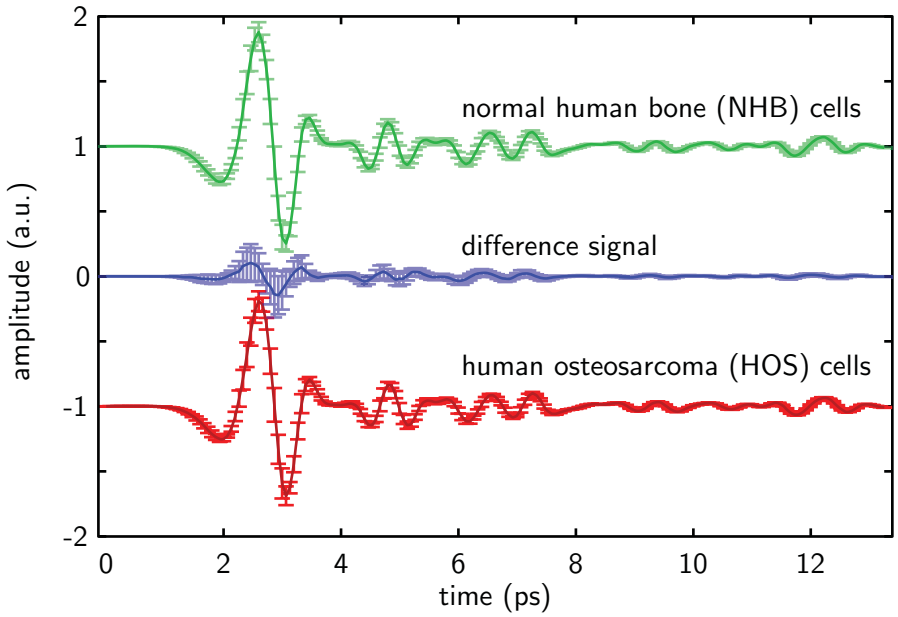


**Figure 6.2. Average T-ray signals for HOS and NHB cells.** In each case, the average signal and its standard deviation are estimated from 48 measurements. The difference signal is calculated from $\langle E_{\mathrm{NHB}}(t)\rangle - \langle E_{\mathrm{HOS}}(t)\rangle$, and the associated standard deviation is calculated from $[s^2_{\mathrm{NHB}}(t) + s^2_{\mathrm{HOS}}(t)]^{1/2}$, where $s^2_{\mathrm{NHB}}(t)$ and $s^2_{\mathrm{HOS}}(t)$ represent the variances for the NHB and HOS signals, respectively. The signals are vertically offset for clarity.

## 6.7 Classification results

A set of 96 signals is available from the THz-TDS measurements. Half of the signals belong to the HOS cells, and the rest belong to the NHB cells. Prior to the signal decomposition and classification, the HOS signals are labelled the *positive class*, and the NHB signals are labelled the *negative class*. These signals are decomposed using a particular wavelet to a particular level. The decomposed sequences are then classified by a linear-kernel SVM based on the leave-one-out cross validation to find a wavelet and level that result in the highest classification accuracy.

Table 6.1 shows the classification accuracy when the input features are the sequence of wavelet coefficients obtained from Daubechies, Coiflets, or Biorthogonal wavelet decomposition with a different order, sequence (approximation, *cA*, or detail, *cD*), and level. The lengths of the coefficients at levels 1, 2, and 3 are 100, 50, and 25, respectively. Each value in the table indicates the number of misclassified vectors from the total of 96 vectors based on the leave-one-out cross validation methodology. When used for decomposition, Symlets lead to identical classification results to Daubechies, whilst

**Table 6.1. Leave-one-out classification error from total 96 vectors.** The values in the table indicate the number of misclassified samples, whilst the values in braces indicate the vector length. The classification results for Symlets decomposition are identical to those for Daubechies decomposition, and thus are not shown here.

| Wavelet | Order | Misclassified sample | | | | | |
|---|---|---|---|---|---|---|---|
| | | $cD_1\{100\}$ | $cA_1\{100\}$ | $cD_2\{50\}$ | $cA_2\{50\}$ | $cD_3\{25\}$ | $cA_3\{25\}$ |
| Daubechies | 1 | 21 | 9 | 19 | 15 | 18 | 17 |
| | 2 | 29 | 8 | 12 | 12 | 9 | 18 |
| | 3 | 27 | 13 | 16 | 13 | 8 | 15 |
| | 4 | 30 | 16 | 24 | 11 | 12 | 22 |
| | 5 | 40 | 19 | 13 | 13 | 6 | 19 |
| | 6 | 34 | 15 | 18 | 14 | 14 | 24 |
| | 7 | 38 | 13 | 25 | 8 | 15 | 20 |
| | 8 | 44 | 12 | 17 | 13 | 13 | 20 |
| | 9 | 44 | 12 | 29 | 14 | 14 | 24 |
| | 10 | 41 | 12 | 32 | 6 | 17 | 21 |
| Coiflets | 1 | 21 | 15 | 24 | 10 | 16 | 18 |
| | 2 | 31 | 19 | 25 | 11 | 15 | 21 |
| | 3 | 32 | 14 | 23 | 11 | 13 | 16 |
| | 4 | 33 | 14 | 24 | 10 | 10 | 24 |
| | 5 | 36 | 18 | 27 | 10 | 9 | 16 |
| Biorthogonal | 1.3 | 21 | 9 | 13 | 14 | 15 | 20 |
| | 1.5 | 20 | 9 | 19 | 10 | 9 | 21 |
| | 2.4 | 26 | 17 | 16 | 17 | 13 | 13 |
| | 2.6 | 26 | 15 | 22 | 11 | 17 | 20 |
| | 2.8 | 26 | 18 | 11 | 16 | 19 | 21 |
| | 3.9 | 32 | 13 | 15 | 11 | 14 | 14 |

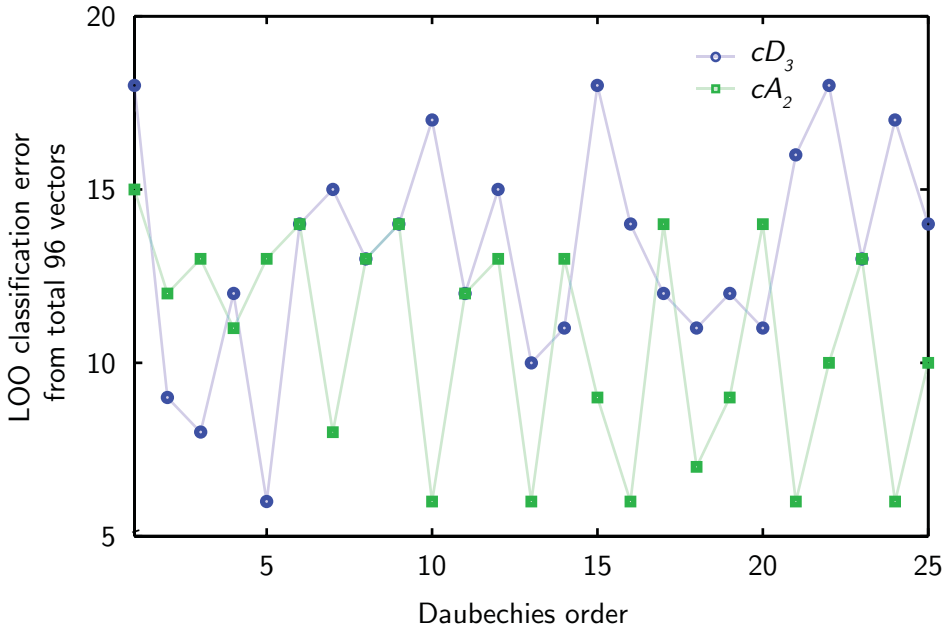


**Figure 6.3. Leave-one-out (LOO) classification error for Daubechies decomposition.** The classification error is based on a total of 96 training/testing vectors obtainable from Daubechies decomposition with different Daubechies orders. The sets of detail coefficients at decomposition level 3 ($cD_3$) or approximation coefficients at level 2 ($cA_2$) are used as the classification features. The lines connecting the points are merely for better perception.

Coiflets and Biorthogonal wavelets result in inferior accuracy to Daubechies. Therefore, the Daubechies decomposition is emphasised. Up to three levels of decomposition are utilised, because the trial reveals that further decomposition levels produce poorer classification accuracies. Also note that from the trial there is no improvement beyond Daubechies 10. However, the classification error for $cA_2$ and $cD_3$ sequences decomposed using higher Daubechies orders is given in Figure 6.3.

In Table 6.1, the classification results are listed with no apparent trend, either regarding the decomposition level or wavelet order. Hence, to find the decomposition setting that yields the highest classification accuracy, the trial-and-error strategy is seemingly required. However, still some common trends for all wavelet families and orders are observable. At the first decomposition level, the results for $cA_1$ are consistently superior to those for $cD_1$, implying the relevant information underlying $cA_1$. When $cA_1$ is decomposed into the next level, it is possible that this information is split into both $cD_2$ and $cA_2$. This situation occurs in some cases such as Daubechies 1 or 2, since the

classification accuracies for both $cD_2$ and $cA_2$ become worse. On the other hand, an improvement of the accuracy for $cA_2$ in many other cases can be observed, for instance, in all orders of Coiflets. Further, when $cA_2$ is decomposed into $cD_3$ and $cA_3$, it can be assumed from the results that the useful information resides in $cD_3$. In addition, it is arguable that the improvement of the classification accuracy at a finer decomposition level contributes to the reduction of features by discarding irrelevant information.

The best classification result, 6 misclassified vectors or 93.8% accuracy, is obtainable by using the features from the Daubechies decomposition. This rate of accuracy is better than the best obtainable from Coiflet and Biorthogonal features, which is 90.63% (9 misclassified vectors). Specifically, the best accuracy of all (93.8%) is available from $cD_3$ decomposed by Daubechies 5 and $cA_2$ decomposed by Daubechies 10. Choosing between these two cases is ambiguous without an additional criterion. Nevertheless, it can be concluded from the classification viewpoint that $cD_3$ is superior—a sequence $cD_3$ with 25 coefficients is less susceptible to *the curse of dimensionality* than a sequence $cA_2$ with 50 coefficients.

## 6.8 Further analysis

Up to this point the optimal features, which are the $cD_3$ coefficients decomposed from the original signals using Daubechies 5, is determined. Hence, it implies that the information provided by $cD_3$ is highly relevant to the distinction between the two classes in the given dataset. In this section, further investigation into $cD_3$ is given. Note that in this section the notation $cD_3$ alone means a sequence of the detail coefficients at level 3, which is decomposed using Daubechies 5, unless stated otherwise.

### 6.8.1 Optimal features

The average $cD_3$ coefficients and their standard deviations for each class of the signals are plotted in Figure 6.4. Although the $cD_3$ sequence contains the most suitable features for our classification problem, not all of its coefficients are relevant. Among various feature selection methods (Kohavi and John 1997), the Fisher[11] criterion score

[11]Historical note: R. A. Fisher lived and worked in Adelaide during the latter part of his career. He delivered a series of 20 lectures at The University of Adelaide between 1959 and 1960. He died in Adelaide in 1963.

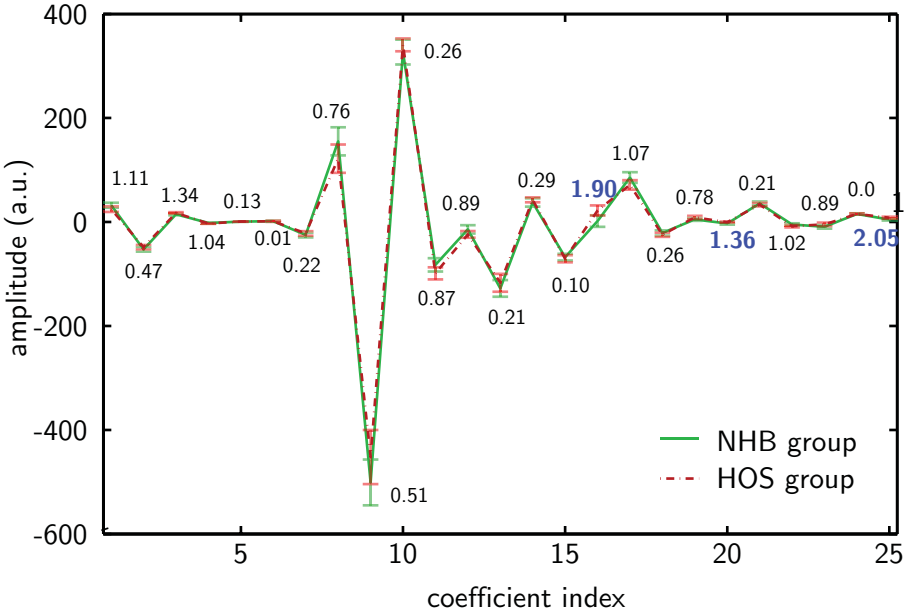


**Figure 6.4. Coefficients, $cD_3$, of T-ray signals for HOS and NHB cells.** The coefficients are obtainable from wavelet decomposition of the measured signals using the Daubechies 5 mother wavelet. Each plot represents the average coefficients, accompanied by the $1\sigma$ standard deviation. The associated relevance scores are calculated by using the Fisher criterion, given in Equation 6.13. The coefficients with bold scores are regarded as the three most relevant features. The lines connecting the coefficients are merely for display and are not physical.

(Pavlidis *et al.* 2001) provides a simple tool for quantitative evaluation of a feature. Given that $\mu_k^+$ and $\sigma_k^+$ are the mean and the standard deviation of feature $k$ for the *positive class*, and $\mu_k^-$ and $\sigma_k^-$ are the mean and the standard deviation of feature $k$ for the *negative class*, the Fisher score is calculated from

$$c_i = \frac{(\mu_i^+ - \mu_i^-)^2}{(\sigma_i^+)^2 + (\sigma_i^-)^2} \,. \tag{6.13}$$

The calculated scores are assigned to the coefficients in Figure 6.4. The higher the score, the more relevant the feature.

To provide a visual impression of the relevant features, two features with the highest Fisher scores are selected to plotted against each other in a two-dimensional space. The selected features are $cD_3(16)$ and $cD_3(25)$, where the numbers in the parentheses indicate the coefficient indices. The two features give the Fisher scores of 1.90 and 2.05 respectively. The scattering of the 96 signals, each represented by the two features, is shown in Figure 6.5. It can be seen that the signals in each class are well distributed

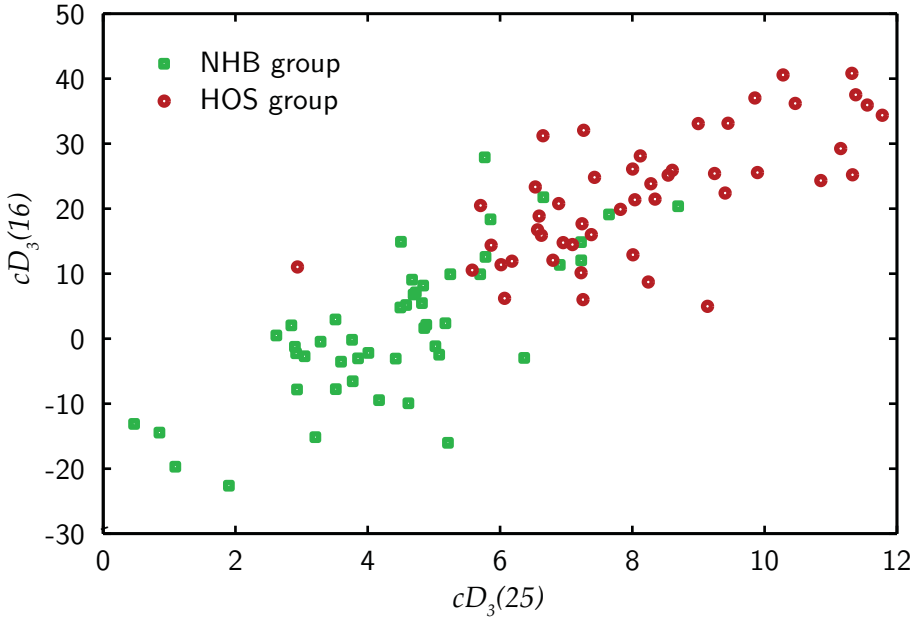


**Figure 6.5. Scattering of the signals in the feature space.** The feature space is defined by the two optimal features, $cD_3(16)$ and $cD_3(25)$, which provide the highest Fisher criterion scores of 1.9 and 2.05, respectively. Each dot in this space represents each measured T-ray signal for either NHB or HOS cells.

in this feature space, and are nearly separable from the signals in the other class. The separation is more obvious in a higher dimension, but that is difficult to perceive on a two dimensional projection.

### 6.8.2 Information underlying the optimal features

To give insight into the wavelet coefficients relevant to the classification problem, the $cD_3$ sequence is transformed backward into the time domain and forward into the frequency domain, as shown in Figures 6.6 and 6.7, respectively.

The time-domain signals in Figure 6.6, reconstructed from $cD_3$, preserve the structure of the original T-ray signals shown in Figure 6.2. Therefore, it can be inferred that the sequence of wavelet coefficients is an appropriate compact representation of the T-ray signal. In particular, an original time-domain signal contains 200 data points, whereas a corresponding sequence of wavelet coefficients contains only 25 data points. Hence, the compression ratio is as high as 1:8.

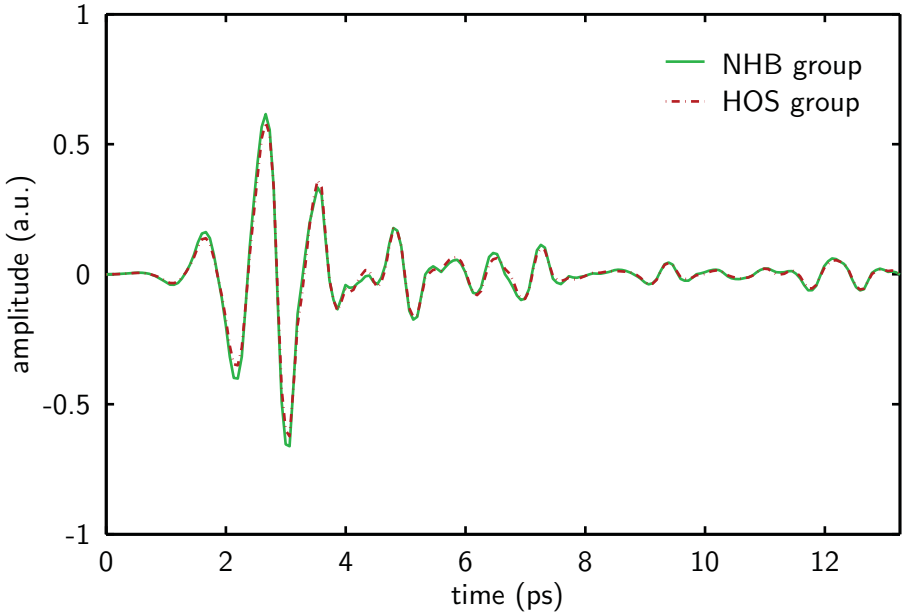


**Figure 6.6. Signals for HOS and NHB cells reconstructed from $cD_3$ coefficients.** The $cD_3$ coefficients are obtainable from wavelet decomposition of the measured T-ray signals for HOS and NHB cells. In the reconstruction process, the wavelet coefficients at other decomposition levels are all suppressed to zero.

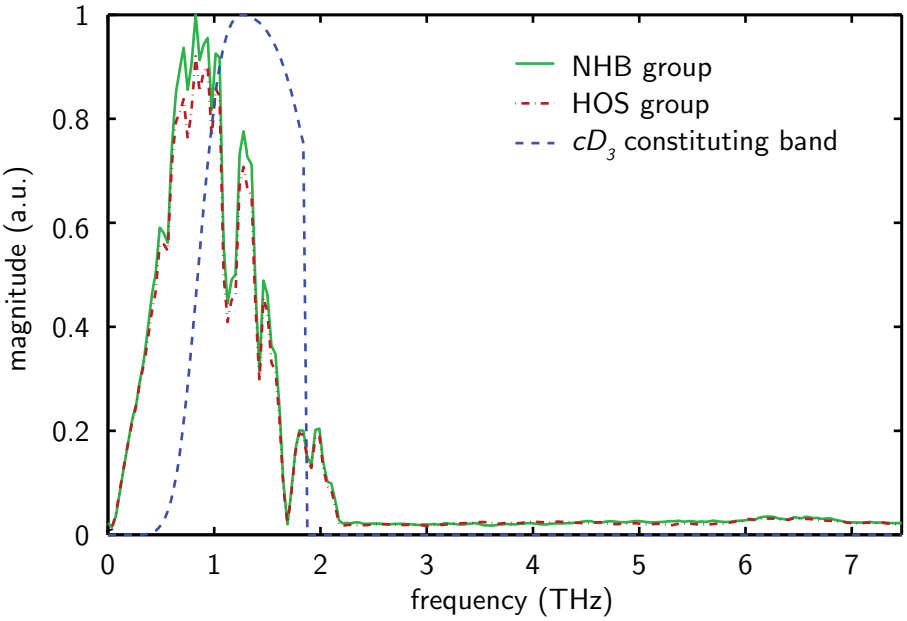


**Figure 6.7. Average spectra for HOS and NHB cells and frequency band for $cD_3$.** The frequency band of this particular wavelet decomposition level covers a major part of the measured T-ray spectra, whilst missing out a band below 0.5 THz. Hence this implies that the $cD_3$ coefficients can effectively retain most of the signal information.

Figure 6.7 shows the frequency band for $cD_3$ in comparison to the measured T-ray spectra. The calculation shows that the frequency band for $cD_3$ can retain 43% of the T-ray energy. If the classification features are Fourier coefficients at the same frequency range, i.e., from 0.5 to 2 THz, the number of features rises to 80—this number is estimated from the magnitude and phase at the intrinsic frequency resolution of 37.5 GHz. Thus, to represent the same information, it requires a larger number of features in the frequency domain than in the wavelet domain.

## 6.9 Conclusion and potential extensions

Many materials have unique spectral features in the T-ray frequency range. Thus, the sample spectra obtained from THz-TDS can be useful in the task of material classification. However, in a number of cases, specifically in the case of many biological samples, no distinctive spectral features are observable, and the absence of distinctive features prohibits simple classification. This work introduces machine learning to cope with the classification problem. Supervised classifiers are used to classify two similar groups of T-ray signals measuring two types of biological samples.

The wavelet coefficients of the T-ray signals are selected as features to be classified by SVMs. A number of mother wavelets and decomposition levels are considered in search for the best representation of the T-ray signals. For a particular mother wavelet and decomposition level, a classification accuracy of as high as 93.8%, based on only 25 features, is achievable. The subsequent analysis shows the effective representation of the optimal wavelet coefficients in the time and frequency domains.

The success rate in the classification of T-ray signals without distinctive features motivates the implementation of machine learning for a number of T-ray applications. An example application includes sensing a minute amount of a target material (Mickan *et al.* 2002c, Menikh *et al.* 2004), which requires relatively sophisticated equipment to amplify a small difference in signals. The introduction of machine classification may alleviate this requirement.

For a higher classification accuracy, an implementation of wavelet packet algorithms (Wickerhauser 1991) to decompose of T-ray signals is an attractive extension. The wavelet packet transform offers the flexibility to signal decomposition owing to its

ability to analyse both approximation and detail results to the maximum level. However, a more efficient technique than trial-and-error is required to assess the classification accuracy, because many different sequences of coefficients are available from the wavelet packet decomposition.

Having discussed the signal processing aspect of THz-TDS in Chapters 5 and 6, we now turn to Part II of the thesis—system evaluation and optimisation—with Chapter 7 focusing on measurement uncertainty in THz-TDS.

Chapter 7

# Uncertainty in THz-TDS Measurements

MEASUREMENTS of optical constants at T-ray frequencies have been performed extensively using THz-TDS. Spectrometers, together with physical models explaining the interaction between a sample and T-ray radiation, are progressively being developed. Nevertheless, measurement errors in the optical constants, so far, have not been systematically analysed. This situation calls for a comprehensive analysis of measurement uncertainty in THz-TDS systems. The sources of error existing in a terahertz time-domain spectrometer and throughout the parameter estimation process are identified. The analysis herein quantifies the impact of each source on the output optical constants. As a consequence, the evaluation of uncertainty opens up the possibility of methodically enhancing measurement precision.

## 7.1 Introduction

Components and techniques have been developed such that a THz-TDS spectrometer can considerably overcome intrinsic problems from thermal background radiation and atmospheric absorption. A THz-TDS waveform transmitted through a material sample is typically rich in information, since its shape is altered by the material's characteristic frequency response. Sample and reference waveforms, once converted by Fourier transform into the frequency domain, can be processed to extract the frequency-dependent optical constants of a material by means of a reliable parameter extraction method (see Chapter 4 for more details).

Nevertheless, even if one assumes that the parameter extraction process is nearly perfect, the operation of the hardware is far from ideal. Namely, measurements of signals and associated parameters still contain errors, which affect the quality of the extracted optical constants. Several sources of random and systematic errors exist throughout the measurement process. These sources are, for instance, signal noise, sample misalignment, thickness measurement variation, etc. Thus, for a reliable measurement, the evaluation of uncertainty is critical in the optimisation of measurement accuracy. The proposed uncertainty model is a combination of the analytical models for significant error sources, and is applicable to transmission-mode THz-TDS.

Some merits of the uncertainty model proposed in this work are as follows: (i) the model reduces the time spent in determining the measurement uncertainty, which previously was carried out using lengthy Monte Carlo simulations; (ii) the model allows the evaluation and comparison of more than one source of error, rather than the noise in the signal alone; (iii) the model offers a standard in the evaluation of uncertainty in the optical constants obtained from THz-TDS, and thus permits assessment of and comparison among results from different measurements; (iv) an overall uncertainty determined from the model can be used in the discrimination of an intrinsic absorption peak from artefacts, as any peak that has a magnitude, relative to the baseline, lower than the uncertainty level, can be labelled as an artefact; and (v) through the model, a methodical optimisation of the measurement parameters is possible.

The work is organised as follows: Section 7.3 gives the background on THz-TDS measurement and parameter extraction, and identifies an open question regarding the analysis of error in the process. The question leads to an introduction to the evaluation of uncertainty in Section 7.4, which can be skipped for those who are familiar with the

subject. In Section 7.5 the sources of error in the THz-TDS measurement and parameter extraction process are identified and characterised by analytical models, based on the evaluation of uncertainty. The proposed models are validated with Monte Carlo simulations in Section 7.6, and some implications in the models are discussed. A practical implementation of the developed uncertainty model is given in Section 7.7.

## 7.2 Research objective and framework

### Objective

- To thoroughly identify sources of either random or systematic error, in a THz-TDS measurement, which affect the characterised optical constants. The errors involve both the spectrometer and the parameter extraction process. The errors are considered under normal system operation. The consideration of error sources is not specific to the type of terahertz generation/detection, i.e., photoconductive antennas or nonlinear crystals.

- To provide a model for the evaluation of uncertainty in the optical constants, measured by a transmission THz-TDS measurement. The model is composed of many components, each explaining the relation between the variance/deviation produced by an identified source of error and the variance/deviation in the optical constants. The proposed analytical models are verified with the results from Monte Carlo simulation (MCS) or other numerical means. A case study on real data is also given.

### Framework

The assumptions of a THz-TDS measurement considered here are that (i) a sample under measurement is a homogeneous dielectric slab with parallel and flat surfaces, where the scattering of T-rays is negligible; (ii) the incident angle of the T-ray beam is normal to the sample surface; (iii) the transverse dimension of the sample is larger than the incident beam waist, so there is no edge diffraction; (iv) the reference signal is measured under the same conditions as the sample signal, except for the absence of the sample; (v) a random error is assumed to follow a normal probability distribution, unless stated otherwise; (vi) the resolution of the measuring apparatus is sufficiently high

so that quantisation error is negligible, unless stated otherwise; (vii) the measuring instruments are well calibrated; and (viii) there is no human error in the measurements.

The evaluation of uncertainty is on the basis of the *Guide to the Expression of Uncertainty in Measurement—GUM*, recommended by the International Organization for Standardization (ISO) and its partners[12] (ISO 1993). Some aspects of the guideline are tailored, where appropriate. The technical terms, where applicable, follow the definitions provided in *International Vocabulary of Basic and General Terms in Metrology—VIM*, published by the ISO in the name of its partners (ISO 2004).

## 7.3 THz-TDS for measurement of optical constants

The process of utilising THz-TDS in determining the optical constants of a sample is composed of many steps, as illustrated in Figure 7.1. At the heart of the process is the measuring device, a terahertz time-domain spectrometer, which has been progressively developed to achieve a higher SNR and wider bandwidth. The quantity provided by a THz-TDS measurement is a time-domain signal. Thus, a physical model that can relate the measured signal to the optical properties of a measured sample is required. This model is then used to estimate or extract the optical constants of a sample from a recorded signal. The measurement is not ideal, and therefore incorporates errors, which demand characterisation to quantify the overall measurement uncertainty. Further details for each part of the measuring process are described below.

### 7.3.1 Measuring device—THz-TDS

A THz-TDS system comprises an ultrafast optical laser, a T-ray emitter/receiver, an optical delay line, a set of guiding and collimating optics, and a material sample under test. The ultrafast optical pulse is divided into two paths, a probe beam and a pump beam, by a beam splitter. At the emitter, the optical pump beam stimulates

[12]The organisations that participate in GUM and VIM: the International Bureau of Weight and Measures (BIPM), the International Electrotechnical Commission (IEC), the International Federation of Clinical Chemistry (IFCC), the International Organization for Standardization (ISO), the International Union of Pure and Applied Chemistry (IUPAC), the International Union of Pure and Applied Physics (IUPAP), and the International Organization of Legal Metrology (OIML).

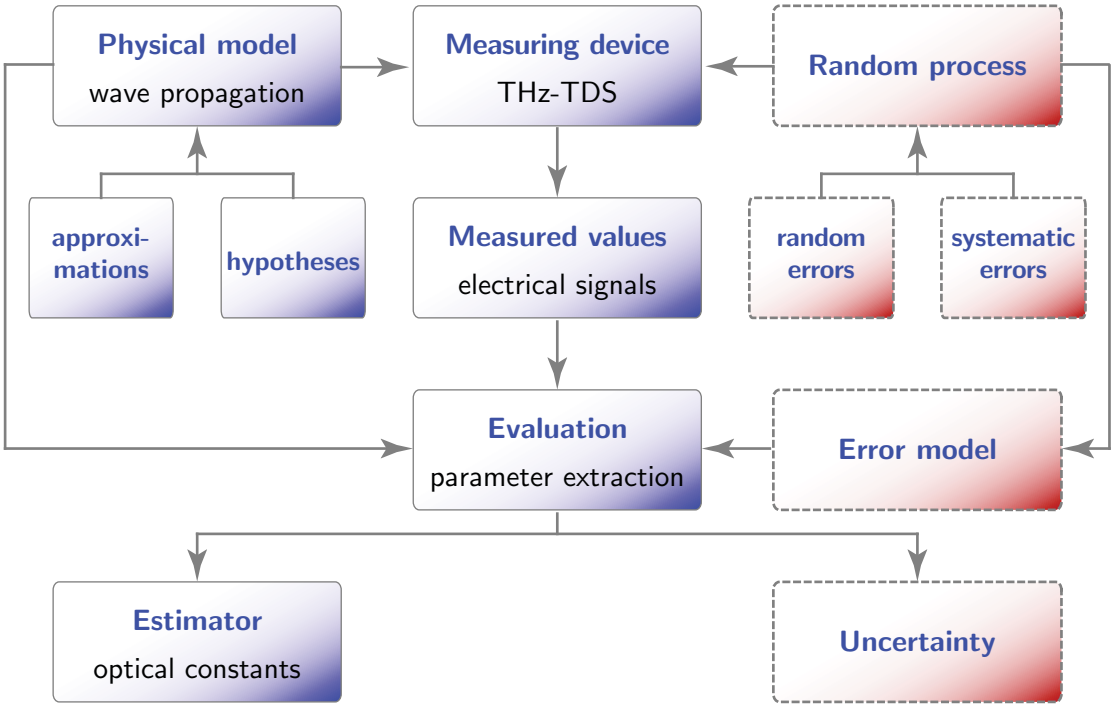


**Figure 7.1. Parameter estimation process using THz-TDS measuring system.** The process is mainly composed of a T-ray spectrometer, a physical T-ray propagation model, and a random process. The blue solid boxes represent well reported parts of the THz-TDS measurement process, whereas the red dashed boxes have not been fully analysed and are now addressed in this chapter. Modified from Grabe (2005).

T-ray pulsed radiation usually via either charge transport (Smith *et al.* 1988) or an optical rectification effect (Xu *et al.* 1992), depending on the emitter type. A typical T-ray system based on photoconductive antennas for emission and detection is shown in Figure 7.2. The diverging T-ray beam is collimated and focused onto the sample by the guiding and collimating optics. After passing through the sample, the T-ray beam is recollimated and focused onto the receiver by an identical set of guiding and collimating optics. At the receiver, the probe beam optically gates the T-ray receiver for a short time duration compared to the arriving T-ray pulse duration. As in the case of T-ray generation, the detection or gating can be performed via either charge transport or electro-optic sampling (Wu and Zhang 1995). Synchronisation between the optical gating pulse and the T-ray pulse allows the coherent detection of the T-ray signal at each time instant. A complete temporal scan of the T-ray signal is enabled by the discrete micromotion of a mechanical stage controlling the optical delay line. The system delivers a time-resolved T-ray pulse, which is readily convertible to a wideband T-ray spectrum via Fourier transform.

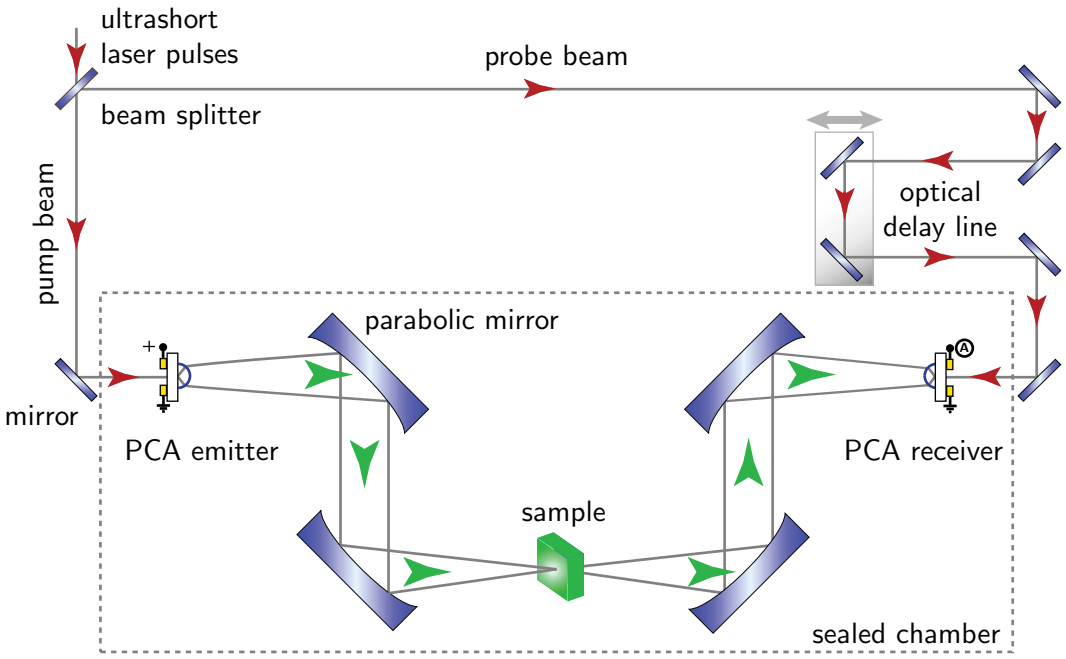


**Figure 7.2. THz-TDS system configured in transmission mode.** The system consists of an ultrafast optical laser, a T-ray emitter/receiver, an optical delay line, a set of mirrors, and a material sample. The emitter and receiver shown are photoconductive antennas. The optical beam path is indicated by small red arrowheads, and the T-ray beam path by large green arrowheads.

### 7.3.2 Physical model and parameter extraction

A key aim of a THz-TDS measurement is to determine the frequency-dependent optical constants of a sample under test. However, a signal available from a THz-TDS system is in the time domain, and suffers various effects determined by geometric optics, i.e., reflection and refraction, influenced by the sample. This necessitates a physical model to describe these effects and a measurement function to extract the constants from the signal.

Typically, a T-ray signal that passes through a parallel-surfaced dielectric sample, at a normal angle of incidence, can be expressed as a function of the frequency, assuming no reflection, by

$$E_{\mathrm{sam}}(\omega) \;=\; \eta \frac{4\hat{n}(\omega)n_0}{[\hat{n}(\omega)+n_0]^2} \cdot \exp\left\{-j\hat{n}(\omega)\frac{\omega l_\theta}{c}\right\} \cdot E(\omega)\,, \tag{7.1}$$

where $E(\omega)$ is the complex emitted wave; $\eta$ is the transmission factor of free air surrounding the sample; $n_0$ is the refractive index of free air; $\hat{n}$ is the complex refractive index of the sample; and $l_\theta$ is the propagation length inside the sample, which equals

the sample thickness $l$ for the normal angle of incidence. The complex refractive index, $\hat{n}(\omega) = n(\omega) - j\kappa(\omega)$, comprises the index of refraction, $n(\omega)$, and the extinction coefficient, $\kappa(\omega)$, which, together, are called the optical constants. In the above equation, $4\hat{n}(\omega)n_0/[\hat{n}(\omega)+n_0]^2$ is a consequence of the transmission at the sample-air interfaces, and the exponential term represents the complex response of bulk material. In addition to the sample response,

$$E_{\text{ref}}(\omega) \;=\; \eta \cdot \exp\left\{-jn_0\frac{\omega l}{c}\right\} \cdot E(\omega)\,, \tag{7.2}$$

is the complex frequency response of a reference signal, i.e., a signal measured with the same settings but with the absence of the sample.

The material parameter extraction process requires both $E_{\text{sam}}(\omega)$ and $E_{\text{ref}}(\omega)$, which are determined from time-domain measurements. The sample response normalised by the reference, or $E_{\text{sam}}(\omega)/E_{\text{ref}}(\omega)$, yields the complex transfer function of a material in the frequency domain:

$$H_0(\omega) \;=\; \frac{4\hat{n}(\omega)n_0}{[\hat{n}(\omega)+n_0]^2} \cdot \exp\left\{-\kappa(\omega)\frac{\omega l}{c}\right\} \cdot \exp\left\{-j[n(\omega)-n_0]\frac{\omega l}{c}\right\}\,. \tag{7.3}$$

Often, the complex refractive index, $\hat{n}(\omega)$, which is a component of the transmission at air-sample interfaces, is approximated to a real index, $n(\omega)$, giving

$$H(\omega) \;=\; \frac{4n(\omega)n_0}{[n(\omega)+n_0]^2} \cdot \exp\left\{-\kappa(\omega)\frac{\omega l}{c}\right\} \cdot \exp\left\{-j[n(\omega)-n_0]\frac{\omega l}{c}\right\}\,. \tag{7.4}$$

This simplified transfer function facilitates the parameter extraction process, but also introduces an error due to the approximation. Later, this type of error will be taken into account, and a proper treatment will be provided in Section 7.5.4. Taking the argument and logarithm of the simplified transfer function gives, respectively,

$$\angle H(\omega) \;=\; -[n(\omega)-n_0]\frac{\omega l}{c}\,, \tag{7.5a}$$

$$\ln|H(\omega)| \;=\; \ln\left[\frac{4n(\omega)n_0}{(n(\omega)+n_0)^2}\right] - \kappa(\omega)\frac{\omega l}{c}\,. \tag{7.5b}$$

The optical constants can be deduced from Equations 7.5a and 7.5b as

$$n(\omega) \;=\; n_0 - \frac{c}{\omega l}\angle H(\omega)\,, \tag{7.6a}$$

$$\kappa(\omega) \;=\; \frac{c}{\omega l}\left\{\ln\left[\frac{4n(\omega)n_0}{(n(\omega)+n_0)^2}\right] - \ln|H(\omega)|\right\}\,. \tag{7.6b}$$

The extracted optical constants are an ultimate outcome of a THz-TDS measurement process, and from now on Equations 7.6a and 7.6b will be referred to as the measurement functions. Quantities obtained from these measurement functions, to some extent, contain a measurement error from the input quantities, and this error motivates the development of a proper procedure for the evaluation of the uncertainty in the results.

### 7.3.3 Evaluation of uncertainty in THz-TDS measurement

Many sources of randomness affecting a THz-TDS signal have been reported so far. These sources include laser intensity fluctuation (Son *et al.* 1992, Haus and Mecozzi 1993, Poppe *et al.* 1998), optical and electronic noise (van Exter and Grischkowsky 1990c, Duvillaret *et al.* 2000), delay line stage jitter (Letosa *et al.* 1996), registration error (Cohen *et al.* 2006), and so on. Mathematical treatment for these noise sources is available in general. Contributions to the error in the estimated optical constants are not only from the randomness in the signal, but also from imperfections in the physical setup and parameter extraction process. These imperfections relate to, for example, the sample thickness measurement, the sample alignment, and so on.

An example situation, where the evaluation of the uncertainty is critical, is considered by Fischer *et al.* (2005a). The dynamic range of the experiment can be increased by averaging a series of measured signals in the time domain. Averaging their corresponding spectra does not affect the dynamic range (Fischer *et al.* 2005a). By averaging signals in the time domain, the standard deviation, therefore, appears in the time domain with the corresponding mean value. Accordingly, it requires an uncertainty model, which can transform the standard deviation of a time-domain signal into the standard deviation of the optical constants.

A few limited models for tracking the uncertainty in a THz-TDS measurement can be found in the literature, but they are specific cases with loss of generality and thus are only indirectly relevant to our discussion. For noise analysis, the model by Duvillaret *et al.* (2000) is used in the calculation of the uncertainty in the optical constants impacted solely by noise in the reference and sample spectra. In double-modulated differential time-domain spectroscopy (DTDS), the evaluation of uncertainty is employed for numerical determination of the optimum thickness difference of a liquid sample (Mickan *et al.* 2004). The evaluation focuses on a dual-thickness geometry, where the

Fresnel transmission coefficient is absent from the transfer function. Confidence intervals are established for the real and imaginary parts of the transfer function, which is influenced by noisy spectra (Pupeza *et al.* 2007). These confidence intervals assist the process of smoothing the estimated optical constants.

It would appear that the previous literature addresses development of the uncertainty models for the optical constants in a superficial manner. In those cases, the work only considers the influence of signal noise, and/or does not extend the model into the time domain. Furthermore, the developed linear models are rarely verified by a nonlinear numerical simulation. Based upon motivation from the requirements discussed earlier, an evaluation of uncertainty for a THz-TDS measurement is established in this work, with the aim of a comprehensive list of error sources in the system.

## 7.4 Methodology for evaluation of uncertainty

This section introduces a basic evaluation of uncertainty, presented in four subsections, as follows: Section 7.4.1 discusses some definitions usually found in the uncertainty analysis. Evaluation of random and systematic errors with different paradigms is given in Section 7.4.2. A means to determine and combine measurement uncertainties in the case that an output quantity is a function of one or more input quantities is shown in Section 7.4.3. The resolution limit in measurement, which can give rise to a systematic error, is treated separately in Section 7.4.4.

### 7.4.1 General definitions

A general aim of the evaluation of uncertainty is to establish a quantity that exhaustively quantifies ambiguity present in a measurement (Lira and Wöger 1997). An implication of the uncertainty is that it can reasonably localise the true value of a measurand with respect to the mean value, although this statement is ambiguous as the true value is by nature inaccessible. Nevertheless, no matter which viewpoint is held, an appropriate measurement result is always accompanied by an uncertainty, which is useful in the justification of the experiment and in comparison among measurements.

Evaluation of measurement uncertainty can be categorised into two types, depending on the source of information. According to VIM (ISO 2004), Type A evaluation

of uncertainty involves a direct statistical analysis of measurements under repeatability conditions, whereas Type B involves obtaining a measurement uncertainty via other means, such as a published value or a deduction from personal experience. In this work, evaluation of measurement uncertainty in THz-TDS concerns both types of evaluations.

Before further information about methodology for an evaluation of uncertainty is discussed, some important technical terms frequently used in the uncertainty community are introduced. Consider Figure 7.3, where the variable $X$ is subject to measurement. The true value or measurand $x_0$ is sought by the observer. In fact this value cannot be accessed due to the lack of information about the systematic error, which constantly biases the measurement result in one direction. What is obtainable with a single measurement is an estimation $x_l$, which deviates from the true value by both the systematic and random errors. The average value of $N$ statistically independent measurements

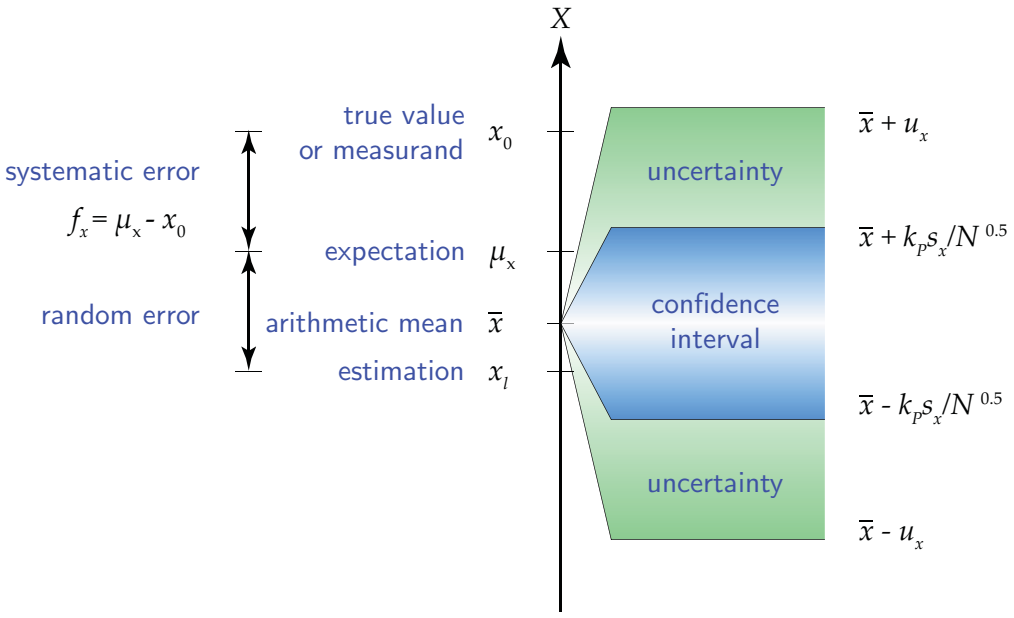


**Figure 7.3. Some definitions and relations used in evaluation of uncertainty.** The systematic error biases the expectation from the true value, whereas the random error added to the expectation yields the estimation. The confident interval localises the expectation with regard to the arithmetic mean, and the uncertainty expands the interval to localise the true value. This graph is related to Type A evaluation of measurement uncertainty, where the evaluation is based on a statistical analysis obtained from repeatable measurements. See Section 7.4.2 for the descriptions of confidence interval and uncertainty. Modified from Grabe (2005).

gives an arithmetic mean $\overline{x} = \sum_{l=1}^{N} x_l / N$. An expectation, $\mu_x$, which is free from random error, would be achieved in the limit if the number of measurements becomes infinite.

### 7.4.2 Evaluation of random and systematic errors

A random error, as mentioned earlier, is the difference between an estimation, $x_l$, and the expectation, $\mu_x$. The evaluation of random error is to establish a confidence interval that can localise the expectation $\mu_x$, based on the data obtainable from a set of estimations. The GUM guideline suggests that a confidence interval follows

$$\overline{x} - \frac{k_P}{\sqrt{N}} s_x \leq \mu_x \leq \overline{x} + \frac{k_P}{\sqrt{N}} s_x \,, \tag{7.7}$$

where $N$ is the number of measurements, $k_P$ is the coverage factor, and $s_x$ is the empirical standard deviation of $X$. The coverage factor $k_P = 1$ defines a standard measurement uncertainty, whereas a higher value defines an expanded measurement uncertainty. Determining the coverage factor $k_p$ from a specified level of confidence $p$ requires knowledge of the distribution of measurement results (see Annex G in ISO (1993) for more information). The empirical variance of $X$ is defined as

$$s_x^2 \;=\; \frac{1}{N-1} \sum_{l=1}^{N} (x_l - \bar{x})^2 \,. \tag{7.8}$$

The empirical standard deviation equals the positive square root of the empirical variance.

Measurement uncertainty must account for both the random error and the systematic error, i.e., the uncertainty must be able to localise the true value with respect to the arithmetic mean. The aforementioned systematic error is the difference between the expectation $\mu_x$ and the true value $x_0$, or $f_x = \mu_x - x_0$. Thus, the uncertainty, localising the true value, is an expansion of the confidence interval that localises the expectation. Figure 7.3 elucidates these relations.

The evaluation of systematic error is subjective. On one hand, given that a rectangular probability distribution represents a systematic error, the uncertainty suggested by GUM is a *geometric combination* between the standard deviations of the random and systematic errors, or

$$u_{\overline{x}} \;=\; k_P \sqrt{\frac{s_x^2}{N} + \frac{f_{s,x}^2}{3}} \,, \tag{7.9}$$

where $f_{s,x}/\sqrt{3}$ is the standard deviation of a rectangular probability distribution that covers $[-f_{s,x}, f_{s,x}]$, which embraces an unknown $f_x$. On the other hand, as a possible alternative to GUM, Grabe assumes a constant systematic error defined over a specific time period (Grabe 1987, Grabe 2001, Grabe 2005). Hence, the analysis of the systematic error is separated from that of the random error, and the uncertainty is an *arithmetic combination* between the confidence interval and the worst case term,

$$u_{\overline{x}} = k_P \frac{s_x}{\sqrt{N}} + f_{s,x} \,. \tag{7.10}$$

In either case, a final measurement result is reported in terms of the arithmetic mean and its uncertainty, or $\overline{x} \pm u_{\overline{x}}$.

Further evaluation of systematic errors in THz-TDS measurement exploits either geometric or arithmetic combination. The selection is based on the nature of the systematic error. If the systematic error is definitive, i.e., it becomes the systematic deviation, the worst-case scenario is adopted. Otherwise, a rectangular distribution and a geometric combination satisfies the analysis.

### 7.4.3 Propagation and combination of measurement uncertainty

Often, a measurand, $\Phi$, is a function of many input quantities, $X_1, X_2, \ldots, X_M$, and $\Phi(X_1, X_2, \ldots, X_M)$ is called a measurement function. In this case the evaluation of uncertainty needs augmentation to account for the propagation and combination of input uncertainties. Possible means of the evaluation can be categorised into two types, numerical or analytical.

An analytical evaluation supported by GUM provides an explicit solution to the propagation and combination of uncertainty. Yet, it requires the linearity assumption of a measurement function in the vicinity of interest. On the other hand, a numerical evaluation, in particular the Monte Carlo method (Weise and Zhang 1997, Joint Committee for Guides in Metrology 2006), has an advantage over its analytical counterpart in that it readily supports the propagation of uncertainty through a nonlinear function (Cox and Harris 1999). Nevertheless, a drawback of the Monte Carlo method is that it is time consuming and, therefore, not flexible. An additional Monte Carlo drawback is that no analytical expression is available, and thus this prohibits further in-depth analysis of the measurement. Nevertheless, a Monte Carlo method is used in validation of the result obtained from the analytical evaluation.

With regard to the analytical evaluation, the propagation of variance, or equivalently, the law of propagation of uncertainty, for the measurement function $\Phi$ is given by

$$s_{\phi}^2 = \sum_{i=1}^{M} \left( \frac{\partial \phi}{\partial \overline{x}_i} \right)^2 s_{x_i}^2 + 2 \sum_{i=1}^{M-1} \sum_{j=i+1}^{M} \frac{\partial \phi}{\partial \overline{x}_i} \frac{\partial \phi}{\partial \overline{x}_j} s_{x_i x_j} \, . \tag{7.11}$$

For the derivation see Appendix C.1. The sensitivity coefficient $\partial \phi / \partial \overline{x}_i$ is calculated at the arithmetic means of the input quantities. This expression also applies to the propagation of the uncertainty of a systematic error that takes on a rectangular distribution. For the propagation of a systematic error that assumes worst-case scenario, the law of error propagation is

$$f_{s,\phi} = \sum_{i=1}^{m} \left| \frac{\partial \phi}{\partial \bar{x}_i} \right| f_{s,x_i} \qquad ; -f_{s,x_i} \leq f_{x_i} \leq f_{s,x_i} \, . \tag{7.12}$$

Both Equations 7.11 and 7.12 are the first-order approximation, and hence valid for a linear or approximately linear measurement function in the region of interest.

The effects of random and systematic errors could be combined either geometrically or arithmetically, as discussed in Section 7.4.2. For example, the combined uncertainty for a measurement function with two input quantities, in case of the geometric combination, is (Grabe 2001)

$$u_{\bar{\phi}} = \frac{k_P}{\sqrt{N}} \sqrt{\left( \frac{\partial \phi}{\partial \bar{x}} \right)^2 \left( s_x^2 + \frac{f_{s,x}^2}{3} \right) + 2 \left( \frac{\partial \phi}{\partial \bar{x}} \right) \left( \frac{\partial \phi}{\partial \bar{y}} \right) s_{xy} + \left( \frac{\partial \phi}{\partial \bar{y}} \right)^2 \left( s_y^2 + \frac{f_{s,y}^2}{3} \right)} \, , \tag{7.13}$$

and in case of the arithmetic combination it becomes (Grabe 2001)

$$u_{\bar{\phi}} = \frac{k_P}{\sqrt{N}} \sqrt{\left( \frac{\partial \phi}{\partial \bar{x}} \right)^2 s_x^2 + 2 \left( \frac{\partial \phi}{\partial \bar{x}} \right) \left( \frac{\partial \phi}{\partial \bar{y}} \right) s_{xy} + \left( \frac{\partial \phi}{\partial \bar{y}} \right)^2 s_y^2} + \left| \frac{\partial \phi}{\partial \bar{x}} \right| f_{s,x} + \left| \frac{\partial \phi}{\partial \bar{y}} \right| f_{s,y} \, , \tag{7.14}$$

where $u_{\bar{\phi}}$ is the uncertainty for a result produced by function $\Phi(X, Y)$.

### 7.4.4 Measurement with resolution limit

The resolution limit of a measuring device can give rise to a systematic error. Occasionally, this error is significant in comparison with the random error in an observation. It is thus suggested that in such cases this limit be incorporated into an expression of uncertainty (Lira and Wöger 1997). Consider the case that a device with its resolution of $\delta$ gives an estimation $x_l$ of a quantity $X$, without any other error. An estimation

of the same measurand obtained from a device with an infinitesimal resolution could be any value in between $x_l \pm \delta/2$, or in practice $x_l + \Delta$. The adjusted term $\Delta$, with a constraint $|\Delta| \leq \delta/2$, is introduced to compensate the imperfect resolution. Obviously, the probability distribution associated with the adjusted term $\Delta$ is rectangular with the variance of $\delta^2/12$. This variance, therefore, contributes to the total variance of $X$, or, mathematically (Lira and Wöger 1997)

$$s_x^2 + \frac{\delta^2}{12}\,, \tag{7.15}$$

where $s_x^2$ is a variance due to random error. In practice, the resolution parameter, $\delta$, is an attribute of a measuring device, and therefore the treatment of resolution limit is a Type B evaluation of uncertainty.

## 7.5 Sources of error in THz-TDS measurement

Many sources of error appear in a THz-TDS measurement and parameter extraction process. Significant sources of error are shown in Figure 7.4, where they are listed along with the parameter extraction process and accompanied by their class (random or systematic). In addition to noise, the sample signal also contains reflections, which, if not dealt appropriately, cause a systematic error. The error in the amplitude from several measurements manifests itself as a variance (or deviation). It propagates down the parameter extraction process, through to the Fourier transform and deconvolution stages, producing the variance in the magnitude and phase of the estimated transfer function. The parameter extraction process requires knowledge of the sample thickness, sample alignment, and air refractive index, each of which have a degree of uncertainty. This step introduces the variances to the estimation. Furthermore, an approximation to the model transfer function gives rise to a systematic error. At the output, all these variances accumulate and contribute to the uncertainty in the extracted optical constants.

Sections 7.5.1 to 7.5.6 provide an analysis for each source of error in detail, including a connection between these errors and the variance in the optical constants. The combination of all variances to produce the uncertainty in the optical constants is given in Section 7.5.7.

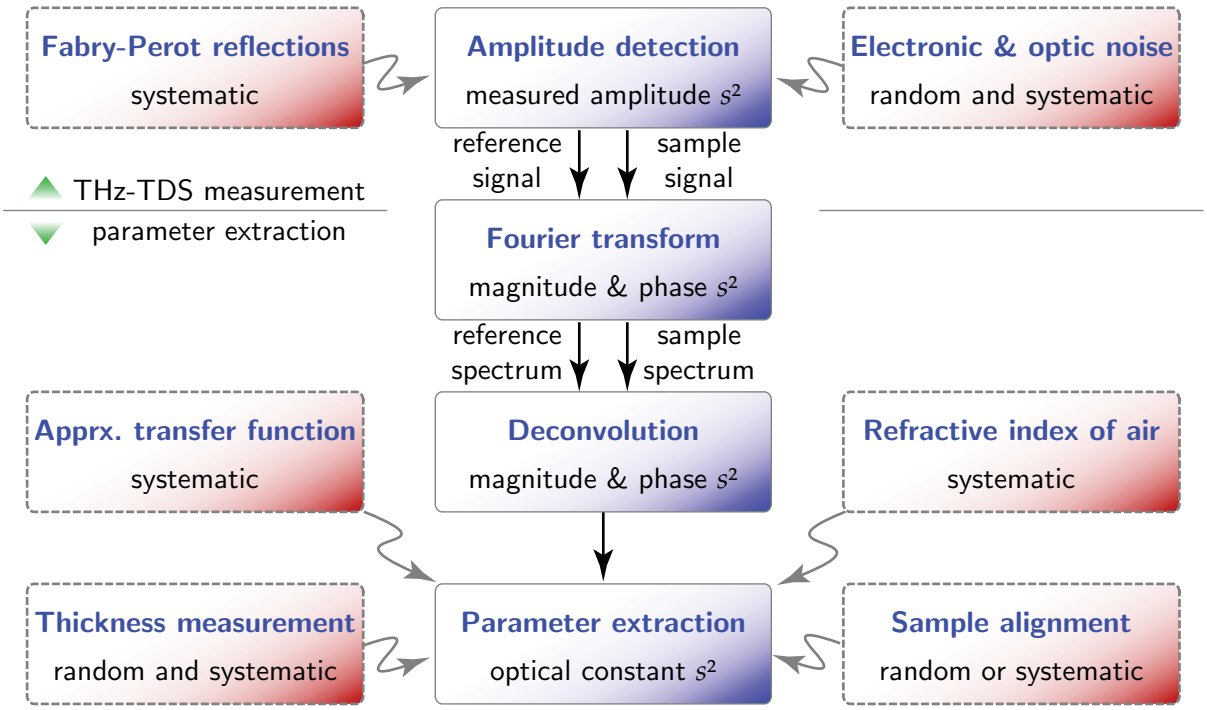


**Figure 7.4. Sources of error in THz-TDS measurement.** The sources of error in the red dashed boxes occur in both the THz-TDS measurement and the parameter extraction process. The errors produced by these sources are classified as either random or systematic. They cause the variances and deviations, which propagate down the process, and eventually contribute to the uncertainty in the extracted optical constants.

### 7.5.1 Random and systematic errors in T-ray amplitude

The T-ray amplitude is prone to variation induced by many sources of random and systematic errors. As mentioned earlier, the sources of random error include laser intensity fluctuation, optical and electronic noise, jitter in the delay stage, etc., whereas the sources of systematic error include registration error, mechanical drift, etc. The variation in the amplitude may embrace the effects from inhomogeneity in a sample or among samples, if the sample is displaced or replaced with nominally identical samples during several measurements. What is considered here is the amplitude variance model, which combines all these errors and assumes a normal probability distribution. This treatment is valid although systematic error is involved, since the systematic error drifts over time and thus cannot be tackled by the method proposed by Grabe (2001), which requires a constant systematic error. The amplitude variance is often statistically obtained from a number of repeated measurements, and thus is regarded as a Type A evaluation.

Regarding the natural difference between two types of error in the T-ray amplitude, a random error occurs in a relatively short time scale, in contrast to a systematic error that can be observed only when the measurement time span is long enough. In addition, the amplitude drift due to the systematic error changes in one direction over time. Due to these facts, recording and averaging signals over a long time span increase the amplitude variation. This scenario is demonstrated in Figure 7.5, in which the drift is larger for a succeeding measurement. Therefore, measuring a T-ray signal is a compromise between the random and systematic errors, i.e., recording over a short time can avoid the drift, but not random error, while recording over a longer period averages out the random error but accentuates the problem of drift.

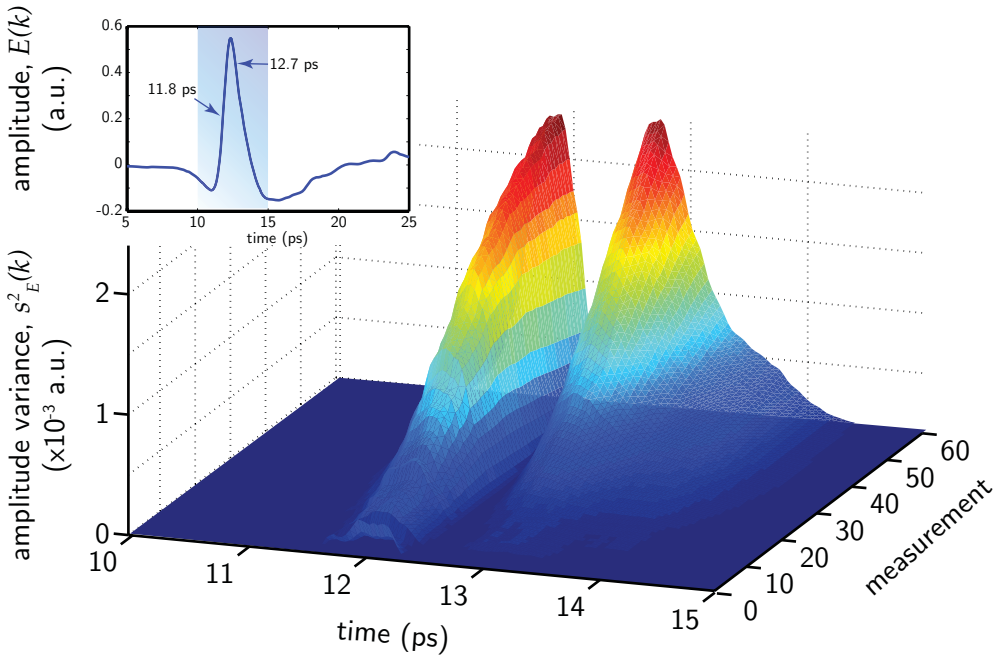


**Figure 7.5. Amplitude variance of measured time-domain signals.** The amplitude variance is plotted against the time and the number of measurements. Any two succeeding measurements are separated by approximately 40 sec. As the number of measurements increases, the variance dramatically increases. The inset shows the arithmetic mean of the 60 measurements. Interestingly, the two peaks in the variance occur at 11.8 and 12.7 ps, whereas the negative and positive peaks in the mean signal are at 11 and 12.4 ps, respectively. The result is most probably dominated by delay-line registration and mechanical drift.

Given the amplitude variances of the time domain reference and sample signals, denoted by $s^2_{E_{\text{ref}}}(k)$ and $s^2_{E_{\text{sam}}}(k)$, respectively, the amplitude-related variances in the optical constants read as

$$s^2_{n,E}(\omega) = \left(\frac{c}{\omega l}\right)^2 \left\{ \frac{A_{\text{sam}}(\omega)}{|E_{\text{sam}}(\omega)|^4} + \frac{A_{\text{ref}}(\omega)}{|E_{\text{ref}}(\omega)|^4} \right\} , \tag{7.16a}$$

$$s^2_{\kappa,E}(\omega) = \left(\frac{c}{\omega l}\right)^2 \left\{ \frac{B_{\text{sam}}(\omega)}{|E_{\text{sam}}(\omega)|^4} + \frac{B_{\text{ref}}(\omega)}{|E_{\text{ref}}(\omega)|^4} + \left(\frac{n(\omega)-n_0}{n(\omega)+n_0}\right)^2 \frac{s^2_{n,E}(\omega)}{n^2(\omega)} \right\} , \tag{7.16b}$$

where

$$A_{\text{sam}}(\omega) = \sum_k \Im^2[E_{\text{sam}}(\omega)\exp(j\omega k\tau)] s^2_{E_{\text{sam}}}(k) , \tag{7.17a}$$

$$A_{\text{ref}}(\omega) = \sum_k \Im^2[E_{\text{ref}}(\omega)\exp(j\omega k\tau)] s^2_{E_{\text{ref}}}(k) , \tag{7.17b}$$

$$B_{\text{sam}}(\omega) = \sum_k \Re^2[E_{\text{sam}}(\omega)\exp(j\omega k\tau)] s^2_{E_{\text{sam}}}(k) , \tag{7.17c}$$

$$B_{\text{ref}}(\omega) = \sum_k \Re^2[E_{\text{ref}}(\omega)\exp(j\omega k\tau)] s^2_{E_{\text{ref}}}(k) . \tag{7.17d}$$

Here, $k$ is the temporal index and $\tau$ is the sampling interval, and thus $k\tau$ is the time. The summation is carried out over the time duration of a recorded T-ray signal. In the equations, all the parameters are calculated at their mean value. For additive noise, $\langle s^2_{E_{\text{ref}}}(k)\rangle = \langle s^2_{E_{\text{sam}}}(k)\rangle$. The derivation for Equation 7.16 can be found in Appendix C.2.

In Equation 7.16, the square of the thickness, $l^2$, is a major factor. Increasing the thickness will seemingly decrease the variance in the optical constants. A physical reason behind this is that, for a very thin sample, the system might not be sensitive enough to detect a small change in the amplitude and phase, which is masked by noise. A thicker sample allows T-rays to interact more with the material, causing a larger change in signal. But, this competes with the fact that $|E_{\text{sam}}(\omega)| \propto \exp(-l)$ and thus increasing $l$ will lower the amplitude of a sample signal and lift the overall variance. A treatment of the thickness-amplitude trade-off can be found in Chapter 8.

Equation 7.16 combines the effects from both the reference and sample signals. For flexibility in some applications, the effects from the two can be separated. Thereby, the variances in the optical constants due to the variance in the sample signal are

$$s^2_{n,E_{\text{sam}}}(\omega) = \left(\frac{c}{\omega l}\right)^2 \frac{A_{\text{sam}}(\omega)}{|E_{\text{sam}}(\omega)|^4} , \tag{7.18a}$$

$$s^2_{\kappa,E_{\text{sam}}}(\omega) = \left(\frac{c}{\omega l}\right)^2 \left\{ \frac{B_{\text{sam}}(\omega)}{|E_{\text{sam}}(\omega)|^4} + \left(\frac{n(\omega)-n_0}{n(\omega)+n_0}\right)^2 \frac{s^2_{n,E_{\text{sam}}}(\omega)}{n^2(\omega)} \right\} . \tag{7.18b}$$

Likewise, the variances in the optical constants due to the variance in a reference signal are

$$s^2_{n,E_{\text{ref}}}(\omega) = \left(\frac{c}{\omega l}\right)^2 \frac{A_{\text{ref}}(\omega)}{|E_{\text{ref}}(\omega)|^4}\,, \tag{7.19a}$$

$$s^2_{\kappa,E_{\text{ref}}}(\omega) = \left(\frac{c}{\omega l}\right)^2 \left\{ \frac{B_{\text{ref}}(\omega)}{|E_{\text{ref}}(\omega)|^4} + \left(\frac{n(\omega)-n_0}{n(\omega)+n_0}\right)^2 \frac{s^2_{n,E_{\text{ref}}}(\omega)}{n^2(\omega)} \right\}. \tag{7.19b}$$

The separation of the effects from the reference and sample allows the evaluation of the uncertainty, where the numbers of measurements for the sample and reference signals are not equal. This separation scheme will be used later in Section 7.5.7, when variances from all sources are combined to yield the overall uncertainty.

### 7.5.2 Random and systematic errors in sample thickness

One parameter that has an influence on the extracted optical constants is the propagation distance of a T-ray beam inside a sample. The propagation distance equals the sample thickness, when the angle of incidence of the beam is normal to the sample surfaces. The variance associated with this thickness is partially due to a random error in thickness measurement, which may be subject to, for example, the mechanical pressure exerted during thickness measurement, the rigidity of a sample, etc. Errors in thickness can also occur due to a change in properties of the sample, for example, a sample of biological tissue can shrink during the experiment due to dehydration or a cryogenically frozen sample can have a different thickness to that measured at room temperature. In addition to the random error, another critical factor contributing to the variance in the thickness is the resolution of a measuring device, deemed systematic error. These two types of error and their impact on the optical constants are evaluated separately, in the following discussion.

#### Random error in sample thickness

Generally, a random error occurring in sample thickness measurements has a normal distribution around a mean value. Given the sample thickness variance $s_l^2$ caused by this error, by referring to the measurement functions in Equations 7.6a and 7.6b, the

thickness-related variances of the optical constants are

$$s^2_{n,l}(\omega) = \left[\frac{n(\omega)-n_0}{l}\right]^2 s^2_l \,, \tag{7.20a}$$

$$s^2_{\kappa,l}(\omega) = \left[\frac{\kappa(\omega)}{l}\right]^2 s^2_l + \left[\frac{c}{n(\omega)\omega l}\left(\frac{n(\omega)-n_0}{n(\omega)+n_0}\right)\right]^2 s^2_{n,l}(\omega) \,, \tag{7.20b}$$

where $s^2_l$ is typically determined from the statistical distribution of several observations, and thus the evaluation is denoted as Type A.

Equations 7.20a and 7.20b indicate that, with no limit, increasing the sample thickness results in a decrease of the variance of the optical constants. However, a thicker sample also results in a weaker sample signal, which eventually gives rise to $s^2_{n,E}(\omega)$ and $s^2_{\kappa,E}(\omega)$ in Equation 7.16.

#### Systematic error in sample thickness (resolution limit)

The resolution of a common thickness measuring device, such as a micrometer or caliper, is relatively limited. This introduces a systematic error to the thickness measurement. As a result, readout values are influenced from the combination of both random and systematic errors. According to the analysis of the resolution limit in Section 7.4.4, the variance in the thickness induced by the resolution limit is $\delta^2_l/12$, where $\delta_l$ is the resolution of a measuring device.

The propagation functions, which link this variance to the variances in the optical constants, are consistent with those in Equation 7.20. Thus,

$$s^2_{n,\delta}(\omega) = \left[\frac{n(\omega)-n_0}{l}\right]^2 \frac{\delta^2_l}{12} \,, \tag{7.21a}$$

$$s^2_{\kappa,\delta}(\omega) = \left[\frac{\kappa(\omega)}{l}\right]^2 \frac{\delta^2_l}{12} + \left[\frac{c}{n(\omega)\omega l}\left(\frac{n(\omega)-n_0}{n(\omega)+n_0}\right)\right]^2 s^2_{n,\delta}(\omega) \,. \tag{7.21b}$$

Because $\delta_l$ is obtained from a published value, the evaluation in Equation 7.21 is regarded as Type B. Similar to the thickness-related variances, the variances here decrease as the thickness increases unless the noise in the signal is considered.

### 7.5.3 Random or systematic error in sample alignment

When the angle of incidence of T-rays on a sample slab is not normal to the surfaces, the transfer function becomes complicated. Specifically, overly tilting the sample will

result in a complex propagation geometry, a deviated beam direction, and a lower T-ray energy focused onto a detector. In order to avoid these complications, the angle of incidence is typically assumed to be normal to the sample's surface, so that a simple transfer function can be adopted.

However, with manual placement and adjustment of the sample, it is likely that a small misalignment can occur. The small misalignment of a sample causes a longer propagation path of T-rays inside the sample, as illustrated in Figure 7.6. A change in the propagation distance consequently affects the estimated optical constants of the sample. The alignment error, therefore, needs to be taken into account in the evaluation of uncertainty in optical constants.

The type of this error is dependent on experimental practice. If the sample is moved in between several measurements, the error is random. On the other hand, if the sample is fixed throughout measurements, the error from the sample alignment is systematic. Despite the possible difference in practice, in this work the error in the sample alignment is considered systematic. The worst-case scenario can bound the error arising from either case.

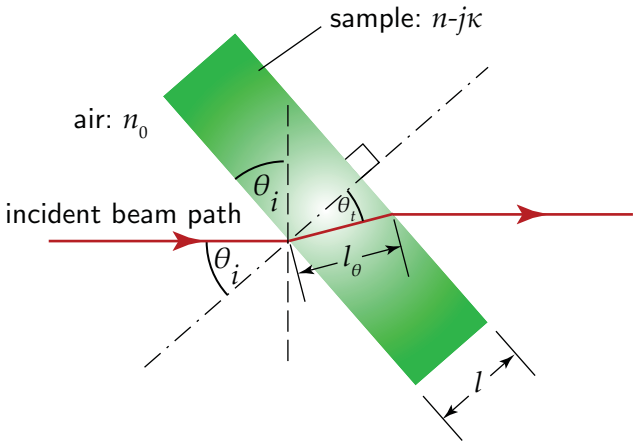


**Figure 7.6. Tilted sample in T-ray beam path.** This exaggerated figure illustrates a small tilt angle from the normal, which might occur due to manual misalignment of the sample. The T-ray path inside the sample, $l_\theta$, is longer than the sample thickness, $l$, by the factor of $1/\cos\theta_t$. The refraction angle, $\theta_t$, is related to the incident angle (and the tilting angle), $\theta_i$, through Snell's law, $n\sin\theta_t = n_0\sin\theta_i$, but for a small tilting angle, $\theta_t \approx \theta_i$.

According to Figure 7.6, the propagation distance inside a sample, $l_\theta$, is a function of the sample thickness, $l$, and the refraction angle, $\theta_t$, or

$$l_\theta = \frac{l}{\cos\theta_t} . \tag{7.22}$$

By assuming that the angle of refraction deviates in a small interval $[-f_\theta, f_\theta]$ and has its arithmetic mean at the origin, the deviation in the propagation distance is thus

$$f_l = l\left(\frac{1}{\cos f_\theta} - 1\right) . \tag{7.23}$$

Note that the numerical evaluation of an error propagation, as in the above equation, is allowed by GUM. Given the deviation in the propagation distance, $f_l$, the alignment-related deviations of the optical constants, derived from Equations 7.6a and 7.6b, are

$$f_{n,\theta}(\omega) = \frac{n(\omega) - n_0}{l} f_l , \tag{7.24a}$$

$$f_{\kappa,\theta}(\omega) = \frac{\kappa(\omega)}{l} f_l + \frac{c}{n(\omega)\omega l} \cdot \frac{n(\omega) - n_0}{n(\omega) + n_0} \cdot f_{n,\theta}(\omega) . \tag{7.24b}$$

Substituting $f_l$ from Equation 7.23 gives

$$f_{n,\theta}(\omega) = [n(\omega) - n_0]\left(\frac{1}{\cos f_\theta} - 1\right) , \tag{7.25a}$$

$$f_{\kappa,\theta}(\omega) = \kappa(\omega)\left(\frac{1}{\cos f_\theta} - 1\right) + \frac{c}{n(\omega)\omega l} \cdot \frac{n(\omega) - n_0}{n(\omega) + n_0} \cdot f_{n,\theta}(\omega) . \tag{7.25b}$$

From the above equations, the deviation in the refractive index due to the sample alignment is independent of the sample thickness, whereas the deviation in the extinction coefficient can reduce for a thicker sample.

### 7.5.4 Systematic error in the approximated transfer function

From Section 7.3.2, regarding the parameter extraction process, it can be seen that the determination of optical constants is based upon an approximated transfer function. This approximation certainly gives rise to an error in the estimated optical constants. But, unlike any other error in the measurement process, the systematic error arising from an approximated transfer function is recognisable and quantifiable. Furthermore, it can be completely removed from the optical constants, if an exact technique for material parameter extraction, such as that given in Duvillaret *et al.* (1996), Duvillaret *et al.*

(1999), or Dorney *et al.* (2001a), is employed. However, a precise approach involves a complicated iterative calculation, and most researchers trade off this complexity with a small error from the approximation. Here, a treatment of the approximation is offered to evaluate the error and to assist the selection of an appropriate approach in determining the optical constants.

In this section, for lucidity, the exact transfer function in Equation 7.3 is referred to as $H_{\text{exact}}(\omega)$, and its approximation in Equation 7.4 is referred to as $H_{\text{appx}}(\omega)$. The phase difference between the approximated and exact transfer functions is

$$\begin{aligned} f_{\angle H}(\omega) &= \angle H_{\text{appx}}(\omega) - \angle H_{\text{exact}}(\omega) \\ &= -\arg\left\{\frac{4\hat{n}(\omega)n_0}{[\hat{n}(\omega)+n_0]^2}\right\} . \end{aligned} \tag{7.26}$$

In a similar way, the magnitude difference between the two functions is

$$\begin{aligned} f_{\ln|H|}(\omega) &= \ln|H_{\text{appx}}(\omega)| - \ln|H_{\text{exact}}(\omega)| \\ &= \ln\left|\frac{4n(\omega)n_0}{[n(\omega)+n_0]^2}\right| - \ln\left|\frac{4\hat{n}(\omega)n_0}{[\hat{n}(\omega)+n_0]^2}\right| \\ &= \ln\left|\frac{n(\omega)}{\hat{n}(\omega)}\left[\frac{\hat{n}(\omega)+n_0}{n(\omega)+n_0}\right]^2\right| . \end{aligned} \tag{7.27}$$

It is now clear that if $\kappa \approx 0$, which makes $\hat{n}(\omega) \approx n(\omega)$, then $f_{\angle H}$ and $f_{\ln|H|}$ become zero.

Derived from the measurement function in Equation 7.6a, the effect of the phase difference on the refractive index deviation is

$$f_{n,H}(\omega) = \frac{c}{\omega l}\left|f_{\angle H}(\omega)\right| . \tag{7.28}$$

Likewise, derived from Equation 7.6b, the effect of the approximated transfer function on the deviation of the extinction coefficient is

$$f_{\kappa,H}(\omega) = \frac{c}{\omega l}\left[\left|f_{\ln|H|}\right| + \frac{1}{n(\omega)}\cdot\frac{n(\omega)-n_0}{n(\omega)+n_0}\left|f_{n,H}(\omega)\right|\right] . \tag{7.29}$$

Obviously, the thickness, $l$, of a sample is an important factor in both $f_{n,H}(\omega)$ and $f_{\kappa,H}(\omega)$. A thicker sample implies a lower contribution to the deviation of the optical constants from the transfer function approximation. A physical explanation is that a thick sample enhances the interaction between T-rays and the bulk material, as indicated by the exponential terms in Equation 7.3. This enhanced interaction dominates the transfer function, and dominates the effect of the approximation in $H_{\text{appx}}(\omega)$.

Here, the values of $n(\omega)$ and $\kappa(\omega)$ are estimated on the basis of a simplified transfer function. Substitution of the approximated values of $n(\omega)$ and $\kappa(\omega)$ into Equations 7.28 and 7.29 can determine the approximated deviations, $f_{n,H}$ and $f_{\kappa,H}$. These deviations are not correction factors for the approximated optical constants, but are rather used to demonstrate the magnitude of the difference between the approximated and the exact values.

### 7.5.5 Systematic error from reflections

In the measurement of a sample, particularly in the case of parallel and shiny surfaces, the reflections at air-sample interfaces always occur, resulting in reflected pulses in a recorded signal. These reflections, or so-called Fabry-Pérot effect, can be removed to some extent from the signal by some means prior to the parameter estimation. Otherwise, the transfer function in Equation 7.4 must be amended to incorporate the Fabry-Pérot effect, as follows:

$$H_{\mathrm{FP}}(\omega) \;=\; \mathrm{FP}(\omega)H(\omega)\,, \tag{7.30}$$

where

$$\mathrm{FP}(\omega) \;=\; \left\{1-\left[\frac{\hat{n}(\omega)-n_0}{\hat{n}(\omega)+n_0}\right]^2\cdot\exp\left[-2j\hat{n}(\omega)\frac{\omega l}{c}\right]\right\}^{-1}\,. \tag{7.31}$$

In this case, the effect must be dealt with during the parameter estimation process by an iterative method such as that of Duvillaret *et al.* (1996). But researchers often prefer using a simple extraction method, in Equations 7.6a and 7.6b, where the Fabry-Pérot effect is ignored. The effect then propagates to the extracted optical constants, where it manifests itself as a systematic error. In response to that, this section proposes an analytical model that can trace the propagation of a Fabry-Pérot effect, now a systematic error, from the spectrum to the optical constants. Quantification of this error can show how large its contribution is toward the optical constants. In addition, the estimated error from the Fabry-Pérot effect has merit in that it can be used to discriminate real absorption features from oscillatory artefacts. If the peak amplitude, i.e., the absorption spectrum subtracted by its baseline, is lower than the estimated Fabry-Pérot oscillation, then the peak is not of importance and can be regarded as an artefact.

Recall that now there are two expressions of the transfer function: one is with the Fabry-Pérot term, $H_{\text{FP}}(\omega)$, and the other is an approximation, $H(\omega)$. The phase difference between the two transfer functions is

$$\begin{aligned} f_{\angle\text{FP}}(\omega) &= \angle H(\omega) - \angle H_{\text{FP}}(\omega) \\ &= -\arg\{\text{FP}(\omega)\} \ . \end{aligned} \tag{7.32}$$

In a similar way, the magnitude difference between the two functions is

$$\begin{aligned} f_{\ln|\text{FP}|}(\omega) &= \ln|H(\omega)| - \ln|H_{\text{FP}}(\omega)| \\ &= -\ln|\text{FP}(\omega)| \ . \end{aligned} \tag{7.33}$$

Derived from the measurement function in Equation 7.6a, the effect of reflections on the refractive index deviation is

$$f_{n,\text{FP}}(\omega) = \frac{c}{\omega l}\left|f_{\angle\text{FP}}(\omega)\right| \ . \tag{7.34}$$

Likewise, derived from Equation 7.6b, the effect of reflections on the deviation of the extinction coefficient is

$$f_{\kappa,\text{FP}}(\omega) = \frac{c}{\omega l}\left[\left|f_{\ln|\text{FP}|}\right| + \frac{1}{n(\omega)}\cdot\frac{n(\omega)-n_0}{n(\omega)+n_0}\left|f_{n,\text{FP}}(\omega)\right|\right] \ . \tag{7.35}$$

Again, the sample thickness plays an important role in scaling the deviation caused by the Fabry-Pérot effect. A longer propagation path within a sample results in a lower deviation of the estimated optical constants. An explanation of this is that a longer T-ray path length in a sample leads to a reduction in the amplitude of reflected pulses in an exponential manner. The reduced amplitude of reflections makes the approximation more reasonable.

In our analysis, the values of $n(\omega)$ and $\kappa(\omega)$ are estimated without considering the Fabry-Pérot effect. Substitution of the approximated values, $n(\omega)$ and $\kappa(\omega)$, into Equations 7.34 and 7.35 can determine the approximated deviations $f_{n,\text{FP}}$ and $f_{\kappa,\text{FP}}$, but not the actual deviations. Thus, $f_{n,\text{FP}}$ and $f_{\kappa,\text{FP}}$ are not correction factors for the optical constants.

### 7.5.6 Systematic error in physical constants

The refractive index of air is slightly larger than unity, and is dependent on the temperature and pressure. The value at 0.89 THz can be estimated from (Chamberlain *et al.*

1965)

$$n_{0,\text{exact}} = 1 + \frac{86.26(5748+T)p}{T^2} \cdot 10^{-6} , \tag{7.36}$$

where $p$ is the partial pressure of water vapour in millimetres of mercury (mmHg) and $T$ is the temperature in Kelvin. At the temperature of 298.15 K (25°C) the *saturated* vapour pressure is 23.76 mmHg—this yields an index offset of $1.4 \times 10^{-4}$.

Nevertheless, the value of unity for air is always adopted instead of this exact calculation in the estimation of the optical constants for the sake of simplicity. Thus, this approximation causes a systematic error, where the sign and magnitude of the variation is known *a priori*. The worst-case analysis is adopted in tracing the propagation of this error to the output optical constants.

From the measurement function in Equation 7.6a, the refractive index deviation due to the air-index deviation is

$$f_{n,n_0}(\omega) = |f_{n_0}| , \tag{7.37}$$

where $f_{n_0} = n_0 - n_{0,\text{exact}}$. Furthermore, from Equation 7.6b, the deviation in the extinction coefficient is

$$f_{\kappa,n_0}(\omega) = \frac{c}{\omega l} \cdot \frac{n(\omega) - n_0}{n(\omega) n_0} f_{n_0} . \tag{7.38}$$

The relation is straightforward and requires no validation by Monte Carlo simulation.

### 7.5.7 Uncertainty in optical constants: A combination of variances

As shown in Sections 7.5.1 to 7.5.6, many sources of error contribute to the variance of the measured optical constants. This section suggests a combination of variances caused by these sources to produce the uncertainty in the optical constants. The combination could be either arithmetic or geometric, dependent on the type of source. The information relating to the combining of variances can be found in Section 7.4.3.

The combined uncertainties for the refractive index and extinction coefficient are estimated by addition of the variances and deviations derived so far, or

$$u_{\overline{n}}(\omega) = k_P \sqrt{\frac{s^2_{n,E_\text{sam}}}{N_{E_\text{sam}}} + \frac{s^2_{n,E_\text{ref}}}{N_{E_\text{ref}}} + \frac{s^2_{n,l}}{N_l} + s^2_{n,\delta}} + f_{n,\theta} + f_{n,H} + f_{n,\text{FP}} + f_{n_0} , \tag{7.39a}$$

$$u_{\overline{\kappa}}(\omega) = k_P \sqrt{\frac{s^2_{\kappa,E_\text{sam}}}{N_{E_\text{sam}}} + \frac{s^2_{\kappa,E_\text{ref}}}{N_{E_\text{ref}}} + \frac{s^2_{\kappa,l}}{N_l} + s^2_{\kappa,\delta}} + f_{\kappa,\theta} + f_{\kappa,H} + f_{\kappa,\text{FP}} + f_{\kappa,n_0} , \tag{7.39b}$$

where the coverage factor $k_P = 1$ is for the standard uncertainty and $k_P > 1$ for an expanded uncertainty; $N_{E_{\text{sam}}}$ and $N_{E_{\text{ref}}}$ are the numbers of measurements for the sample and reference signals, respectively; and $N_l$ is the number of measurements for the sample thickness. Because the sources of error are uncorrelated, no covariance terms appear in the formulas.

It is advised that when the measurement uncertainty is reported, the coverage factor, $k_P$, and all the components used to reckon the uncertainty be listed out, along with their evaluating method, i.e., Type A or Type B evaluation (ISO 1993). Typically, but not always, $s^2_{\{n,\kappa\},E_{\text{sam}}}$, $s^2_{\{n,\kappa\},E_{\text{ref}}}$, and $s^2_{\{n,\kappa\},l}$ are Type A, or statistical observations, whereas the rest of the components are Type B.

The calculation of uncertainty presented in this section follows a recommendation of GUM in that the uncertainty is *directly derivable from* the contributing sources of error, and it is *directly transferable to* other measurands, to which the optical constants are relevant. For example, transferring from the uncertainty in the extinction coefficient to that in the absorption coefficient is via $u_{\overline{\alpha}} = (2\omega/c)u_{\overline{\kappa}}$.

The uncertainty model enables further investigation for dominant sources of error in the system, and also enables optimisation of the measurement. A parametric sensitivity analysis can also be performed with these equations. It should, however, be remembered that the uncertainty model is based on a linear approximation. This low-order approximation is valid in the case where the sources of error have their variation limited to a small vicinity. Section 7.6 validates this approximation by comparing the results with those obtained from Monte-Carlo Simulation (MCS).

## 7.6 Validation of the uncertainty model with MCS

The viability of the uncertainty model given in Equation 7.39 depends on the validity of the propagation models, which link the variance from the error source to that in the optical constants. Derived based on the linear assumption, the propagation models are valid within a certain range around a mean value. In order to validate the analytical models, simulations are set up to observe their results in comparison to the results obtained from Monte Carlo simulation (MCS) or other numerical means, which fully supports the propagation of variance in a nonlinear function.

### 7.6.1 Simulation settings

A T-ray signal is simulated by using the PCA model by Duvillaret *et al.* (2001) (see Appendix B for more information). The parameters of the model are set as follows: the laser pulse duration $\tau_{las} = 120$ fs, the free-carrier recombination time in the emitter and receiver $\tau_{tx} = \tau_{rx} = 300$ fs, and the carrier collision time in the emitter and receiver $\delta\tau_{tx} = \delta\tau_{rx} = 180$ fs. The temporal resolution and temporal window of the simulated signal are 66 fs and 40 ps, respectively. This corresponds to the spectral resolution of 25 GHz. The sample signal is calculated using Equation 7.4 for the case where the experimental parameters are as follows: $n - j\kappa = 3.0 - 0.1j$ ($\kappa = 0.1$ equals $\alpha = 41.9\,\mathrm{cm}^{-1}$ at 1 THz), $l = 100$ $\mu$m, $\theta_i = 0°$, and $n_0 = 1$. Figure 7.7 shows the simulated T-ray reference and sample signals and spectra, in the case that an additive white Gaussian noise limits the maximum dynamic range of the sample spectrum to 20 dB. The magnitude of the spectra decays towards higher frequencies, and thus the bandwidth is limited to 4 THz.

In the simulation, the values of standard deviation for each source of error are selected in order to reflect the range of error present in reality. The simulation results are presented in terms of the standard deviation, $s$, rather than the variance, $s^2$, since the standard deviation has the same dimension as its corresponding parameter, which is more intuitive.

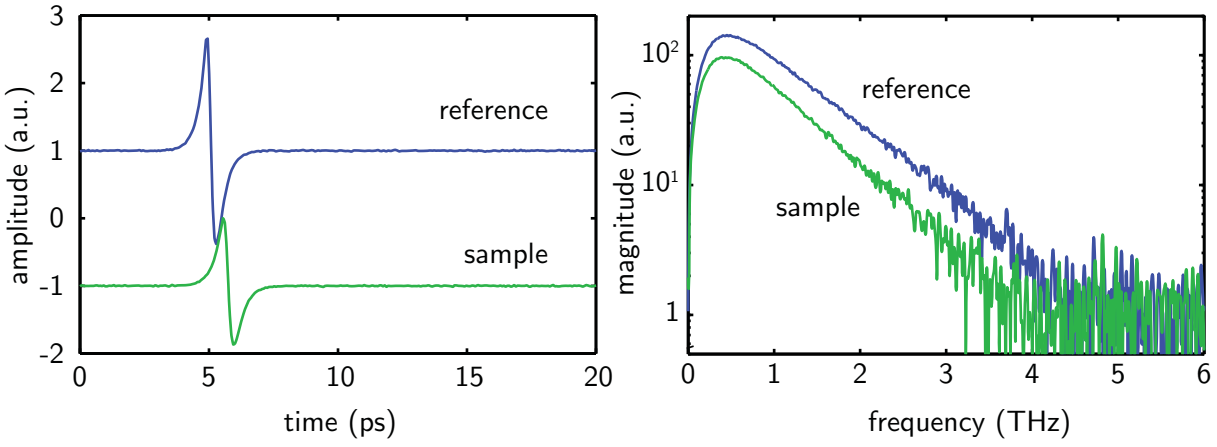


**Figure 7.7. Simulated signals and spectra for reference and sample.** The sample is a 100-$\mu$m-thick dielectric slab, having a complex refractive index of $n - j\kappa = 3.0 - 0.1j$. The simulation model can be found in Appendix B. The white Gaussian noise limits the dynamic range of the sample spectrum to 20 dB, and limits the signal bandwidth to 4 THz. The time-resolved signals are vertically offset for clarity.

### 7.6.2 Random and systematic errors in T-ray amplitude

The proposed analytical model in Equation 7.16, which evaluates the variance in the optical constants as a function of the variance in the signals' amplitude, is validated with MCS. The simulation parameters are given in Section 7.6.1, and the sample signal is calculated using Equation 7.4. In this regard, five different levels of additive Gaussian noise are established in the sample and reference signals, and these levels of noise are preferably referred to in terms of the dynamic ranges of the sample spectrum from 30, 25, 20, 15, to 10 dB. The dynamic range, $D_R$, is related backward to the standard deviation in the amplitude of a signal, $s_E$, via

$$D_R\,(\mathrm{dB}) \;=\; 10\log_{10}\left(\frac{\max E(k)}{2s_E(k)}\right)\,. \tag{7.40}$$

The factor of two multiplying the standard deviation is for the peak-to-peak noise amplitude. Practically, the noise in T-ray signals is, rather than additive, a function of the amplitude, time, and frequency. However, that consideration is not necessary here, as the simulation is intended to demonstrate the ability of the proposed model to transfer the variance resulting from noise to the optical constants through the measurement function.

Figure 7.8 shows the results from the simulation using analytical and numerical methods. In general, as the spectral magnitude decreases towards high frequencies, the standard deviation in the optical constants increases proportionally. By comparing the results from the analytical model and the MCS, it can be seen that a large disagreement occurs at high frequencies, where the SNR is relatively low. This disagreement is not from the limitation of the linear propagation model, because between 0.0 and 0.2 THz, where the SNR is also weak, the results from the two methods still fit reasonably. An explanation is that the noise is too large to recover the meaningful optical constants in the MCS, resulting in an exaggerated standard deviation. This situation is not of concern for the applicability of the proposed analytical model, as the optical constants at this range of low-SNR frequencies must always be discarded. In addition to the disagreement at high frequencies, a small mismatch between the analytical and numerical results occurs below 1 THz in case of $s_{n,E}$. This mismatch is more likely due to the model's assumptions of linearity and vanishing covariance.

Comparison between the standard deviations of the refractive index, $s_{n,E}$, and of the extinction coefficient, $s_{\kappa,E}$, in Figure 7.8 shows that the two deviations are equal in

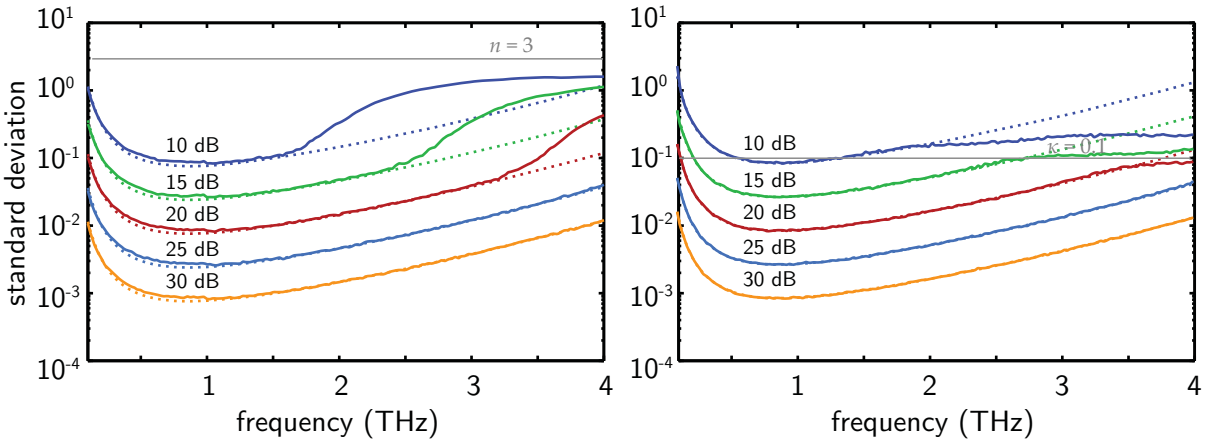


(a) standard deviation of $n$ or $s_{n,E}$ (b) standard deviation of $\kappa$ or $s_{\kappa,E}$

**Figure 7.8. Standard deviation in optical constants due to signal noise.** The solid lines represent results from a Monte Carlo Simulation (MCS), and the dotted lines from the analytical models or Equation 7.16. The indicated dynamic range values are of the sample signal. Each MCS result is from 2000 repetitive runs of the parameter extraction process. The thin grey lines show the level of the optical constants. No vertical offsets have been added to the plot.

magnitude. This situation is general, because Equations 7.16 imply equality. Moreover, as indicated by the grey lines, the magnitude of $\kappa$ is one order lower than of $n$—the condition often found in most dielectric materials. Therefore, this convinces one that, from the same measurement, the refractive index is more precise than the extinction coefficient (and absorption coefficient). The physical reason responsible for this observation remains an open question. The increased precision of the refractive index suggests its higher sensitivity, which could be exploited in some applications, such as T-ray biosensing.

The relatively high precision of $n$ gives rise to a question: Is the extinction coefficient, $\kappa$, converted from $n$ via Kramers-Kronig relation, more reliable that the $\kappa$ from a direct measurement? The answer is no. From the results shown in Figure 7.8, following the projection of $n$ onto the $\kappa$ space, it appears that the standard deviation $s_{n,E}$ would be projected onto the $\kappa$ space with the same scale, leading to a lowered $s_{\kappa,E}$. But in fact, the relation between $s_n$ and $s_\kappa$ through Kramers-Kronig relation is $s_\kappa = s_n/\sqrt{3}$, or $s_\kappa$ is less than $s_n$ by only 57.7% (Riu and Lapaz 1999). Moreover, this projected standard deviation still does not consider the contribution of error from numerical transformation limits, i.e., integration method, a finite number of points, and a restricted frequency

range (Riu and Lapaz 1999). Conclusively, the hypothesis of $s_\kappa$ reduction by using the Kramers-Kronig relation is ruled out.

### 7.6.3 Random and systematic errors in sample thickness

This section shows the validation via MCS of the propagation model in Equation 7.20, which links the variance of the sample thickness to that of the optical constants. The simulation parameters are given in Section 7.6.1, and the sample and reference signals are free from noise. In the simulation, the standard deviation in the sample thickness is varied from 1, 3, 5, 7, to 9 $\mu$m. For the MCS, in each case the sample signal is calculated using Equation 7.4, and the optical constants are extracted using Equations 7.6, with 2000 values of the sample thickness. These thicknesses have a normal distribution with a specified standard deviation. A set of the extracted optical constants is then determined for its standard deviation.

Figure 7.9 illustrates the effect of the variance in the sample thickness on the variance in the optical constants. The thickness considered is in the order of a hundred of microns, whereas the standard deviation is around a few microns. In case of the refractive index in Figure 7.9(a), the analytical model and the MCS yield the agreeable outputs, where $s_{n,l}(\omega) \propto s_l$. For the case of the extinction coefficient in Figures 7.9(b), a large mismatch

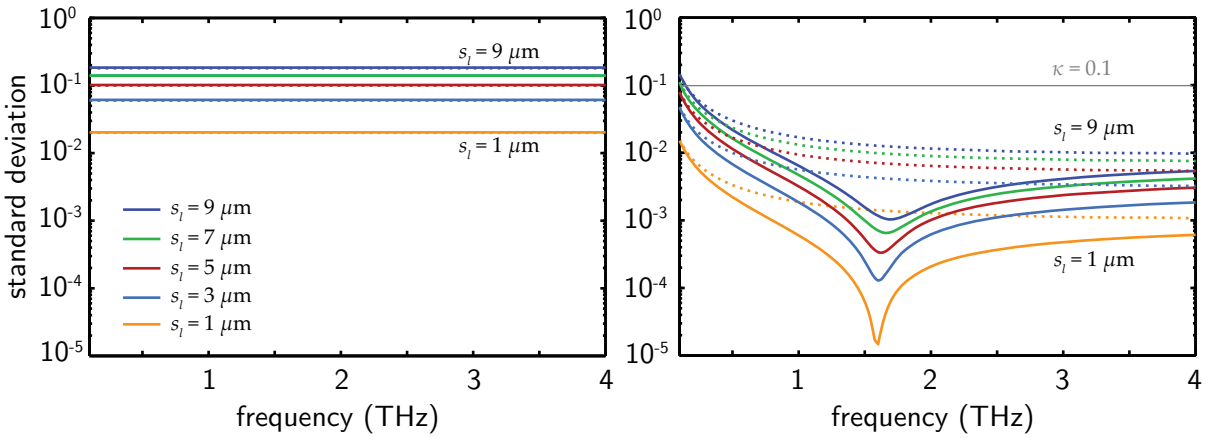


(a) standard deviation of $n$ or $s_{n,l}$ (b) standard deviation of $\kappa$ or $s_{\kappa,l}$

**Figure 7.9. Standard deviation in optical constants due to thickness error.** The solid lines represent results from a Monte Carlo Simulation (MCS), and the dotted lines from the analytical models in Equation 7.20. Each MCS result is from 2000 iterations of the parameter extraction process.

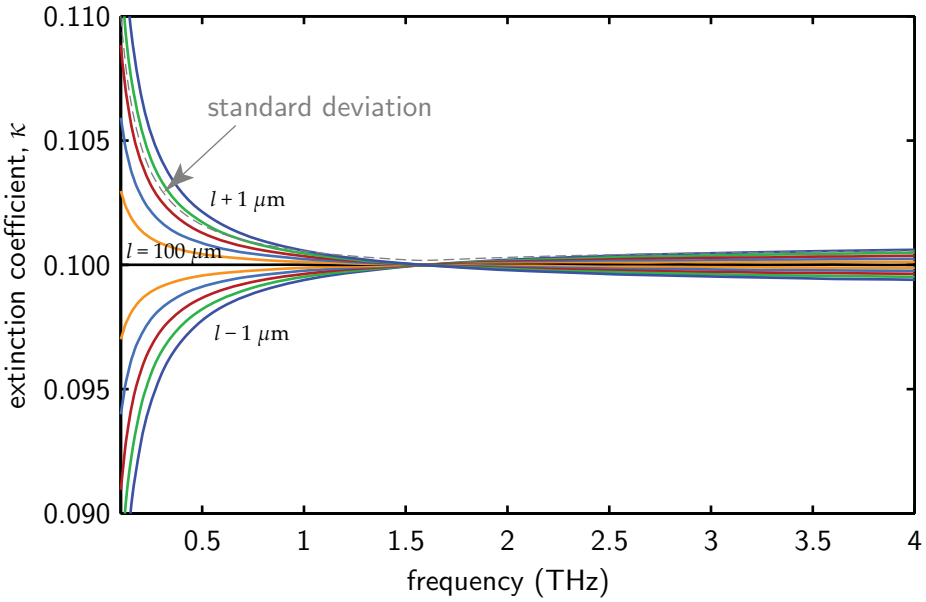


**Figure 7.10. Extracted extinction coefficient at various random thicknesses.** The actual extinction coefficient is 0.1 and is frequency dependent, whereas the actual thickness is 100 $\mu$m. By entering incorrect thicknesses into the parameter extraction process, a series of false coefficients is obtained. The incorrect thickness runs from 99 $\mu$m to 101 $\mu$m with a 0.2 $\mu$m interval.

occurs between the analytical and numerical results, as the $s_{\kappa,l}$ determined from the model is significantly larger than that from MCS, which contains a sharp fall. This mismatch is most likely owing to the limitation of the linear-approximation model. However, the analytical model is still useful, because the calculated variance bounds the actual variance.

Noticeable in Figure 7.9(b), the standard deviation estimated from the MCS shows an irregular profile, i.e., a sharp fall, as a function of the frequency. The cause of that irregularity is manifested in Figure 7.10, where the extinction coefficient is estimated at several incorrect thicknesses. It is obvious that if the thickness used in the parameter extraction deviates from the actual thickness, the coefficient becomes a function of the frequency and crosses its actual value at a certain frequency. The situation can be explained mathematically by referring to the parameter extraction in Equation 7.6. Substituting the measured magnitude and phase in Equation 7.5 into Equation 7.6 gives

$$n_{\text{est}} = n_0 + \frac{c}{\omega l_{\text{est}}}\left\{[n_{\text{act}} - n_0]\frac{\omega l_{\text{act}}}{c}\right\}, \tag{7.41a}$$

$$\kappa_{\text{est}} = \frac{c}{\omega l_{\text{est}}}\left\{\ln\left[\frac{4n_{\text{est}}n_0}{(n_{\text{est}}+n_0)^2}\right] - \ln\left[\frac{4n_{\text{act}}n_0}{(n_{\text{act}}+n_0)^2}\right] + \kappa_{\text{act}}\frac{\omega l_{\text{act}}}{c}\right\}. \tag{7.41b}$$

The subscript 'act' denotes an actual value hidden in the measured magnitude and phase, and 'est' for an estimated value. If $l_{\text{est}} = l_{\text{act}}$, then $n_{\text{est}} = n_{\text{act}}$, and the actual value of the extinction coefficient can be obtained. On the other hand, if $l_{\text{est}} \neq l_{\text{act}}$, then $n_{\text{est}} \neq n_{\text{act}}$. Consequently, the logarithmic terms in Equation 7.41b do not vanish, leaving $\kappa_{\text{est}}$ as a function of the reciprocal of the frequency. In this regard, the frequency where the thickness-related variance of $\kappa$ is lowest, or the thickness-invariant frequency, could possibly be exploited in some particular applications.

Note that since the propagation of variances that originate from the resolution limit and the sample alignment exploits a similar model to that in Equation 7.20, which is already validated in this section, their propagation models do not require a further validation.

### 7.6.4 Systematic deviation from approximated transfer function

This section verifies the applicability of the proposed models in Equations 7.28 and 7.29, which evaluate the influence of the transfer function approximation on deviation in the optical constants. Because the models provide the deviation, rather than the variance, the results can be compared directly to the exact deviation without having recourse to an MCS analysis. The setting of the simulation is similar to that described in Section 7.6.1, except for the value of the extinction coefficient which runs from 0.001, 0.01, 0.1, to 1, while the sample thickness is fixed at 100 $\mu$m. In another situation, the sample thickness varies from 50, 100, 500, to 1000 $\mu$m while $\kappa = 0.1$. In each case, the sample signal is calculated using Equation 7.3, and the optical constants are extracted using Equation 7.6. The exact deviation is the difference between the extracted optical constants and their true value. The estimated deviation is obtained by substituting the extracted optical constants and the related parameters into the proposed analytical models in Equations 7.28 and 7.29. Figure 7.11 depicts the resultant deviations.

Clearly, the deviation decreases gradually towards higher frequencies, where the effect of the approximation is lessened. In case that the thickness is fixed and the extinction

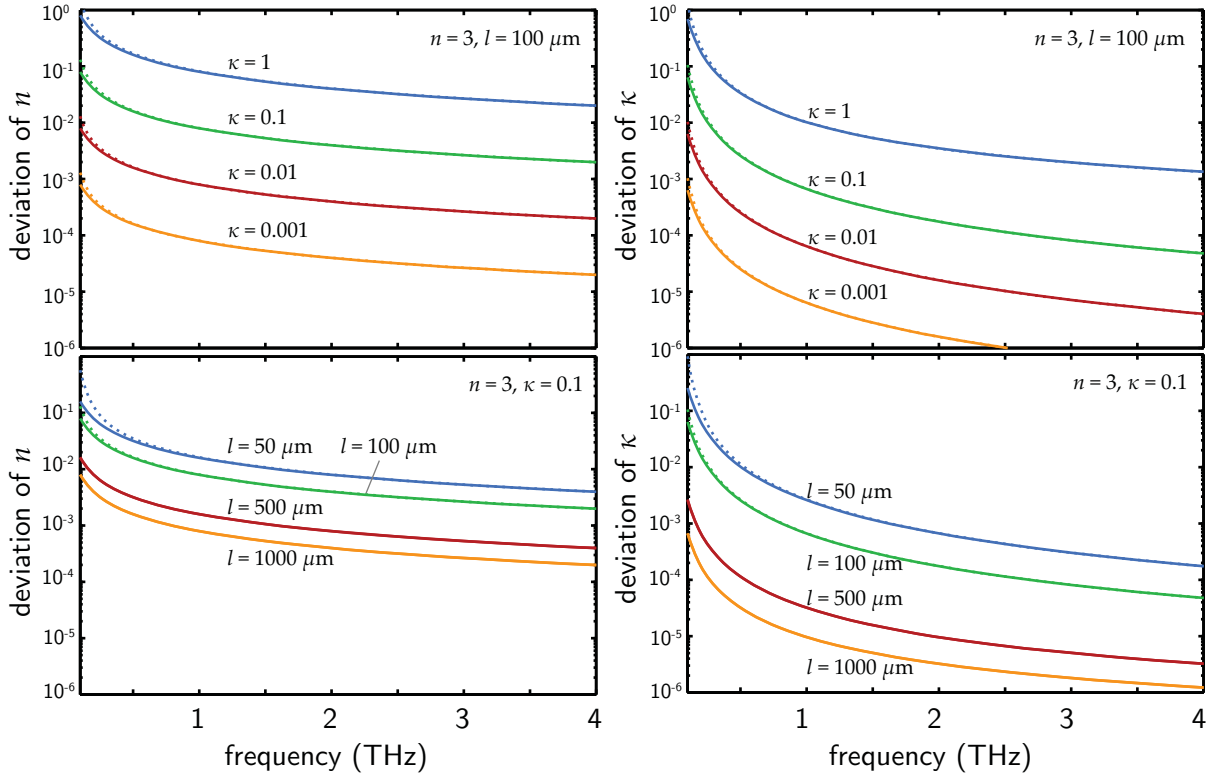


(a) deviation of $n$ or $f_{n,H}$ (b) deviation of $\kappa$ or $f_{\kappa,H}$

**Figure 7.11. Deviation in optical constants due to transfer function approximation.** The solid lines represent the exact deviations. The dotted lines are the results from the proposed analytical models in Equations 7.28 and 7.29.

coefficient reduces, the deviation reduces proportionally. This is because a lower $\kappa$ means that $\hat{n} = n - j\kappa$ is closer to $n$ and subsequently the approximation of the transfer function is more valid. On the other hand, if $\kappa$ is fixed and the thickness reduces, the deviation increases. A reduction in the sample thickness results in a lower contribution from bulk material interaction that influences the transfer function. Meanwhile, the effect of transmission at the interfaces is more pronounced, invalidating the approximation.

By comparing the analytical and numerical results, it can be seen that the proposed analytical model can estimate the deviation in the optical constants for a broad range of $\kappa$ and $l$, with a reasonable error from the approximated $n$ and $\kappa$. But for a thin sample at low frequencies, the model seems to encounter a limit. As discussed earlier, a thin sample means that the factor of the transmission at air-sample interfaces becomes more important and eventually invalidates the approximation. Substituting the optical

constants with a large deviation into Equations 7.28 and 7.29 to estimate the deviation is therefore not recommended.

### 7.6.5 Systematic deviation from reflections

As shown in Section 7.5.5, ignoring the Fabry-Pérot term from the parameter extraction process, whereas the reflections are present in the signal, gives rise to a systematic error in the optical constants. This section verifies the proposed models in Equations 7.34 and 7.35, which estimate this type of error analytically. The simulation parameters are the same as those described in Section 7.6.1, but now the temporal window of a signal is extended from 40 ps to 120 ps, to accommodate reflections, which arrive with a longer delay. For the fixed sample thickness at 100 $\mu$m, two values of the extinction coefficient, 0.001 and 1, are simulated. For the fixed extinction coefficient at 0.1, the sample thickness varies from 50, 100, 500, to 1000 $\mu$m. In each case, the sample signal is calculated using Equation 7.4 with the consideration of the Fabry-Pérot effect, and the optical constants are extracted using Equation 7.6, where the effect is ignored. The exact deviation is the difference between the extracted optical constants and their true value. The estimated deviation is obtained by substituting the extracted optical constants and the related parameters into the proposed analytical models in Equations 7.34 and 7.35. Figure 7.12 shows the deviations of the optical constants obtained from these calculations.

A general trend which can be observed for all results is that the deviation decreases towards higher frequencies. In addition, a sample with a larger thickness or a higher absorption tends to result in a lower deviation of the optical constants, implying less influence from the reflections. This is because in a sample with a long propagation path or with a high absorption, the reflections are more absorbed and diminished from a measured signal, and thus the estimated optical constants are closer to the actual value. In contrast, for a sample with a low thickness or a low absorption, the reflections are chiefly present in a measured signal, resulting in a large deviation in an estimation of the optical constants.

Comparison between the numerical and analytical results shows no difference at a low value of deviation. The higher deviation means the estimated optical constants contain more error introduced by the reflections. Substituting the optical constants

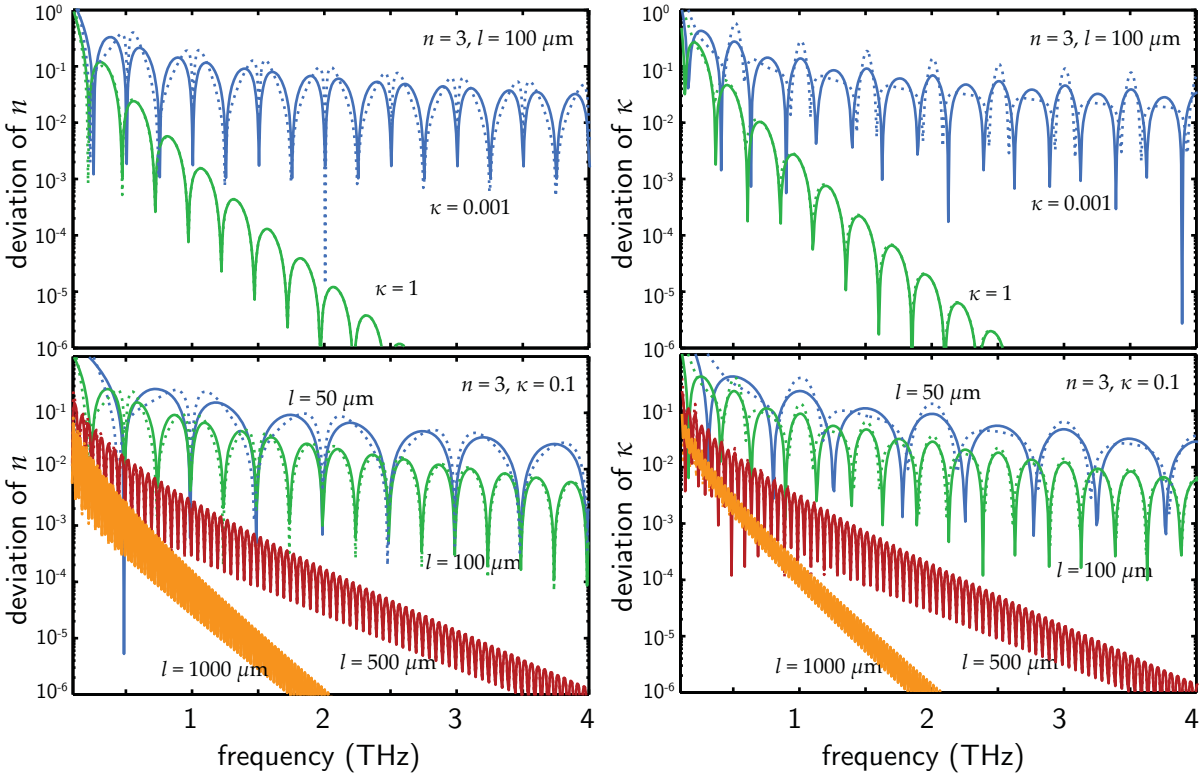


(a) deviation of $n$ or $f_{n,\mathrm{FP}}$ (b) deviation of $\kappa$ or $f_{\kappa,\mathrm{FP}}$

**Figure 7.12. Deviation in optical constants due to reflections.** The solid lines represent the exact deviations. The dotted lines are the results from the proposed analytical models in Equations 7.34 and 7.35.

with a large deviation into the analytical models in Equations 7.34 and 7.35 to estimate the deviation, hence, gives results with a large error.

## 7.7 Practical implementation

The analytical models for the propagation of variance, developed and validated in the earlier sections, are implemented with a set of T-ray measurements to demonstrate the functionality. The measurements are carried out with a lactose sample by a free-space transmission T-ray spectrometer.

The THz-TDS system in use employs photoconductive antennas (PCA) at the transmitter and receiver. The pump laser is a mode-locked Ti:sapphire laser with a pulse duration of 15 fs and a repetition rate of 80 MHz. This generates the T-ray pulse with a FWHM of 0.4 ps, and its bandwidth spans from 0.1 to 3 THz. The time constant for the

lock-in amplifier is set to 30 ms. The surrounding atmosphere is purged with nitrogen to eliminate the effects of water vapour.

The lactose sample is prepared by mixing 25 mg of $\alpha$-lactose monohydrate with HDPE powder and pressing the mixture using a hydraulic press into a solid disk with a diameter of 13 mm and a thickness of 1.85 mm. The sample is placed at the focal plane between two off-axis parabolic mirrors. These mirrors have a focal length of 100 mm and the collimated beam incident on the first mirror has a diameter of 35 mm. According to the theory of Gaussian beam optics (Saleh and Teich 1991), the depth of focus, i.e., twice the Rayleigh length, is 2 mm for the 3-THz wavelength. Thus, the sample thickness of 1.85 mm is thinner than the depth of focus of the highest-frequency component. In addition, the largest waist diameter of the beam is 11 mm for the 0.1-THz component, smaller than sample's diameter, and thus does not lead to edge diffraction.

The reference and sample signals are measured alternately to assure that the drift in the signal amplitude does not influence the result. The reference and sample signals are both measured 10 times. The time between two consecutive measurements is 6 min on average. Figure 7.13 shows the mean values of the reference and sample signals, along with their standard deviations. No reflections are observed in the sample signal.

Measured by a micrometer with a resolution $\delta = 1$ $\mu$m, the pellet of lactose has an average thickness of 1.85 mm in the propagation direction, and the standard deviation of the thickness from 10 measurements is $s_l = 5$ $\mu$m. Let us suppose as a worst-case that the tilting angle of the lactose sample during the measurements has a rectangular distribution around the origin, bounded by $f_\theta = \pm 2^\circ$. Throughout the measurement, the ambient temperature is approximately 25°C and the humidity is 60%—this corresponds to the saturated vapour pressure of 23.76 mmHg and the partial pressure of 14.26 mmHg. According to Equation 7.36, the refractive index of air is $\approx 1.0001$.

Shown in Figure 7.14 are the optical constants of the lactose/HDPE pellet, $n$ and $\kappa$, their standard deviations, $s_n$ and $s_\kappa$, their deviations, $f_n$ and $f_\kappa$, and the combined uncertainties, $u_n$ and $u_\kappa$, plotted on a logarithmic scale. The optical constants are determined from a pair of the averaged reference and sample signals, using the measurement functions in Equations 7.6a and 7.6b. The standard deviations, the deviations, and the uncertainties are evaluated by using the proposed analytical models. For comparison, the standard deviations of $n$ and $\kappa$ due to the amplitude variation, or $s_{n,E}$

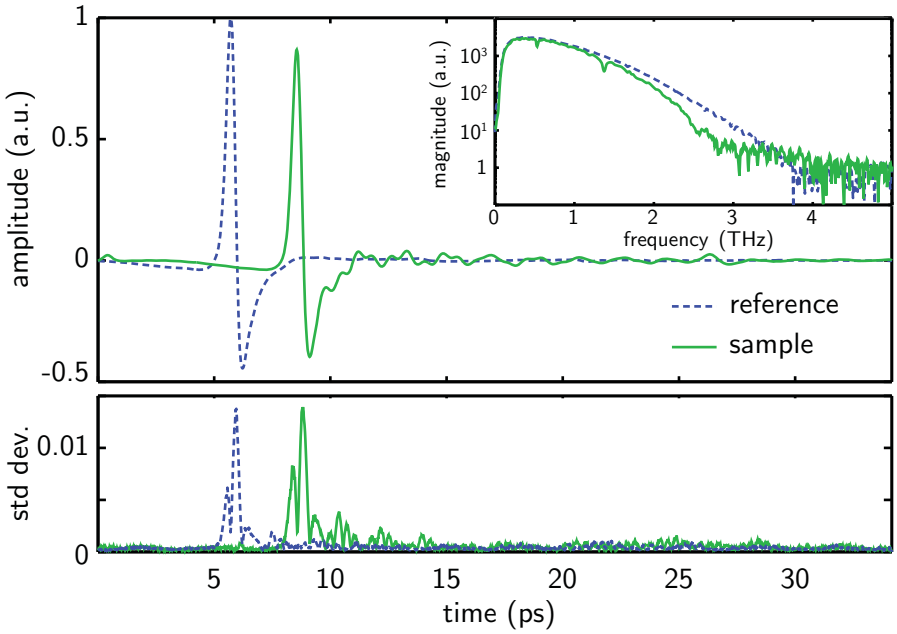


**Figure 7.13. Average signals and standard deviations for reference and lactose.** The reference and lactose signals, each, are averaged over 10 measurements. The signals have a temporal resolution of 0.0167 ps, and a total duration of 34.16 ps. The inset shows the spectra of the reference and sample.

and $s_{\kappa,E}$, are also evaluated numerically from the ten profiles of their respective values, available from ten pairs of the reference and sample signals. The analytical and numerical evaluations appear to provide comparable values of $s_{\kappa,E}$ or $s_{n,E}$. The slight mismatch is likely caused by the first-order approximation in the analytical model.

The refractive index appears constant at $n \approx 1.46$, but actually varies slightly with the frequency. The extinction coefficient, on the other hand, is strongly dependent on the frequency, and varies in between 0.001 and 0.01; two absorption resonances at 0.53 and 1.37 THz reproduce those reported in Fischer *et al.* (2005b). The variation in the T-ray amplitude gives rise to $s_{n,E}$ and $s_{\kappa,E}$ equally. Because the extinction coefficient is lower than the index of refraction by two orders of magnitude or more, the extinction coefficient is thus significantly affected by $s_{\kappa,E}$. Interestingly, the standard deviation in $n$ caused by the thickness variance, or $s_{n,l}$, is higher than the standard deviation caused by the amplitude variance $s_{n,E}$. The deviations from the limited thickness resolution, $s_{n,\delta}$ and $s_{\kappa,\delta}$; from the tilting angle, $f_{n,\theta}$ and $f_{k,\theta}$; and from the offset in refractive index, $f_{n_0}$ and $f_{\kappa,n_0}$, are less than the optical constants' levels by four orders of magnitude, and are deemed insignificant. The transfer function approximation causes a significant impact in the case of the extinction coefficient, since at low frequencies the value of $f_{\kappa,H}$

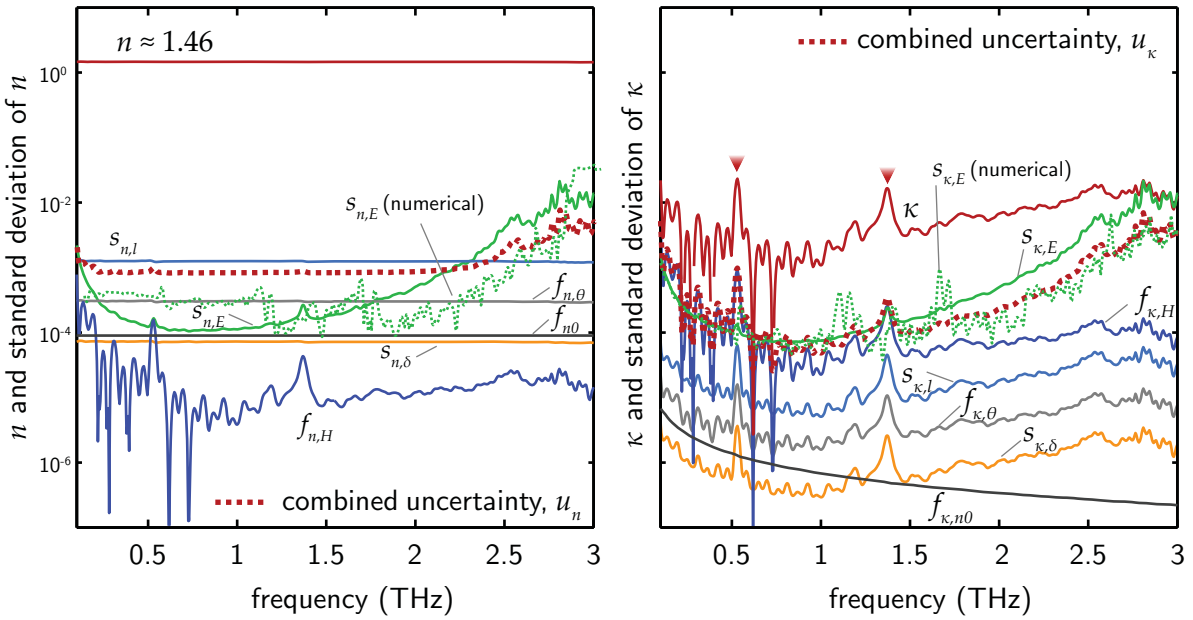


(a) standard deviation of $n$ or $s_n$ (b) standard deviation of $\kappa$ or $s_\kappa$

**Figure 7.14. Uncertainty for lactose measurement.** The combined uncertainties in the optical constants are plotted in comparison to the mean values of the optical constants and the standard deviations introduced by various sources of error. The combined uncertainty is calculated with the coverage factor $k_P = 1$. Both subfigures share the same vertical scale. In (a), the refractive index of the lactose/HDPE pellet is approximately 1.46, compared to its combined uncertainty of $10^{-3}$. The major sources contributing to the combined uncertainty are signal noise and thickness uncertainty. In (b), the extinction coefficient is in the order of $10^{-3}$, compared to its combined uncertainty in the order of $10^{-4}$. The major source contributing to the combined uncertainty is signal noise. The arrowheads indicate the low-frequency resonances of $\alpha$-lactose at 0.53 and 1.37 THz.

is close to the value of $s_{\kappa,E}$. Note that no deviation from the reflections is evaluated here, as the reflections are not present in the signal.

The uncertainties $u_n$ and $u_\kappa$ are evaluated with the coverage factor $k_P$ of 1. It can be seen that the uncertainties are dominated by the effects from the amplitude variation, $s_{n,E}$ or $s_{\kappa,E}$. The values of $u_n$ and $u_\kappa$ become larger at higher frequencies, where the magnitude of the sample and reference spectra is low. The tendency of the uncertainties with respect to the spectral position is similar to that of the results reported in Bolivar *et al.* (2003), in which a similar THz-TDS system is used in characterisation of some dielectric materials.

## 7.8 Conclusion and potential extensions

Previously, the analysis of the sources of error in a THz-TDS measurement emphasised the noise in a signal caused by electronic, optical, and mechanical components. Yet, other sources of random and systematic errors, introduced during the signal measurement and throughout the parameter extraction process, were overlooked. It is thus of great importance to have an analysis that can quantify and relate the error from many sources to the final parameters, i.e., the optical constants.

This work presents the evaluation of uncertainty in a THz-TDS measurement, with a particular focus on a transmission mode measurement. Several sources, which contribute to the measurement error, are identified. The relation between the variance or deviation from each of these sources and that in the optical constants is derived. All the contributing variances and deviations, affecting the optical constants, are combined to give the total uncertainty in the measurement. The derived analytical models are successfully validated with the Monte Carlo method or other numerical means. A test of the models with experimental T-ray data obtained from lactose measurements also provides validation, which enables a further comparative study of error from each part of a THz-TDS system. The evaluation of uncertainty in this work, where applicable, follows the guideline proposed in GUM (ISO 1993).

It should be noted that our assumption of a perfect sample results in the absence of some sources of systematic and random errors, which could contribute to the uncertainty in the optical constants. These sources are, e.g., the lack of parallelism of the sample surfaces and the inhomogeneity and scattering by the sample (Franz *et al.* 2008). Apart from those sample-related imperfections, a number of optical effects are omitted from the widely used transfer function model, or Equation 7.3. These effects, particularly arising from a beam-focusing configuration, include frequency-dependent beam shape (beam waist at the focal point, Rayleigh length, beam divergence) (Gürtler *et al.* 2000), and beam defocusing by the sample. Treatment of these effects is appropriate for future work.

The proposed model is applicable to any THz-TDS system, which produces sample's response in compliance with Equation 7.3. An adaptation of the model to deal with the reflection mode THz-TDS or other tailored THz-TDS systems is feasible. Further accuracy in the evaluation of uncertainty, at an additional computational expense, can be obtained by considering a higher-order analysis (Lira 2002) or a numerical approach,

such as a Monte Carlo method (Joint Committee for Guides in Metrology 2006), which is accepted as a supplementary to GUM.

The promising results in this chapter suggest that the proposed uncertainty model offers a standard for evaluation of uncertainty in transmission THz-TDS measurements. Therefore, measurements from different laboratories can be compared on the same basis. The number of repeated measurements depends on the nature of the error, i.e., if the error does not drift over a given time span, the number of measurements should be maximised; otherwise, if drift is observed, a different methodology is required. Another benefit of the proposed model is that it enables analytical optimisation and sensitivity analysis for some measurement parameters, which often results in reduction of the measurement uncertainty. As an example, the optimisation of a sample's thickness is determined based on this analysis, and will be presented in Chapter 8.

"*. . . The evaluation of uncertainty is neither a routine task nor a purely mathematical one: it depends on detailed knowledge of the nature of the measurand and of the measurement. The quality and utility of the uncertainty quoted for the result of a measurement therefore ultimately depend on the understanding, critical analysis, and integrity of those who contribute to the assignment of its value.*"

GUM (ISO 1993)

Chapter 8

# Material Thickness Optimisation for THz-TDS

HOW thick should a sample be for a transmission-mode THz-TDS measurement? Should a sample be as thick as possible? The answer is 'no'. Although greater thickness allows T-rays to interact more with bulk material, the SNR rolls off with thickness due to signal attenuation. So, should a sample be extremely thin? Again, the answer is 'no'. A sample that is too thin renders itself nearly invisible to T-rays, in such a way that the system can hardly sense the difference between the sample and a free space path. Hence, where is the optimal boundary between 'too thick' and 'too thin'? The optimal trade-off is analysed and revealed in this Chapter, where our approach is to find the optimal thickness that results in the minimal uncertainty of measured optical constants.

## 8.1 Introduction

In a transmission measurement, a THz-TDS system generates and detects coherent broadband pulses, which, once transmitted through a sample, have their shape changed in accordance with the sample's frequency response. This enables estimation of optical constants, or related quantities, of the sample from the measured pulses. Recent developments for the system mainly aim for wider bandwidth (Huber *et al.* 2000, Liu *et al.* 2004b) and faster scan rates (Jiang and Zhang 2000, Bartels *et al.* 2006, Yasui *et al.* 2005). Another important aspect that needs consideration is the uncertainty in the extracted optical constants.

The uncertainty in the optical constants is deemed crucial in many THz-TDS applications. Some applications that require a low uncertainty in measurement include quantifying the sample amount (Jacobsen *et al.* 1996, Strachan *et al.* 2005, Gorenflo *et al.* 2006), determining resonance frequencies (van Exter *et al.* 1989b), etc. In certain cases, a lower uncertainty assists the interpretation of data at a critical point. An example is when a small resonance is overwhelmed by noise, resulting in an ambiguous observation. In such a case, reducing the uncertainty in the measurement could resolve the issue.

A major contribution to the uncertainty in the measured optical constants is from the fluctuations and noise in the measured signals, which are mainly due to electronic (van Exter and Grischkowsky 1990b), optical (Poppe *et al.* 1998), and mechanical (Cohen *et al.* 2006) components. Thus, in order to reduce the uncertainty in optical constants, one may attempt to tackle the noise in the signals directly. It is known that using a lock-in amplifier with an optical chopper to modulate T-ray signals (Mittleman *et al.* 1996) can reduce $1/f$ noise due to laser fluctuations. Also increasing the signal strength in the first place helps to lessen the effect of electrical and optical noise sources, by increasing the SNR. However, both of these approaches cannot solve the problem of mechanical drift. Alternatively, multiple scans are taken so that repeated measurements can be averaged in an attempt to reduce noise—however, this does not work if mechanical drift manifests between successive scans. A further approach to reduction of the uncertainty in optical constants is hidden in the details of sample geometry and its optimisation—for the first time we now analyse this case and back up our theory with experimental results in this chapter.

It is well known to every THz-TDS experimentalist that, in transmission-mode spectroscopy, a sample that is too thick has considerable bulk absorption and can significantly reduce the signal power. In fact, the upper bound of the thickness for a given absorption value is determined from the system's dynamic range (Jepsen and Fischer 2005). Therefore, a sample is usually made very thin as long as it can be mechanically supported. However, a sample that is too thin can also cause problems, as the system might not be sufficiently sensitive to detect the resultant changes in the amplitude and phase of the signal. Both thickness extremes result in higher uncertainty in the measured optical constants. In this chapter, the optimal trade-off between the two extremes is determined, in order to minimise the uncertainty in optical constants.

This chapter is organised as follows: In Section 8.3, an analytical model relating the variance in signals to the variance in optical constants is introduced. This model leads to the optimisation of the sample thickness based on minimisation of the variance in optical constants, as shown in Section 8.4. An analytical formula for optimum thickness is verified by THz-TDS experiments with various materials in Section 8.5. The usage of the formula is discussed in Section 8.6.

## 8.2 Research objective and framework

### Objective

To determine the thickness of a sample optimised for a transmission-mode THz-TDS measurement. The optimality, of the sample thickness, results in minimum noise-related uncertainty of the measured optical constants. The optimisation is carried out analytically, with the model relating the variance in measured time-domain signals to the variance in extracted optical constants.

### Framework

For the THz-TDS measurement considered here, our working assumptions are that (i) the measurement is in transmission mode, (ii) the sample under test is a homogeneous dielectric slab with parallel flat surfaces, where the scattering of T-rays is negligible, (iii) the angle of incidence of the T-ray beam is normal to the sample surfaces, (iv) the T-ray beam is well collimated, and (v) the reference signal is measured under the same condition as the sample signal, except for the absence of the sample.

## 8.3 Uncertainty in optical constants

The amplitude of T-ray signals is prone to noise induced by many sources. These sources include laser intensity fluctuations, optical and electronic noise, jitter in the delay stage, alignment error, mechanical drift, etc. Whilst most of the sources of error obey a normal distribution, alignment error and mechanical drift do not. However, via the Central Limit Theorem (Feller 1945, Trotter 1959), we might expect the resultant of all the errors tends towards a normal distribution. Hence, considered here is an amplitude variance model, which unifies all these errors and assumes a normal probability distribution. The influence of this amplitude variance on the uncertainty in extracted optical constants is shown in this section.

Given that the sample under a transmission-mode measurement has parallel and polished surfaces, and the angle of incidence of the incoming T-ray beam is normal to the surfaces, the transfer function of the sample is expressed as

$$H(\omega) = \frac{E_{\text{sam}}(\omega)}{E_{\text{ref}}(\omega)} = \tau\tau' \cdot \exp\left\{-\kappa(\omega)\frac{\omega l}{c}\right\} \cdot \exp\left\{-j[n(\omega) - n_0]\frac{\omega l}{c}\right\} , \tag{8.1}$$

where $E_{\text{ref}}(\omega)$ and $E_{\text{sam}}(\omega)$ are the reference and sample signals in the frequency domain, $l$ is the sample thickness, $n(\omega)$ and $\kappa(\omega)$ are the refractive index and the extinction coefficient of the sample, $n_0$ is the refractive index of air, and $\tau$ and $\tau'$ are the transmission coefficients at the sample interfaces. The refractive index and the extinction coefficient, together called the optical constants, can be deduced from Equation 8.1 as

$$n(\omega) = n_0 - \frac{c}{\omega l}\angle H(\omega) , \tag{8.2a}$$

$$\kappa(\omega) = \frac{c}{\omega l}\left\{\ln|\tau\tau'| - \ln|H(\omega)|\right\} . \tag{8.2b}$$

Influenced by the variance in measured signals, the variances in refractive index, $s_n^2(\omega)$, and in extinction coefficient, $s_\kappa^2(\omega)$, can be derived from Equation 8.2 using the law of propagation of uncertainty. In brief, from the signal amplitudes in the time domain, the variance is transferred to the variance of the magnitude and phase spectra in the frequency domain via Fourier transform. Then the combination between the variances of sample and reference measurements produces the variance in the transfer function of a sample. The variance eventually appears over the optical constants. From this analysis, the variances in the refractive index and in the extinction coefficient are given

by, respectively,

$$s_n^2(\omega) = \left(\frac{c}{\omega l}\right)^2 \left\{ \frac{A_{\text{sam}}(\omega)}{|E_{\text{sam}}(\omega)|^4} + \frac{A_{\text{ref}}(\omega)}{|E_{\text{ref}}(\omega)|^4} \right\} , \tag{8.3a}$$

$$s_\kappa^2(\omega) = \left(\frac{c}{\omega l}\right)^2 \left\{ \frac{B_{\text{sam}}(\omega)}{|E_{\text{sam}}(\omega)|^4} + \frac{B_{\text{ref}}(\omega)}{|E_{\text{ref}}(\omega)|^4} + \left(\frac{n(\omega) - n_0}{n(\omega) + n_0}\right)^2 \frac{s_n^2(\omega)}{n^2(\omega)} \right\} , \tag{8.3b}$$

where

$$A_{\text{sam}}(\omega) = \sum_k \Im^2[E_{\text{sam}}(\omega) \exp(j\omega k\Delta)] s_{E_{\text{sam}}}^2(k) , \tag{8.4a}$$

$$A_{\text{ref}}(\omega) = \sum_k \Im^2[E_{\text{ref}}(\omega) \exp(j\omega k\Delta)] s_{E_{\text{ref}}}^2(k) , \tag{8.4b}$$

$$B_{\text{sam}}(\omega) = \sum_k \Re^2[E_{\text{sam}}(\omega) \exp(j\omega k\Delta)] s_{E_{\text{sam}}}^2(k) , \tag{8.4c}$$

$$B_{\text{ref}}(\omega) = \sum_k \Re^2[E_{\text{ref}}(\omega) \exp(j\omega k\Delta)] s_{E_{\text{ref}}}^2(k) . \tag{8.4d}$$

Here, $s_{E_{\text{ref}}}^2(k)$ and $s_{E_{\text{sam}}}^2(k)$ are the variances associated with the reference and sample signals, respectively; $k$ is the sampling index number and $\Delta$ is the sampling interval, and thus $k\Delta$ is the time; $\Re^2$ and $\Im^2$ denote the square of real and imaginary parts, respectively. The summation is carried out over the time duration of the recorded T-ray signal. In the equations, all parameters utilize mean values. The proposed model in Equation 8.3 is successfully validated with Monte Carlo method. The complete derivation for Equation 8.3 can be found in Appendix C.2.

## 8.4 Optimisation of the sample thickness

From Equations 8.3a and 8.3b in Section 8.3, it can be inferred that four major variables, $n(\omega)$, $\kappa(\omega)$, $l$, and $|E_{\text{ref}}|$, govern the amplitude-related variance, $s_n^2$ or $s_\kappa^2$. Optimising one of these parameters might help reduce the variance. Two of them, $n(\omega)$ and $\kappa(\omega)$, are intrinsic to materials, and thus cannot be optimised. The signal strength, $|E_{\text{ref}}|$, without doubt, must be as large as possible—provided there is no damage to the sample—in order to minimise the variance. The sample thickness, $l$, can usually be controlled and thus may lend itself to optimisation.

The intricate relation between the sample thickness and the standard deviation in the refractive index, $s_n$, is simulated and demonstrated via a contour plot in Figure 8.1. As we can see, at every frequency, there is an optimum sample thickness that gives the

lowest $s_n$. Figure 8.2 reveals the magnitude of $s_n$ and $s_\kappa$ as a function of the thickness, estimated at three different example frequencies. The optimum thicknesses for the simulated sample at these frequencies approximately span 300 $\mu$m to 1 mm. Moving towards a thicker sample by an order of magnitude sees an increment of the standard deviation by three orders. Moreover, moving towards a thinner sample by an order of magnitude results in increased standard deviation by one order of magnitude. Selecting the sample thickness to correspond to desired minimum in Figure 8.2 is therefore advantageous.

According to the transfer function in Equation 8.1,

$$|E_{\text{sam}}(\omega)|^4 \;=\; (\tau\tau')^4 \exp\left\{-4\kappa(\omega)\frac{\omega l}{c}\right\} |E_{\text{ref}}(\omega)|^4 \,. \tag{8.5}$$

Substituting Equation 8.5 into Equation 8.3a and reassigning the notation gives

$$s_n^2(\omega) \;=\; \frac{C}{l^2}\left\{\frac{A'_{\text{sam}}(\omega)}{\exp(-4\kappa\omega l/c)} + A_{\text{ref}}(\omega)\right\} \,, \tag{8.6}$$

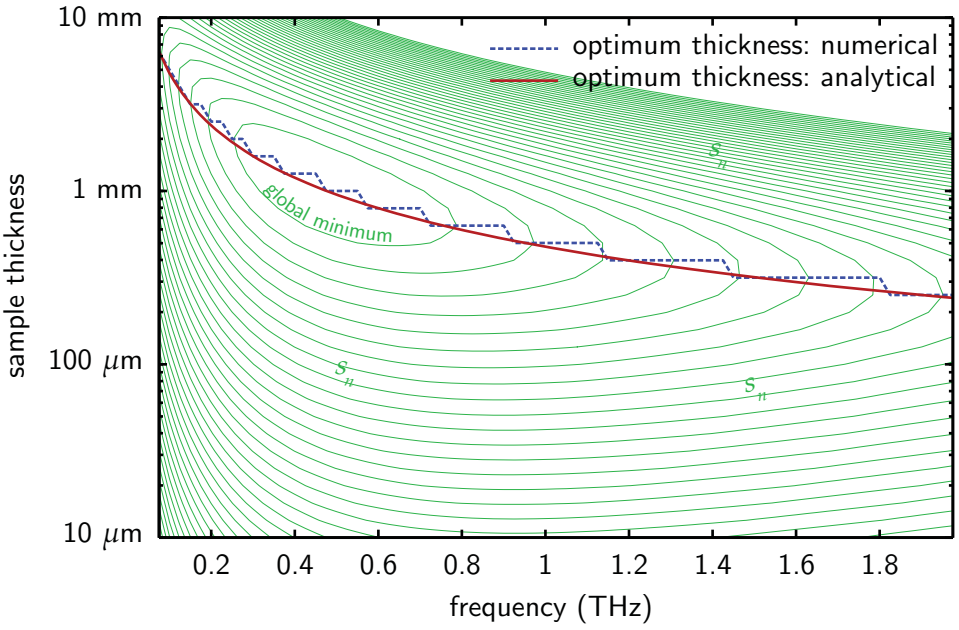


**Figure 8.1. Standard deviation in refractive index against thickness and frequency.** The contours represent the simulated magnitude of $s_n$, which is in fact comparable to that of $s_\kappa$. The optical constants are set to $n - j\kappa = 3.0 - 0.1j$ at all frequencies ($\kappa = 0.1$ equals $\alpha = 41.9$ cm$^{-1}$ at 1 THz). Additive white Gaussian noise limits the maximum dynamic range of the reference spectrum to 40 dB. The position of the global minimum relative to the frequency corresponds to the peak position of the reference spectrum. The plot for the optimum thickness determined numerically appears jagged due to the discrete nature of the simulation.

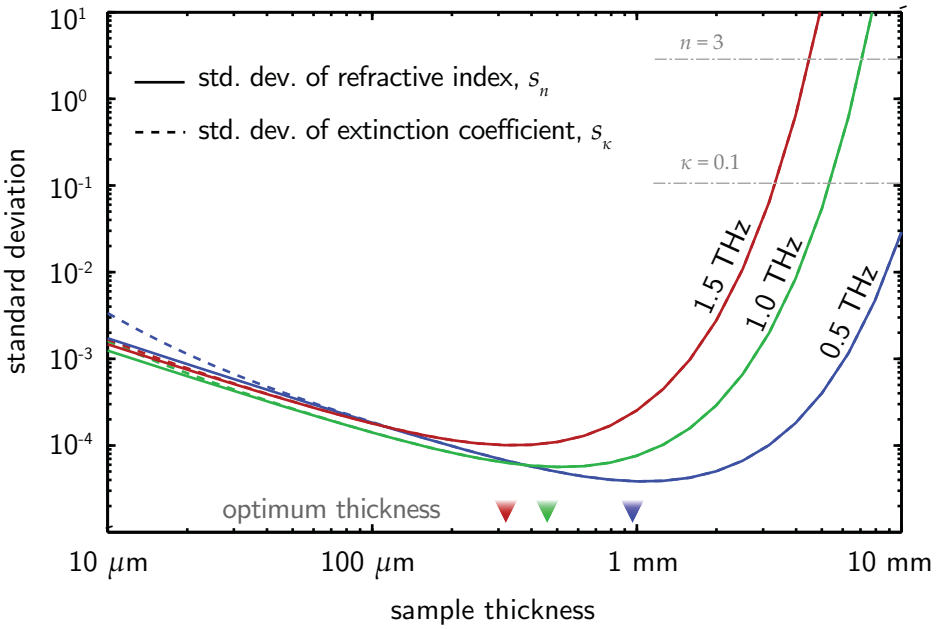


**Figure 8.2. Standard deviation in optical constants against sample thickness.** The plots are cross-sectional profiles of Figure 8.1, at selected frequencies 0.5, 1.0, and 1.5 THz. The optimum thicknesses, where the standard deviation is minimal, are indicated by arrowheads. By moving towards a thicker sample, the standard deviation rapidly increases to the point comparable to the values of the optical constants. The standard deviation at high frequency is more sensitive to the thickness increment, as the T-ray magnitude at high frequencies is relatively low.

where

$$C = \frac{c^2}{\omega^2 |E_{\text{ref}}(\omega)|^4} \qquad \text{and} \qquad A'_{\text{sam}}(\omega) = \frac{A_{\text{sam}}(\omega)}{(\tau\tau')^4} \,. \tag{8.7}$$

Assuming that $s_E^2$ in $A(\omega)$ is not a function of $l$, we are now able to minimise $s_n^2(\omega)$ with respect to the thickness $l$. By taking the derivative of Equation 8.6 with respect to $l$, we arrive at

$$\frac{\partial s_n^2(\omega)}{\partial l} = \left(4\frac{C}{l^2}\frac{\kappa\omega}{c} - 2\frac{C}{l^3}\right)\frac{A'_{\text{sam}}(\omega)}{\exp(-4\kappa\omega l/c)} - 2\frac{C}{l^3}A_{\text{ref}}(\omega) \,. \tag{8.8}$$

The variances in the reference and sample spectra, $A_{\text{ref}}(\omega)$ and $A_{\text{sam}}(\omega)$, can be related via the transfer function, as does the magnitude of the spectra in Equation 8.5,

$$A_{\text{sam}}(\omega) \approx (\tau\tau')^4 \exp\left\{-4\kappa(\omega)\frac{\omega l}{c}\right\} A_{\text{ref}}(\omega) \,. \tag{8.9}$$

Note that the dependency of $A_{\text{sam}}(\omega)$ on the sample thickness is an approximation, and does not affect the optimisation. Substituting Equation 8.9 into Equation 8.8 and

**Table 8.1. Optimum sample thickness for some common materials.** The optimum thickness for THz-TDS measurement is determined using Equation 8.11. The absorption coefficients, measured at room temperature, are taken from various sources: water (Thrane *et al.* 1995); PMMA, TPX (Fischer 2005); HDPE (Jin *et al.* 2006). Note that the absorption coefficient can widely vary from sample to sample, in particular for plastics.

| Material | 0.5 THz | | 1.0 THz | | 1.5 THz | |
|---|---|---|---|---|---|---|
| | $\alpha$ (cm$^{-1}$) | $l_{\text{opt}}$ | $\alpha$ (cm$^{-1}$) | $l_{\text{opt}}$ | $\alpha$ (cm$^{-1}$) | $l_{\text{opt}}$ |
| Water | 150 | 130 $\mu$m | 200 | 100 $\mu$m | – | – |
| PMMA | 5 | 4 mm | 20 | 1 mm | 40 | 0.5 mm |
| HDPE | 2.0 | 10 mm | 2.2 | 9.1 mm | 2.4 | 8.3 mm |
| TPX | 0.1 | 20 cm | 0.5 | 4 cm | 0.8 | 2.5 cm |

equating to zero gives,

$$\left(4\frac{C}{l^2}\frac{\kappa\omega}{c} - 2\frac{C}{l^3}\right) A_{\text{ref}}(\omega) - 2\frac{C}{l^3}A_{\text{ref}}(\omega) \;=\; 0\,, \tag{8.10}$$

and further manipulation yields the optimum thickness:

$$l_{\text{opt}} = \frac{c}{\omega\kappa(\omega)} = \frac{2}{\alpha(\omega)}\,. \tag{8.11}$$

The resultant optimum thickness obtained using Equation 8.11 is in accordance with the result obtained numerically, as demonstrated in Figure 8.1.

By substituting the optimum thickness in Equation 8.11 into Equation 8.5 and ignoring reflection at the interfaces, we see that a sample with optimum thickness attenuates the magnitude of the incident pulse by the factor of $1/e$. The optimum thickness turns out to be a distance that is equal to twice the penetration depth. Optimisation of the sample thickness by starting from Equation 8.3b also delivers the same outcome. Notice that the optimum thickness, $l_{\text{opt}}$, relies on neither the index of refraction, $n(\omega)$, nor the signal magnitude, $|E(\omega)|$. This is because the transmittance at the sample interfaces is not a function of thickness. In addition, the sensitivity of the detector is not involved, as the analysis aims for minimisation of the uncertainty, i.e., stability of the measurement, for a given sensitivity.

In Table 8.1, some common dielectric materials with their optimal thicknesses are given, according to Equation 8.11. In addition, it appears that the resultant thickness calculated from this equation is in close agreement with the result found numerically in

Mickan *et al.* (2004), in which the optimisation is for a differential thickness THz-TDS measurement. For example, at 1 THz, the optimum thickness for dioxane, which has $\kappa = 0.013$ or $\alpha = 5.45\ \mathrm{cm}^{-1}$, is reported to be 4 mm, and the optimum thickness for water, $\kappa = 0.478$ or $\alpha = 200\ \mathrm{cm}^{-1}$, is 100 $\mu$m (Mickan *et al.* 2004). Using the same parameters, the derived analytical expression given in Equation 8.11 estimates the thicknesses for dioxane and water to be 3.7 mm and 100 $\mu$m, respectively.

## 8.5 Experiments and results

The experiments are performed using a fiber-coupled T-ray Picometrix 2000 system, equipped with photoconductive antennas for T-ray generation and detection. The pumping laser is a mode-locked Ti:Sa laser (MaiTai, Newport) with a central wavelength of 800 nm, a pulse duration of $<$80 fs, and a repetition rate of 80 MHz. The system generates pulsed T-ray radiation spanning 0.05 to 1.5 THz, with a maximum dynamic range of 30 dB. The collimated beam diameter is approximately 25.4 mm. The sample materials that are used in this study are PVC, PE, and water, which have unique absorption characteristics. The reference measurement is made with a free path in two runs, ten scans each, before and after every run of ten individual sample measurements. The similarity of the variances of the two runs confirms no significant change to the hardware during sample measurement.

### 8.5.1 Polyvinyl chloride: PVC

The measurement is carried out with normal-grade PVC, which is preformed in a rod shape. The rod with a diameter of 50 mm is cut into four cylindrical segments, with the thickness of 1 (0.967), 10 (9.977), 20 (19.869), and 50 (50.338) mm—the values in parentheses are the average of five measurements with one standard deviation of $\approx \pm 0.005$ mm. The surfaces of these samples are well polished to minimise scattering. Each sample is measured with a collimated beam from the THz-TDS system in the axial direction for ten scans, and each scan is made after the previous scan within 30 sec.

#### Optical constants

The optical constants of PVC are extracted from the measurements of the 10-mm sample. The phase at low frequencies is extrapolated from the phase value between 0.05

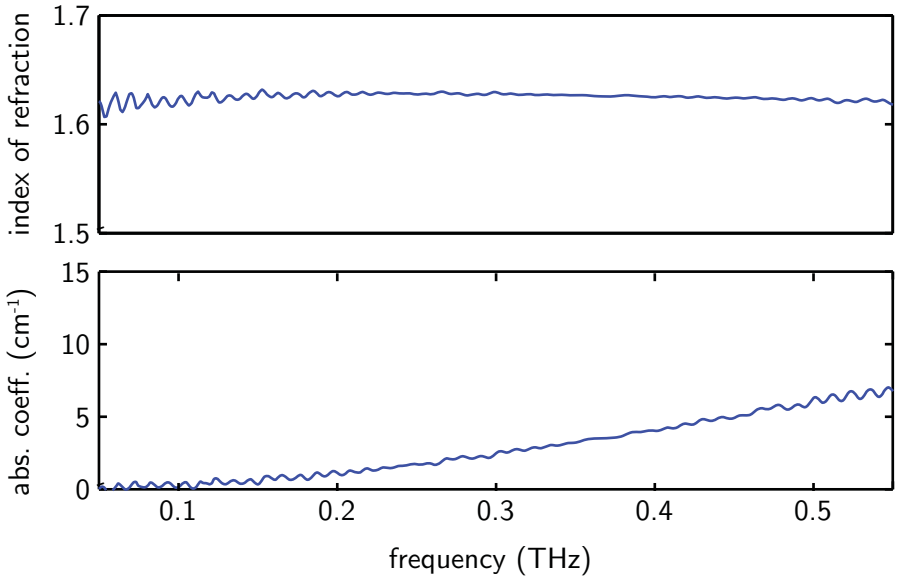


**Figure 8.3. Optical constants of PVC.** The constants are calculated from the average signal probing a 10-mm-thick sample. The available bandwidth of the measurement is from 0.05 to 0.55 THz. The ripples in the curves are due to Fabry-Pérot reflections.

and 0.1 THz. Figure 8.3 shows the extracted optical constants. Clearly, the refractive index is nearly constant at 1.63, lower than the previously published value at 1.67 (Piesiewicz *et al.* 2007). The absorption coefficient increases quadratically, also in accordance with (Piesiewicz *et al.* 2007). Note that small shifts in the refractive indices of plastics at T-ray frequencies are known to be caused by slight hygroscopicity (Balakrishnan *et al.* 2009b) and differences in the manufacturing process.

### Optimum thickness

The optimum thickness for PVC, which supposedly yields the lowest variance in the measured optical constants, is determined from the absorption coefficient using the proposed model in Equation 8.11. However, the measured absorption coefficient contains error from noise, water-vapour absorption, and Fabry-Pérot fringes. By assuming that the absorption coefficient is well described by a parametric function, the measured coefficient is initially smoothed by a second-order polynomial, which also enables extrapolation of the coefficient towards a higher frequency range. Figure 8.4 illustrates the optimum thickness determined directly from the measured coefficient and from the fitting model. It can be seen that at frequencies around 1.0 THz, a sample thickness of 1 mm would provide the lowest variance of the optical constants. In addition, at low frequencies the optimum thickness increases by around one order of magnitude.

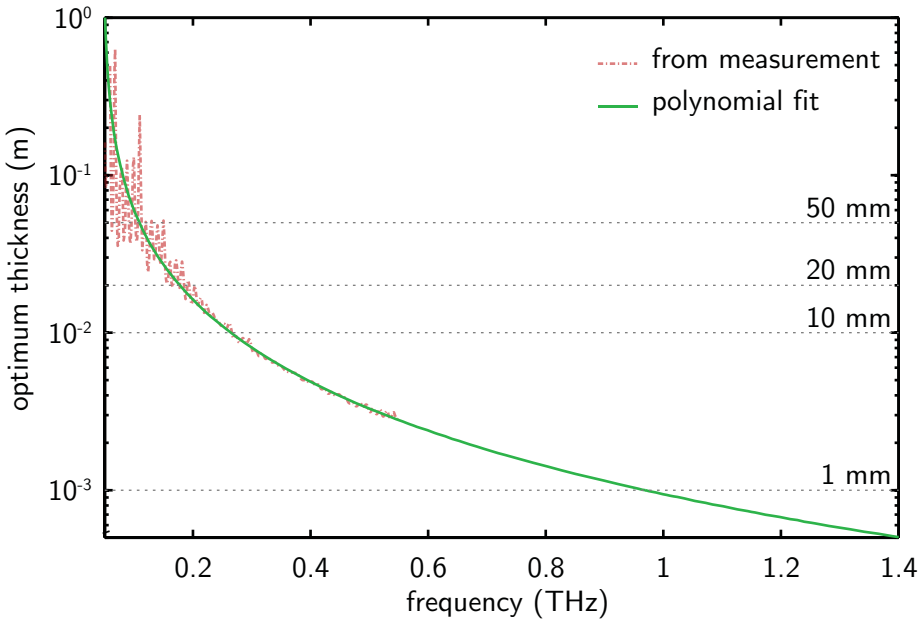


**Figure 8.4. Optimum thickness for PVC.** The optimum thickness is determined from the measured absorption coefficient. The solid line is a second-order polynomial fit to the absorption coefficient between 0.05 and 0.55 THz. The horizontal dotted lines indicate the sample thicknesses of 1, 10, 20, and 50 mm, available for the measurements.

### Standard deviation

Figure 8.5 shows the standard deviations of the optical constants for the four PVC samples, in terms of the unprocessed scatter plots and the fitting parametric curves. It is evident that at 0.05-0.2 THz, the 50-mm-thick sample provides the lowest standard deviation among the four samples; at 0.2-0.25 THz, the 20-mm-thick sample; at 0.25-0.6 THz, the 10-mm-thick sample; and above 0.6 THz, the 1-mm-thick sample. This optimum relation is in perfect agreement with the prediction in Figure 8.4, which is derived using the proposed optimal-thickness model. The improvement in measurement accuracy can be observed, for example, by comparing the standard deviations of the 1-mm-thick and 50-mm-thick sample. At around 0.1 THz the standard deviation for the thicker sample is $\approx 4 \times 10^{-5}$, and that for the thinner sample is $\approx 2 \times 10^{-3}$, or the improvement of the standard deviation is by almost two orders of magnitude.

## 8.5.2 High-density polyethylene: HDPE

The material used in this experiment is a high-density polyethylene (HDPE), supplied as a long cylindrical rod with a diameter of 50 mm. The rod is sliced into six samples,

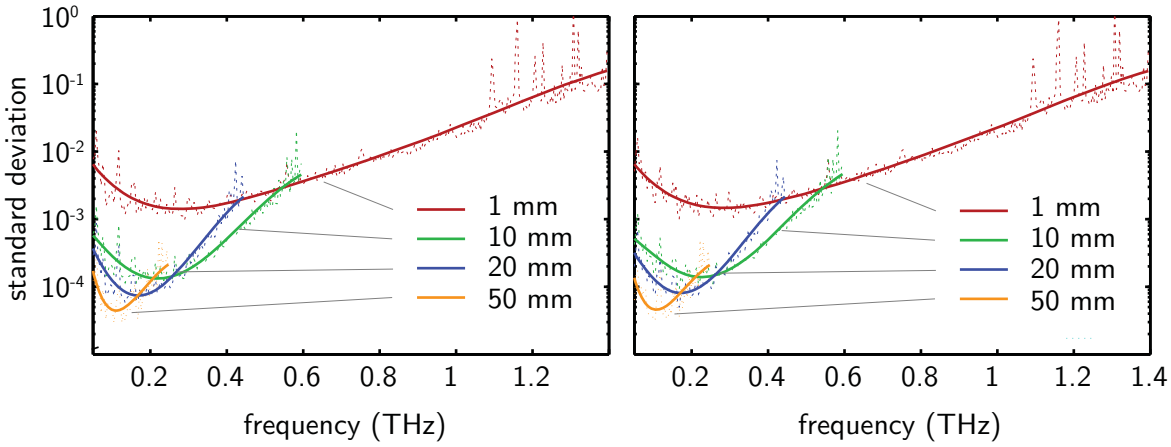


(a) standard deviation of $n$ (b) standard deviation of $\kappa$

**Figure 8.5. Standard deviations in optical constants of PVC.** Each standard deviation is determined from ten reference and ten sample signals. The dotted lines represent the raw curves obtained from Equation 8.3, whereas the solid lines are from an analytical function, $\exp(a_1x^6 + a_2x^5 + \ldots + a_6x + a_7)$, fitted to the dotted lines. The missing part of the curves in the high frequency range corresponds to the low SNR portion of the measured spectra.

with the thickness of 1 (1.006), 10 (9.809), 20 (19.943), 50 (50.040), 100 (100.697), and 200 (201.294) mm. THz-TDS measurements are made in the axial direction of the samples with ten scans for each sample. The interval between each scan is 45 sec.

### Optical constants

Figure 8.6 shows the optical properties of HDPE, extracted from the 50-mm sample. The phase at low frequencies is extrapolated from that between 0.05 and 1 THz. Obviously, the refractive index is constant at 1.512 over the frequency range, and the absorption coefficient is nearly zero. The estimated refractive index is slightly lower than previously published values at 1.53 (Jin *et al.* 2006, Piesiewicz *et al.* 2007), but the extinction coefficient is comparable to that in Piesiewicz *et al.* (2007).

### Optimum thickness

Further analysis shows that the optimum thickness of HDPE determined using Equation 8.11 is higher than 20 mm for the frequency below 2 THz, as shown in Figure 8.7. These sample thicknesses, although relatively thick, are expected to provide the lowest uncertainty in the measurement of the optical constants. It is evident that the prepared

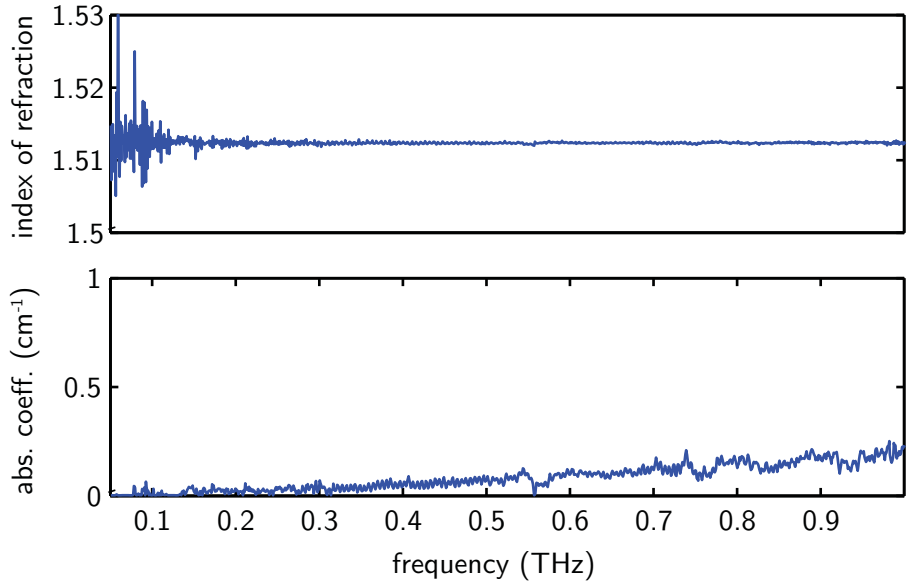


**Figure 8.6. Optical constants of HDPE.** The constants are calculated from the average signal probing the 50-mm-thick sample. The noise in the refractive index at low frequencies is due to the low SNR of the probing signal.

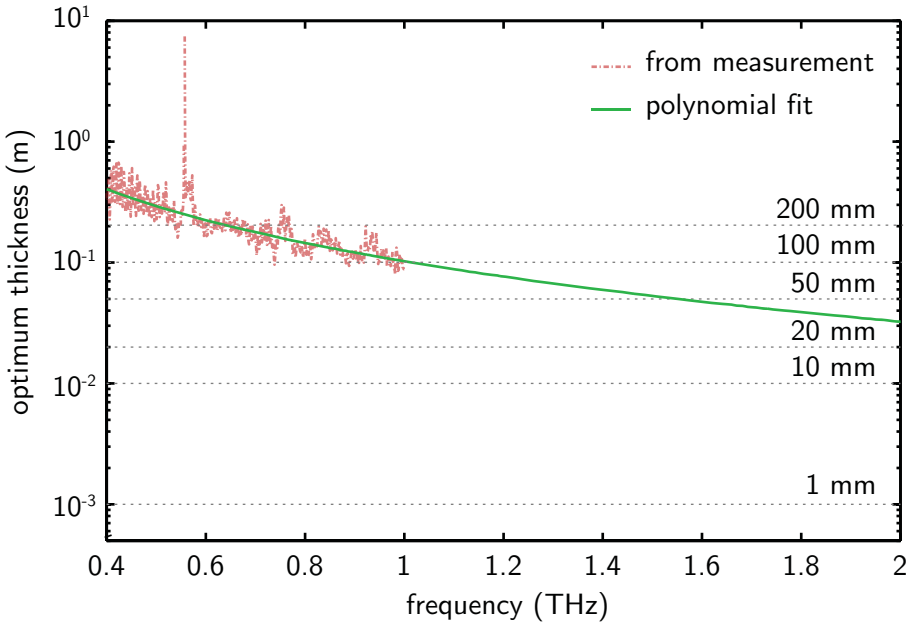


**Figure 8.7. Optimum thickness for HDPE.** The optimum thickness is determined from the measured absorption coefficient. The solid line is a second-order polynomial fit to the absorption coefficient between 0.05 and 1 THz. The horizontal dotted lines indicate the sample thicknesses of 1, 10, 20, 50, 100, and 200 mm, available for the measurements.

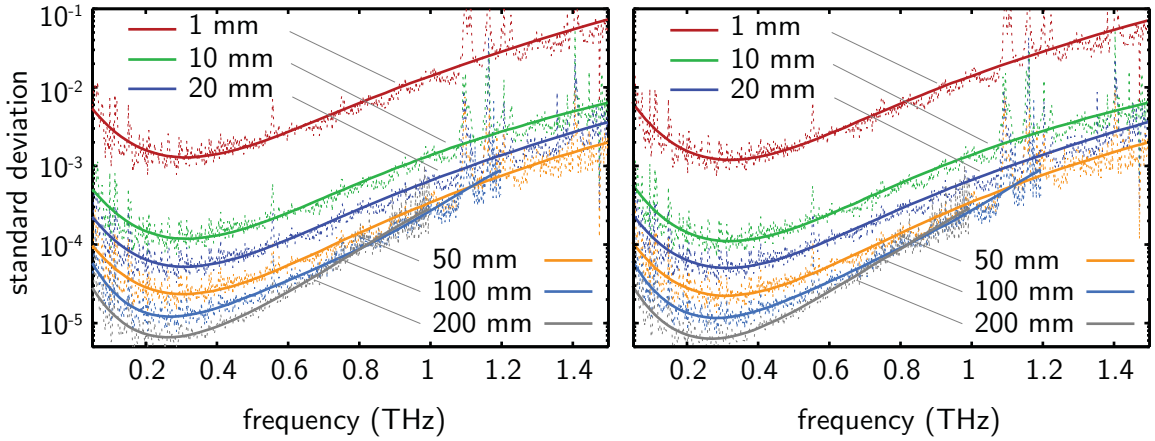


(a) standard deviation of $n$ (b) standard deviation of $\kappa$

**Figure 8.8. Standard deviations in optical constants of HDPE.** Each standard deviation is determined from ten reference and ten sample signals. The dotted lines represent the raw curves obtained from Equation 8.3, whereas the solid lines are from an analytical function, $\exp(a_1x^5 + a_2x^4 + \ldots + a_5x + a_6)$, fitted to the dotted lines. The missing part of the curves in the high frequency range corresponds to the low SNR portion of the measured spectra.

thicknesses of 1, 10, and 20 mm are suboptimal at all frequencies of interest, and, thus, measurement at these thicknesses is vulnerable to high uncertainty. Moreover, the sample thicknesses of 50, 100, and 200 mm are the best for measurement at 1.6, 1.0, and 0.6 THz, respectively.

### Standard deviation

Figure 8.8 confirms the predicted optimum thickness for HDPE. By measuring the samples at various thicknesses, the standard deviations of the measured optical constants can be compared. The sample thickness of 1 mm results in the highest standard deviation for the given samples, and increase of the thickness reduces the deviation proportionally. The 50 mm sample leads to the lowest standard deviation around 1.1 to 1.5 THz; the 100 mm sample, around 0.8 to 1.1 THz; and the 200 mm sample, below 0.8 THz. The results are in excellent agreement with the optimum thickness predicted earlier in Figure 8.7. In addition, between 0.05 and 1.0 THz, the standard deviation for the 200-mm-thick sample is better than that for the 1-mm-thick sample by two orders of magnitude.

### 8.5.3 Ultra-high molecular weight polyethylene: UHMWPE

The PE pellets used in this experiment are prepared by pressing amounts of pure ultra-high molecular weight polyethylene (UHMWPE) powder in a pellet press at 10 tonnes. The surfaces of the resulting pellets are an optical grade, and thus the surface scattering is negligible. The available thicknesses of the pellets are as follows: 4.5 (4.542), 5.4 (5.414), 8 (8.066), 9 (9.142) mm. Note that the pellet press is limited to pellet thicknesses below 10 mm. Each of the PE pellets is measured with a focused T-ray beam for ten scans, with an interscan interval of 30 sec.

#### Optical constants

The optical constants of PE, extracted from the 9-mm sample, are shown in Figure 8.9. In the extraction process, the phase spectrum at low frequencies is extrapolated from the phase between 0.1 and 1 THz. The average index of refraction is 1.465, and the absorption coefficient is below 1 $cm^{-1}$ up to 2 THz. The measured absorption coefficient is in agreement with the value published in Fischer (2005), but a previously published value of refractive index for UHMWPE is not available.

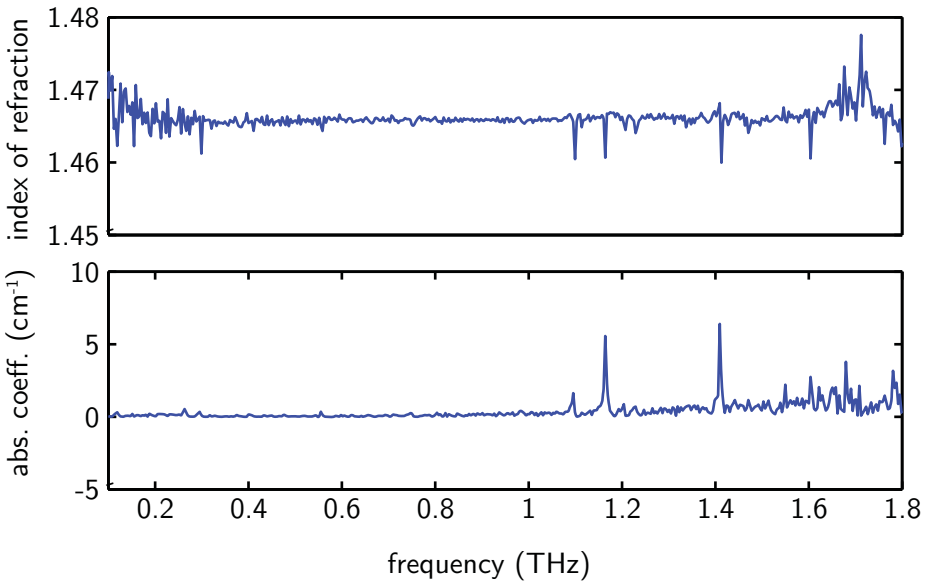


**Figure 8.9. Optical constants of UHMWPE.** The constants are calculated from the average signal probing the 9-mm-thick sample. The available bandwidth of the measurement is 0.05 to 1.8 THz. Water-vapour resonances are observed at 1.1, 1.17, and 1.4 THz in the refractive index and the absorption coefficient.

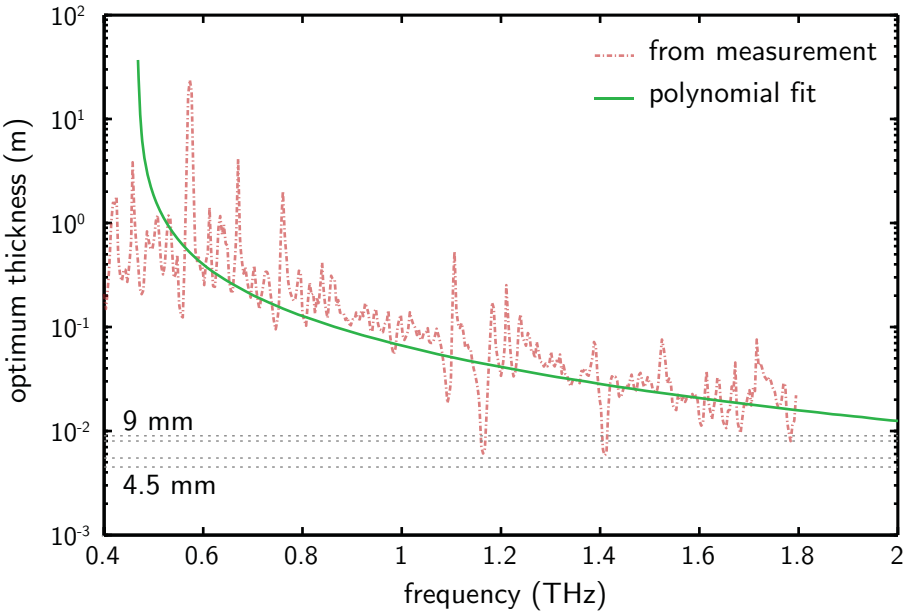


**Figure 8.10. Optimum thickness for UHMWPE.** The optimum thickness is determined from the measured absorption coefficient. The solid line is a second-order polynomial fit to the absorption coefficient between 0.4 and 1.8 THz. The horizontal dotted lines indicate the sample thicknesses of 4.5, 5.5, 8, and 9 mm, available for the measurements.

### Optimum thickness

The optimum thickness for PE is obtained by using Equation 8.11, as shown in Figure 8.10. As UHMWPE is virtually non-absorptive at low frequencies, no optimum thickness below 0.4 THz is determinable. The exceptional transparency of PE causes a considerably large optimum thickness, i.e., higher than 10 mm below 2 THz. Thus, the thicknesses of the prepared pellets are suboptimal at all frequencies of interest.

### Standard deviation

The standard deviations of the optical constants of PE at different thicknesses are shown in Figure 8.11. At all frequencies of interest, the standard deviation decreases with increase of the sample thickness. This result concurs with the calculation of the optimum thickness, which shows the lowest standard deviation for a thicker sample.

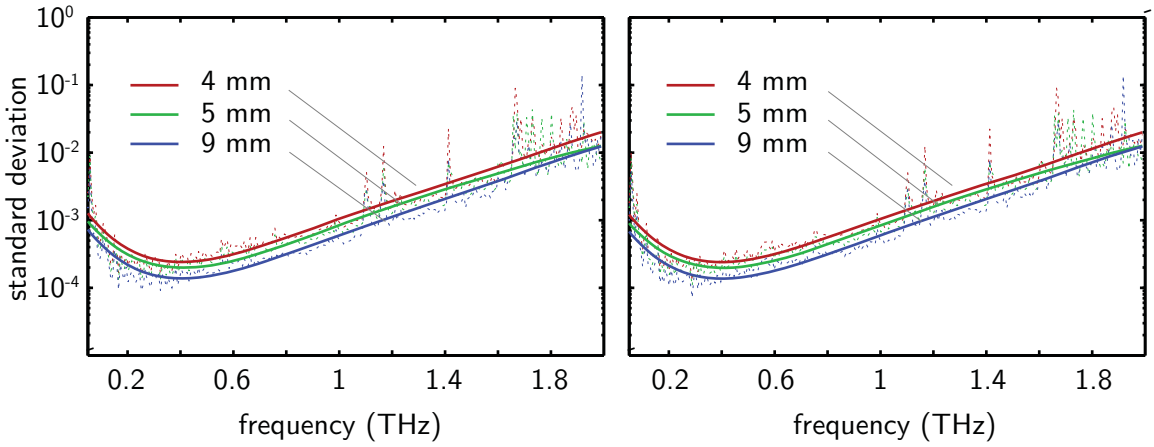


(a) standard deviation of $n$ (b) standard deviation of $\kappa$

**Figure 8.11. Standard deviations in optical constants of UHMWPE.** Each standard deviation is determined from ten reference and ten sample signals. The dotted lines represent the raw curves obtained from Equation 8.3, whereas the solid lines are from an analytical function, $\exp(a_1x^5 + a_2x^4 + \ldots + a_5x + a_6)$, fitted to the dotted lines. The result for the 8-mm pellet is very close to that of 9-mm, and thus is not shown here.

### 8.5.4 Liquid water

The measurement for liquid water is different from that for solid dielectrics in terms of the propagation geometry. During measurement, water must be contained in a cell that is equipped with a pair of transparent windows. The presence of the windows modifies the transfer function describing the measurement. Theoretically, the proposed model of the optimum thickness is still valid in this case.

In the experiment, the cell in use is assembled from two parallel cycloolefine windows, each with the thickness of 3 mm, and a replaceable spacer in between. The spacer facilitates adjustment to the thickness of the liquid sample. Distilled water is injected into the cell, which is pre-adjusted to accommodate various thicknesses, from 15, 30, 40, 60 (61), 80, to 170 $\mu$m. The sample with each thickness is measured with a focused T-ray beam at the normal angle of incidence for ten scans, with a 45 sec interval between scans. The reference is measured with the identical cell, filled with dry air only.

#### Optical constants

The optical constants of water, shown in Figure 8.12, are obtainable from the 170-$\mu$m sample measurement, which provides the lowest disturbance due to Fabry-Pérot

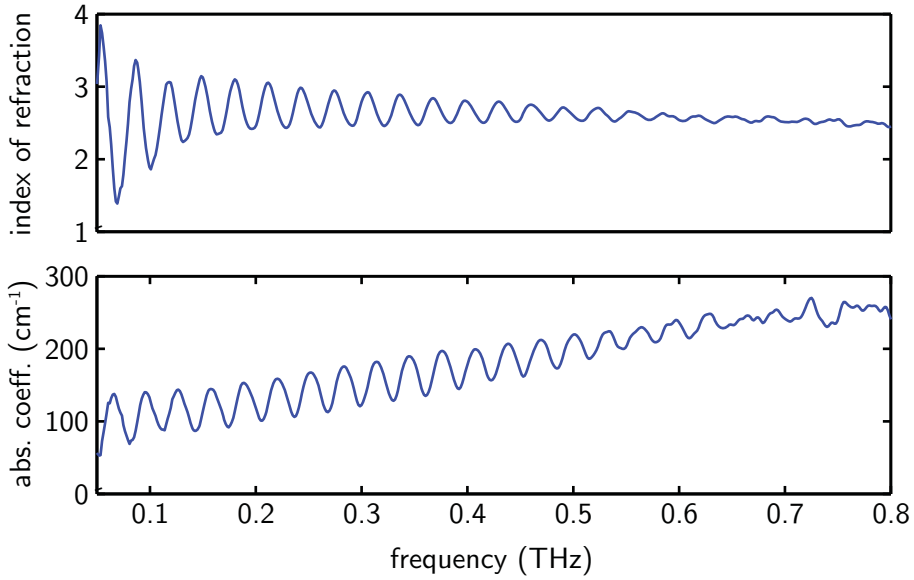


**Figure 8.12. Optical constants of water.** The constants are calculated from the average signal probing a 170-$\mu$m-thick sample. The available bandwidth of the measurement is 0.05 to 0.8 THz. The ripples are caused by Fabry-Pérot reflections within the windows.

fringes. The phase at low frequencies is extrapolated from the phase value between 0.05 and 0.5 THz. Although the sample spectrum is normalised by the reference measured with a blank cell, the reflections induced by the windows cannot be completely removed. The average refractive index is approximately 2.5, whereas the absorption coefficient rises linearly to 250 cm$^{-1}$ at 0.8 THz. These values are consistent with the optical constants of water at T-ray frequencies published in Afsar (1978) and Thrane *et al.* (1995).

### Optimum thickness

The exceptionally high absorption of water results in the requirement of a thin sample under measurement. Calculated from the absorption coefficient using Equation 8.11, the optimum thickness of water in the range between 0.05 to 2.0 THz is illustrated in Figure 8.13. It is clear that for this frequency range, the optimum thickness lies between 40 and 200 $\mu$m. Decreasing the thickness further than 40 $\mu$m would cause an increase in the variance at all frequencies.

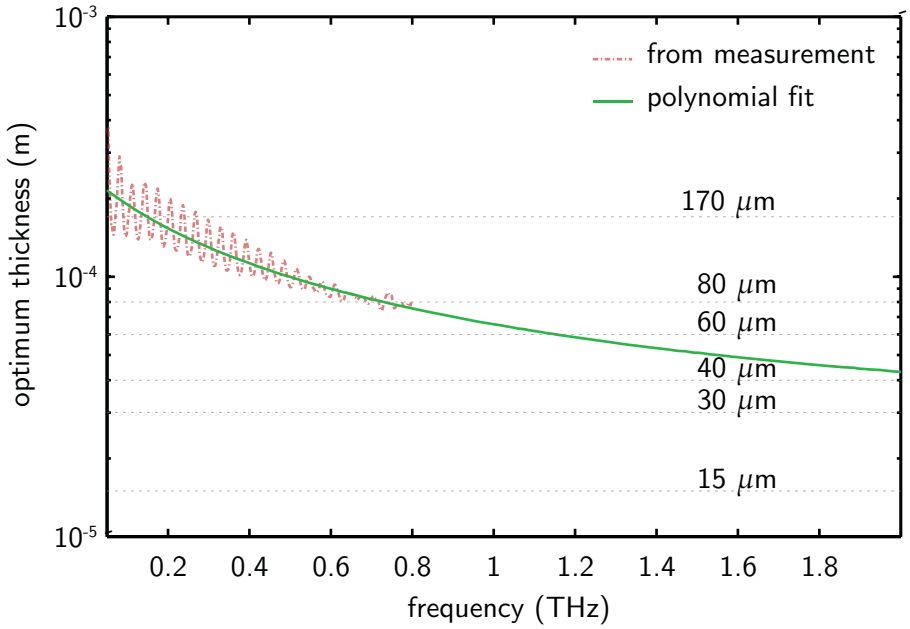


**Figure 8.13. Optimum thickness for water.** The optimum thickness is determined from the measured absorption coefficient. The solid line is a second-order polynomial fit to the absorption coefficient between 0.05 and 0.8 THz. The horizontal dotted lines indicate the sample thicknesses of 15, 30, 40, 60, 80, and 170 $\mu$m, available for the measurements.

### Standard deviation

Figure 8.14 depicts the standard deviations of the optical constants of water measured at different thicknesses. Notice that as the sample thickness decreases beneath 40 $\mu$m, the standard deviation increases proportionally at all frequencies of interest. At 1.7 to 2.0 THz, the 40-$\mu$m sample shows the lowest standard deviation; at 0.4-1.7 THz, the 60-$\mu$m and 80-$\mu$m samples; at 0.05-0.4 THz, the 170-$\mu$m sample. The results are agree well with the prediction for the optimum thickness in Figure 8.13. The improvement of the measurement precision can be clearly observed. By comparing the standard deviations of 15-$\mu$m and 170-$\mu$m samples at 0.2 THz, it is seen that the difference in precision is nearly one order of magnitude.

This experiment explicitly shows the impracticality of an excessively thin sample. Also it shows the functionality of the optimum thickness equation, although the transfer function of a sample in cell is different from that of a free-standing sample.

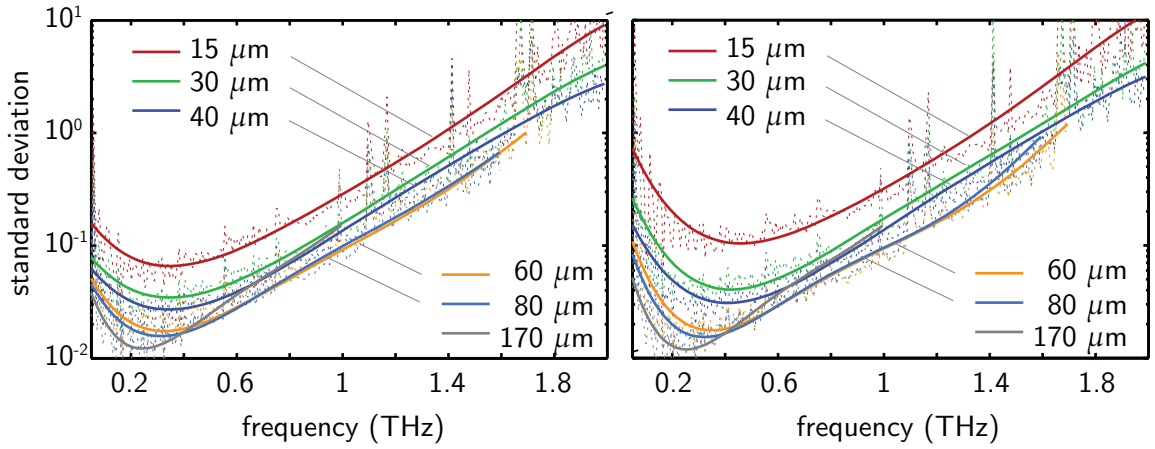


(a) standard deviation of $n$ (b) standard deviation of $\kappa$

**Figure 8.14. Standard deviations in optical constants of water.** Each standard deviation is determined from ten reference and ten sample signals. The dotted lines represent the raw curves obtained from Equation 8.3, whereas the solid lines are from an analytical function, $\exp(a_1x^5 + a_2x^4 + \ldots + a_5x + a_6)$, fitted to the dotted lines. The missing part of the curves at higher frequencies corresponds to the low SNR portion of the measured spectra.

### 8.5.5 Lactose

The sample materials used so far in Sections 8.5.1 to 8.5.4 have rather featureless spectra. In contrast, for a more general case, polycrystalline $\alpha$-lactose monohydrate is selected for this experiment, because it has a distinctive absorption spectrum due to intermolecular resonance modes at lower T-ray frequencies. The sample pellets of lactose with different thicknesses are prepared from lactose powder ground together with UHMWPE powder in the mass ratio of 1:3. The mixture powder is pressed at 10 tonnes by a hydraulic press to produce six pellets with the diameter of 13 mm and the thicknesses from 0.4 (0.440), 0.8 (0.876), 1.6 (1.658), 2.4 (2.385), 3.2 (3.196), to 4.0 (4.014) mm, all with optical-graded surfaces. The pellets are measured with a focused T-ray beam. Eight scans are recorded for each pellet, and another eight for the reference. For this experiment, the ambient measurement atmosphere is purged with nitrogen to reduce the effects of water vapour absorption. It is worth noting that the measured results are not for pure $\alpha$-lactose monohydrate, but rather a $\alpha$-lactose monohydrate/UHMWPE mixture. However, for conciseness, this mixture is referred to as the *lactose mix* hereafter.

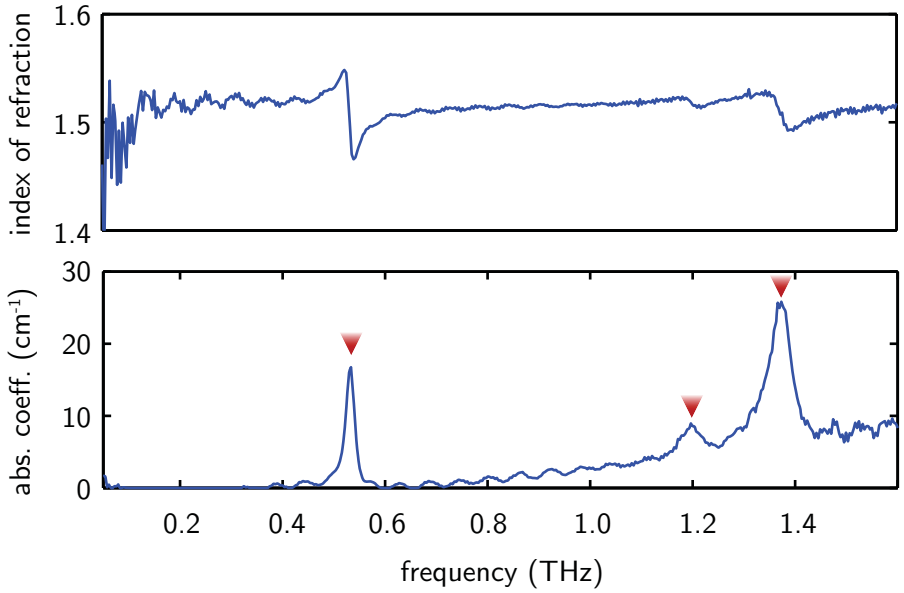


**Figure 8.15. Optical constants of lactose mix.** The constants are calculated from the average signal probing the 1.6-mm sample. The absorption peaks are pronounced at 0.53, 1.2, and 1.37 THz, as indicated by the arrowheads, before the spectrum is overwhelmed by noise beyond 1.6 THz.

### Optical constants

The optical constants for the lactose mix, shown in Figure 8.15, are determined from the 1.6-mm sample. The phase data at the frequencies lower than 0.05 THz are extrapolated from the data from 0.05 to 1.0 THz. Below 1.6 THz, the average value of the refractive index is 1.513, and the absorption coefficient is less than 30 $cm^{-1}$. The strong absorption peaks, clearly observable at 0.53, 1.2, and 1.37 THz, reproduce the results published in Fischer *et al.* (2005b).

### Optimum thickness

The optimum thickness for the lactose mix, plotted in Figure 8.16, is determined from the measured absorption coefficient using the developed equation. For those frequencies below 1.2 THz, which contain no absorption peak, the optimum thickness is higher than 4.0 mm. The available thicknesses of the sample are likely to provide the lowest measurement uncertainty of the optical constants around the vicinities of absorption peaks. More specifically, the 1.6-mm sample should give the lowest uncertainty for the absorption peak at 0.53 THz, and the 0.8-mm sample gives the lowest uncertainty for the peak at 1.37 THz.

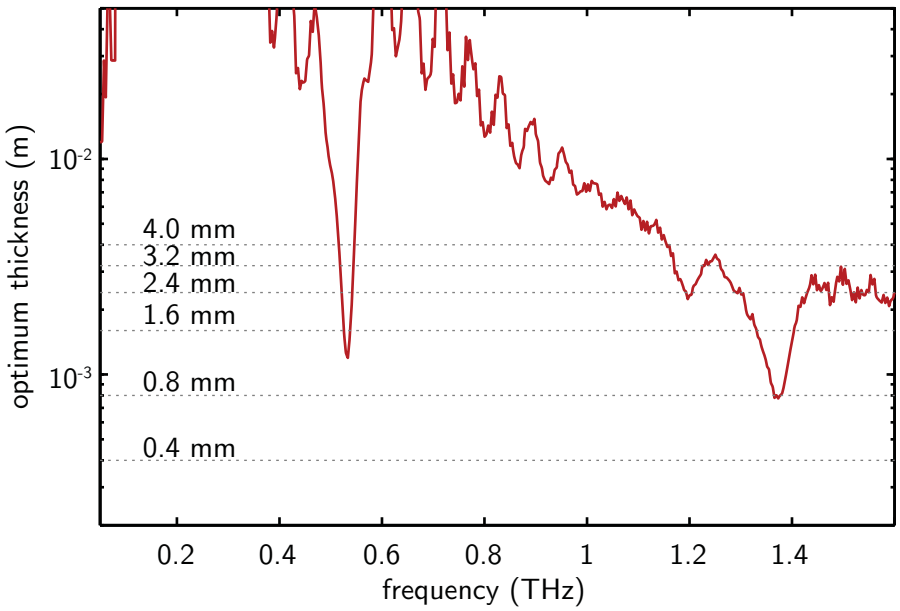


**Figure 8.16. Optimum thickness for lactose mix.** The optimum thickness is determined from the measured absorption coefficient. The horizontal dotted lines indicate the sample thicknesses of 0.4, 0.8, 1.6, 2.4, 3.2, to 4.0 mm, available for the measurements.

### Standard deviation

To confirm the prediction of the optimum thickness, the standard deviation in the optical constants is determined, via the Monte Carlo method, from the repeated measurements. As shown in Figure 8.17, the values of the standard deviation at each interesting frequency are plotted against the thickness for clarity. Two frequencies at 0.53 and 1.37 THz are the locations of the absorption peaks of lactose, whilst another two frequencies at 0.4 and 1.0 THz are the locations of the baseline away from the peaks. It is clear from Figure 8.17 that at 0.53 and 1.37 THz, the sample thicknesses of 1.6 and 0.8 mm provide the lowest standard deviation in measurement, respectively. At the frequencies of baseline, i.e., 0.4 and 1.0 THz, no optimum thickness is found in the thickness range between 0.4 and 4 mm, and the standard deviation profiles become lower towards a thicker sample thickness. The results in Figure 8.17 hence justify the prediction of the optimum thickness in Figure 8.16.

## 8.6 Usage of the model

The proposed model for optimum thickness is frequency-dependent, and thus it can determine the thickness for materials with any type of absorption response, provided

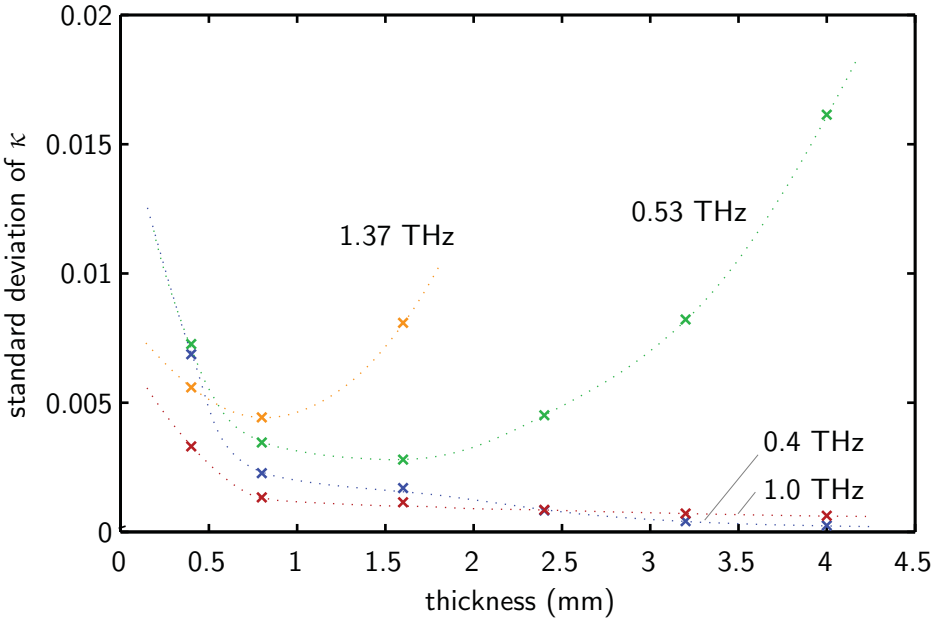


**Figure 8.17. Standard deviation in extinction coefficient of lactose mix.** The values at each thickness, indicated by the crosses, are determined from eight reference and eight sample signals, using the Monte Carlo method. The frequencies 0.53 and 1.37 THz correspond to the two first significant absorption peaks of the lactose spectrum. The missing part of the 1.37-THz plot is due to the low SNR portion of the measured spectra. The standard deviation in the index of refraction has a comparable value, and hence is not shown here. The dotted lines are fitted to the measurements only for visualisation.

that the absorption coefficient is available. In practice, this absorption coefficient can be measured from a preliminary sample or obtained from a published value.

When selecting the optimum thickness, two options are available: (i) to have the widest measurement bandwidth, or (ii) to have the lowest uncertainty at a particular frequency. If the widest bandwidth is required, the maximum absorption value within the reliable frequency range of the system should be used in determination of the optimum thickness. This results in a thinner sample thickness thus retaining the bandwidth of the system and avoids dynamic range limited distortion, while providing a reasonably low uncertainty in the measurement. There is a possibility that one might need to observe a sample's response in a narrow frequency range, with the highest precision available from the instrument, for example, in order to resolve a weak absorption peak hidden beneath the noise or to quantify the ratio of a mixture. In such cases, the optimum thickness calculated at the frequency of interest is indeed the best selection.

Despite the thickness optimality, there are some unrestricted lower and upper limits of the thickness that are worth consideration. For a very thin sample, non-uniformities in the sample geometry and in the bulk material tend to be pronounced. Relocation of the sample during measurements may cause a large variation among measured signals (Markelz 2008). Although the variance in the signal's amplitude encompasses these effects, the dependence of the effects on the thickness is not taken into account in the optimisation. In addition, thickness measurement for a thin sample is prone to imprecision. Due to these concerns, special care must be given to the uniformity of a sample with very thin optimum thickness and to the method of thickness measurement. A concern for reflection removal may arise in the case of optimally thin samples, for which the succeeding reflections temporally overlap and inseparable. However, an iterative parameter extraction process can cope with those overlapping reflections (Duvillaret *et al.* 1996, Duvillaret *et al.* 1999). For a very thick sample, beam defocusing may cause an overestimation of the measured absorption coefficient. A collimated beam or long-focal length beam system can alleviate the effect.

## 8.7 Conclusion and potential extensions

Currently, for a transmission THz-TDS measurement, there is no explicit criterion for determining an appropriate thickness for a sample under measurement in the existing literature. Traditionally, the selection of the sample thickness depends wholly on the experience of an experimentalist. In many cases, the sample thickness is preferably thin, to preserve the bandwidth of the signal. This is favourable so long as the uncertainty in optical constants is properly considered. An excessively thin sample can cause significant rise in the uncertainty of the optical constants that is influenced by measurement noise.

This work offers a criterion in selecting the optimum thickness of a sample. Provided that the absorption of a sample material at a frequency of interest can be estimated or approximated, the proposed model can predict the optimum thickness, which gives the lowest uncertainty in measurement. The derivation of the criterion is carried out via minimising the uncertainty in optical constants—in terms of the variance or standard deviation—which is affected by the variance in measured time-resolved signals.

The experiments, performed with PVC, PE (high density and UHMW), and water, representing typical, low, and high absorption materials, confirm the validity and applicability of the derived thickness criterion. By selecting an optimum thickness for a sample under measurement, significant improvement in the standard deviation of the optical constants can be observed. These examples with monotonically increasing absorption sufficiently support the model, because the model determines the optimal thickness based on the absorption value at a particular frequency, regardless of the morphology of the absorption spectrum. In addition, as a case study, another experiment is performed with polycrystalline lactose, containing strong THz modes. An excellent agreement between the theory and the experimental results is achievable. Validated by the experiments, the proposed model can be used as a rule of thumb in selecting the thickness for a sample to achieve the minimum uncertainty in measured optical constants.

Another point, in conclusion, is that our analysis may apply in principle to optical and other regimes. However, generally speaking, the T-ray experimentalist more readily has control over the thickness, whereas the optical experimentalist tends to have more control over signal power. This explains why the analysis herein becomes generally of greater interest in the T-ray domain.

This chapter concludes Part II of the thesis—system evaluation and optimisation. Part III—T-ray optics—starts with Chapter 9 that describes an implementation of antireflection coating operated in the T-ray regime.

Chapter 9

# Quarter-Wavelength Antireflection Coatings for T-rays

TRANSPARENT windows are common to THz-TDS systems. The general function of such windows is to contain a sample. Even though the windows are transparent to T-rays, the attenuation due to multiple reflections at window interfaces exists. There has been very little work carried out to-date on the reduction of reflection losses, owing to the recent emergence of T-ray technology. This chapter analyses the reduction of T-ray reflection loss by means of a quarter-wavelength antireflection coating. Because T-ray wavelengths are much longer than visible wavelengths, the antireflection layer for T-rays is much thicker than the usual optical case. This motivates exploration of suitable coating materials and methods, different from those used for optical coatings, and the greater thickness also suggests the feasibility of retrofittable coatings.

## 9.1 Introduction

Typically, when the electromagnetic field propagates through a slab of material, it experiences two modes of amplitude attenuation—one is the *absorption loss* and the other is the *reflection loss*. The absorption loss is due to bulk material, inside which molecules absorb and convert the electromagnetic energy into vibrational motion or heat. This type of loss has an exponential dependence on the extinction coefficient of material and the propagation length. It is possible to control, i.e., decrease or increase, the absorption loss to some extent through temperature manipulation, since the extinction coefficient is temperature-dependent.

Another cause of amplitude attenuation is reflection loss. In this case, the wave energy is not converted into other energy forms, but rather diverted to another direction. When the field encounters an interface between two dielectrics, part of the field is reflected off a surface. The reflection direction and the reflection amplitude are predicted by Snell's law and Fresnel's law, respectively. The important parameter in both laws is the refractive index of material. In case of a normal angle of incidence at an air-sample interface, the reflection coefficient is given by $\rho = (n-1)/(n+1)$ and thus the reflectance is $\mathcal{R} = (n-1)^2/(n+1)^2$, where $n$ is the index of refraction of the sample. As $n$ increases from unity to infinity, the reflectance increases from zero to unity. The reflectance of some materials, typically used for T-ray windows, is illustrated in Figure 9.1.

It would appear that amplitude attenuation due to the reflection loss becomes dominant for transparent materials. This leads to the requirement for reducing such loss, in particular when a transparent material functions as, for example, a window or substrate. Through an antireflection coating on a window surface, the propagation direction can be controlled in such a way that it reduces the reflectance and enhances the transmittance. The underlying mechanism of an antireflection coating is the interference formed by reflections inside the coating layer. A simple illustration showing the performance of the coating is given in Figure 9.2.

This chapter analyses the reduction of T-ray reflection loss by means of a quarter-wavelength antireflection coating. Because T-ray wavelengths are much larger than visible wavelengths, the antireflection layer for T-rays is much thicker than the usual optical case. This creates an interesting opportunity for retrofittable antireflection layers in T-ray systems. An example structure composed of a T-ray transparent window,

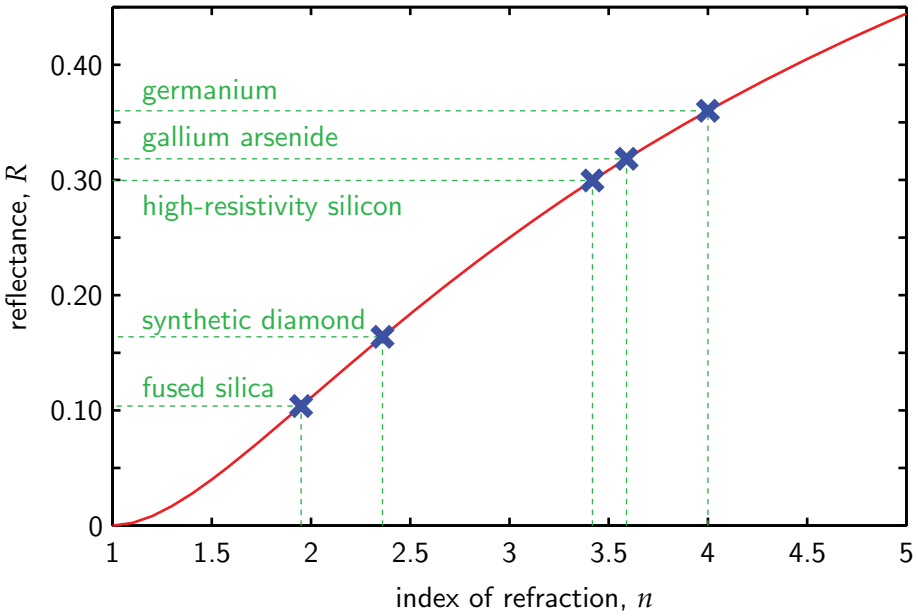


**Figure 9.1. Reflectance of common materials at T-ray regime.** The reflectance is calculated from $\mathcal{R} = (n-1)^2/(n+1)^2$ for some common materials used as window or substrate. The indices of refraction of these materials are for the T-ray radiation. The reflectance shown here takes into account only one surface. When two surfaces, i.e., the entry and exit faces of a slab, are considered, the reflectance increases to $2\mathcal{R} - \mathcal{R}^2$.

made from a high-resistivity silicon wafer, and a coating, made of common PE sheets is demonstrated. A coating material is applied onto the surfaces of a silicon window by means of supporting frame. This structure is characterised by a THz-TDS system, which has a reliable frequency range between 0.2 and 1.0 THz.

This chapter is organised as follows. Section 9.3 briefly reviews the existing work on antireflection coatings, which are effective at higher T-ray frequencies or the conventional FIR band. Based on the characteristic matrix analysis in Section 9.4, the theory of quarter-wavelength antireflection coatings is given in Section 9.5, leading to the models of reflectance and transmittance in Section 9.6. Section 9.7 explores some common T-ray transparent materials, which can be used as either windows or coatings depending on their optical and mechanical properties. Possible coating techniques for T-ray windows are summarised in Section 9.8. In Section 9.9 the retrofittable antireflection coating technique is presented along with the measured transmittances of the windows assembled by this technique.

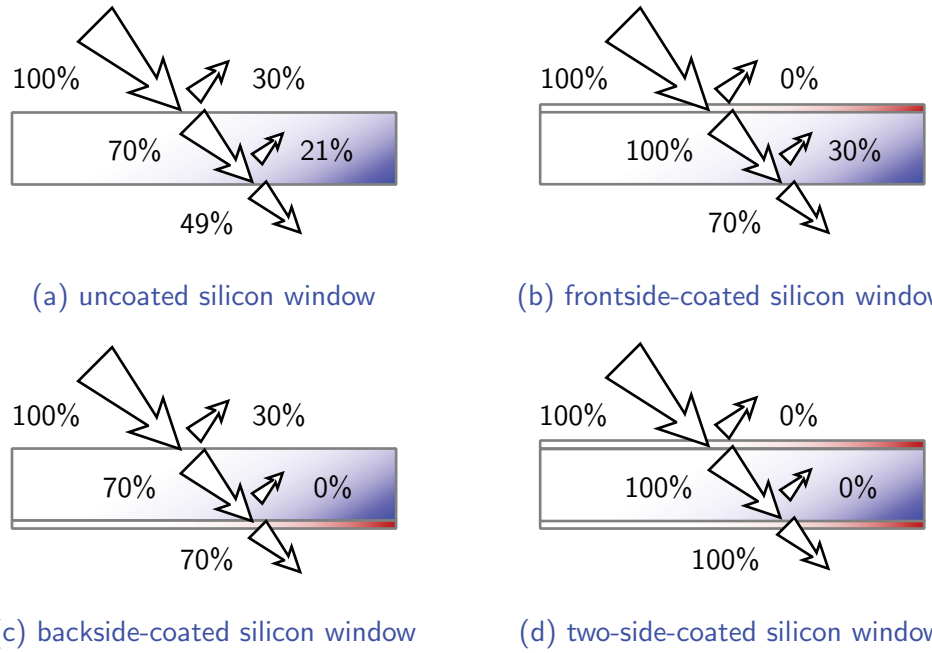


(a) uncoated silicon window

(b) frontside-coated silicon window

(c) backside-coated silicon window

(d) two-side-coated silicon window

**Figure 9.2. Antireflection coatings for silicon windows.** The indicated transmittance and reflectance percentages are for (i) a particular transmitting frequency, (ii) a normal angle of incidence, (iii) intrinsic silicon (no material absorption), and (iv) an appropriate thickness and index of refraction for the coating layers. The angle of incidence is exaggeratedly tilted for visualisation, and the arrows are not to scale.

## 9.2 Research objective and framework

### Objective

- To explore materials and coating techniques suitable for quarter-wavelength antireflection coating of T-ray transparent windows. The materials in use should be easily available, and the coating methods should be uncomplicated. Yet, the fabricated window should sustain the feasibility and reliability.
- To characterise the assembled antireflection windows in terms of its transmittance by means of THz-TDS. The enhancement of the window transmittance should follow the application of a suitable coating material. The measured transmittances are verified with the characteristic matrix method.

### Framework

The assumptions of the measurement carried out here are that: (i) an antireflection window under measurement has parallel and flat surfaces; (ii) the angle of incidence

of the T-ray beam is normal to the surface of the window; (iii) the incident beam is well collimated, i.e., no divergence or convergence at infinity; (iv) dry air surrounds the T-ray path; (v) the reference signal is measured under the same conditions as the sample signal, except for the absence of the sample; and (vi) the transverse dimension of the window and coating is large enough, so that no edge diffraction affects the result.

## 9.3 Review of antireflection coatings for T-rays

Some significant literature on antireflection windows operated with FTIR is covered below in chronological order. The important material parameters, including index of refraction, $n$, absorption coefficient, $\alpha$, and thickness, $l$, given in the literature are quoted to give clues on optical properties and structural dimensions. For comparison, all values taking the frequency related definitions, i.e., wavelength or wavenumber, are converted to the terahertz base units.

**Polyethylene coating/many substrates** (Armstrong and Low 1974). PE films ($n = 1.5$) were attached onto many substrate materials, i.e., synthetic sapphire, silicon, crystalline quartz, and calcium fluoride ($CaF_2$), by means of thermal bonds. The film thicknesses were in the order of ten microns. The spectroscopic data in the 1.5 THz to 15 THz range showed an increase in the transmittance for every substrate.

**Quartz/germanium** (Kawase and Hiromoto 1998). A plate of fused quartz ($n = 2.0$, $\alpha = 1\ \mathrm{cm}^{-1}$) was glued onto one side of an intrinsic germanium (Ge: $n = 4.0$) or gallium arsenide (GaAs: $n = 3.6$) substrate, and then the quartz was polished to a thickness of approximately 20 $\mu$m. Measured by FTIR spectroscopy, the coated germanium and gallium arsenide substrates exhibited 57-percent transmittance at 1.74 THz, and 65-percent transmittance at 1.43 THz, respectively. Later, Kawase *et al.* (2000) glued fused quartz onto two sides of the germanium substrate to confirm the reproducibility. This configuration raised the transmittance to 90 percent.

**Polyethylene/silicon** (Englert *et al.* 1999). Two LDPE sheets ($n = 1.52$, $\alpha = 66.8 \times 10^{-2}\mathrm{cm}^{-1}$, $l$=18.5 $\mu$m) were applied to both sides of a wedged silicon window in a vacuum, and the LDPE-coated window was heated up to promote durability. This structure attained up to 90-percent transmittance at 2.5 THz. The coated

window was used in aircraft, allowing highly-efficient narrowband remote sensing of the FIR radiation.

**Parylene/silicon** (Gatesman *et al.* 2000). Parylene-C ($n = 1.62$, $\alpha = 11$ cm$^{-1}$, $l = 24.0$ $\mu$m) or parylene-D ($n = 1.62$, $\alpha = 11$ cm$^{-1}$, $l = 26.5$ $\mu$m) was deposited onto both sides of each silicon substrate. The parylene-C and parylene-D coated substrates gave the transmittance of 90 percent at 1.9 THz and 1.7 THz, respectively. The authors noted that parylene coating thickness is not feasible below 1 THz.

**Parylene-C/silicon** (Hübers *et al.* 2001). A layer of parylene-C ($n = 1.62$, $\alpha = 27$ cm$^{-1}$, $l = 18.5$ $\mu$m) was deposited on a surface of a silicon window. An FTIR measurement showed 90% transmittance at 2.3 THz, and a significant enhancement from 1.5 to 3 THz. An application of the coating to a silicon lens, which was used in a hot-electron-bolometric (HEB) mixer, resulted in a success reduction in the noise temperature by an increment in the signal transmittance.

**Silicon dioxide/germanium** (Hosako 2003). A layer of silicon dioxide ($SiO_2$, $n = 2.10$, $l = 20.9$ $\mu$m) was deposited on a germanium substrate by the plasma-enhanced chemical vapour deposition (CVD) method. The transmittance of the substrate at 1.8 THz was increased to 55 %. Hosako (2004) and Hosako (2005) extended the previous work to a two-period coating structure, each period of which contains amorphous Si and $SiO_2$. The coated germanium has a transmittance of over 90% over a broad frequency band, centered at 1.8 THz.

Recently, a few papers reported studies on antireflection coatings with ultrafast T-ray systems. For example, Löffler *et al.* (2005) employed THz-TDS to characterise a silicon substrate coated with a mixture of paraffin wax and silicon powder on one side. The authors demonstrated only the amplitude spectrum of the sample, and the time-resolved signal was omitted. Furthermore, it was claimed that the index of refraction of the mixture is controllable by varying the mixture ratio, but there was no report on this index nor the coating thickness.

A paper reported by Biber *et al.* (2004) involves an *artificial* antireflection coating, operated with ultrafast T-ray systems. A silicon window was etched on both surfaces, forming grids of an artificial dielectric with a depth of quarter wavelength. Inspected by THz-TDS, this structure provided a relatively broadband high transmittance over 430-670 GHz. In addition, Brückner *et al.* (2007) proposed another artificial coating

technique. A surface-relief grating or moth-eye structure was crafted on the surfaces of a Topas window. Measured by a THz-TDS system, an enhancement in the transmittance at 0.2 and 0.9 THz was attainable. However, the principles underlying these techniques are beyond the scope of this work that focuses on homogeneous antireflection coatings.

It appears that almost all previous research addressed the designs and analyses of antireflection windows in the FIR region, i.e., from 1.5 THz to tens of terahertz. However, these designs are inappropriate for modern ultrafast T-ray systems, which operate in the frequency range between 0.1 and 2.0 THz or higher. In addition, most prior measurements were carried out via conventional FTIR spectroscopy, which delivers only transmittance magnitude spectra. The capability of ultrafast T-ray systems has not been fully exploited for characterising T-ray antireflection windows in the lower T-ray regime.

## 9.4 Characteristic matrix method

The complexity of a calculation model based on ray tracing rises dramatically in the case that a wave propagation through a structure with more than two parallel dielectric interfaces is simulated. This is because the number of possible propagation paths increases from inter-layer reflections. For instance, if only waves reflected at most four times are taken into calculation, a dielectric slab (two interfaces) allows three transmitting paths to occur. The number of transmitting paths rises to nine in a structure with three parallel interfaces, and so on. It appears that the calculation complexity can be alleviated by using the characteristic matrix method, where a composition of dielectric layers is explained by an ordinary matrix multiplication. A derivation of the characteristic matrix shown afterward is based on Hecht (1987).

Figure 9.3 shows an EM wave propagation across two dielectric interfaces. From the figure, the total electric field at interface I, $E_{\mathrm{I}}$, equals the summation of the incident field, $E_{i\mathrm{I}}$, and the reflected field, $E_{r\mathrm{I}}$. Since the electric and magnetic fields are continuous at an interface, the total electric field at interface I can also be expressed as the

summation of the refracted field, $E_{t\mathrm{I}}$, and the reflected field from interface II, $E'_{r\mathrm{II}}$. Thus,

$$\begin{aligned} E_{\mathrm{I}} &= E_{i\mathrm{I}} + E_{r\mathrm{I}} \\ &= E_{t\mathrm{I}} + E'_{r\mathrm{II}} \,. \end{aligned} \tag{9.1}$$

The total magnetic field at interface I is derivable from the electric field via

$$\begin{aligned} H_{\mathrm{I}} &= (E_{i\mathrm{I}} - E_{r\mathrm{I}})\mathrm{Y}_0 \\ &= (E_{t\mathrm{I}} - E'_{r\mathrm{II}})\mathrm{Y}_1 \,, \end{aligned} \tag{9.2}$$

where

$$\mathrm{Y}_0 = \sqrt{\frac{\epsilon_0}{\mu_0}} n_0 \cos\theta_0 \,, \tag{9.3a}$$

$$\mathrm{Y}_1 = \sqrt{\frac{\epsilon_0}{\mu_0}} n_1 \cos\theta_1 \,. \tag{9.3b}$$



**Figure 9.3. Electric and magnetic fields across two dielectric interfaces.** Three dielectric slabs with the refractive indices, $n_0$, $n_1$, and $n_s$, constitute two interfaces, across which the fields are continuous. Dielectric slabs 0 and $s$ are assumed to be semi-infinite. At interface I the angles of incidence and refraction are $\theta_0$ and $\theta_1$ to the normal, respectively. At interface II the angles of incidence and refraction are $\theta_1$ and $\theta_s$ to the normal, respectively. The propagation directions are denoted by the red dotted arrows, and the polarisation directions are denoted by the green solid arrows. In this case the electric field is $\sigma$-polarised (TE wave). Adapted from Hecht (1987).

Assuming that dielectric $s$ in Figure 9.3 is semi-infinite so that there is no reflection from the back surface of the medium, the total electric field at interface II is

$$\begin{aligned} E_{\mathrm{II}} &= E_{i\mathrm{II}} + E_{r\mathrm{II}} \\ &= E_{t\mathrm{II}} \,, \end{aligned} \tag{9.4}$$

and the total magnetic field at interface II is

$$\begin{aligned} H_{\mathrm{II}} &= (E_{i\mathrm{II}} - E_{r\mathrm{II}})\mathrm{Y}_1 \\ &= E_{t\mathrm{II}}\mathrm{Y}_s \,, \end{aligned} \tag{9.5}$$

where

$$\mathrm{Y}_s = \sqrt{\frac{\epsilon_0}{\mu_0}} n_s \cos\theta_s \,. \tag{9.6}$$

The relations between the fields within dielectric 1 are established through the propagation coefficient, or

$$E_{i\mathrm{II}} = E_{t\mathrm{I}} \cdot \exp(-i\gamma_1) \,, \tag{9.7a}$$

$$E_{r\mathrm{II}} = E'_{r\mathrm{II}} \cdot \exp(+i\gamma_1) \,, \tag{9.7b}$$

where $\gamma_1 = \omega n_1 l \cos\theta_1 / c$. By substituting Equations 9.7a and 9.7b into Equations 9.4 and 9.5, the total electric and magnetic fields at interface II are rewritten as

$$E_{\mathrm{II}} = E_{t\mathrm{I}} \cdot \exp(-i\gamma_1) + E'_{r\mathrm{II}} \cdot \exp(+i\gamma_1) \,, \tag{9.8}$$

and

$$H_{\mathrm{II}} = \left[E_{t\mathrm{I}} \cdot \exp(-i\gamma_1) - E'_{r\mathrm{II}} \cdot \exp(+i\gamma_1)\right] \mathrm{Y}_1 \,. \tag{9.9}$$

From Equations 9.1, 9.2, 9.8, and 9.9, the total fields at interface I can be related to the total fields at interface II as

$$E_{\mathrm{I}} = E_{\mathrm{II}} \cos\gamma_1 + H_{\mathrm{II}} \frac{i}{\mathrm{Y}_1} \sin\gamma_1 \,, \tag{9.10}$$

and

$$H_{\mathrm{I}} = E_{\mathrm{II}} \mathrm{Y}_1 i \sin\gamma_1 + H_{\mathrm{II}} \cos\gamma_1 \,. \tag{9.11}$$

Equations 9.10 and 9.11 can be described in a matrix form as

$$\begin{bmatrix} E_{\mathrm{I}} \\ H_{\mathrm{I}} \end{bmatrix} = \mathbf{M}_1 \begin{bmatrix} E_{\mathrm{II}} \\ H_{\mathrm{II}} \end{bmatrix} \,. \tag{9.12}$$

The matrix $\mathbf{M}_1$ is known as the *characteristic matrix*. For dielectric 1 the characteristic matrix is defined as

$$\mathbf{M}_1 = \begin{bmatrix} m_{11} & m_{12} \\ m_{21} & m_{22} \end{bmatrix} = \begin{bmatrix} \cos\gamma_1 & (i\sin\gamma_1)/\mathrm{Y}_1 \\ \mathrm{Y}_1 i\sin\gamma_1 & \cos\gamma_1 \end{bmatrix} . \tag{9.13}$$

For a system of cascading $N$ dielectric slabs, the total characteristic matrix is also available, as

$$\mathbf{M}_{\text{total}} = \mathbf{M}_1\mathbf{M}_2\mathbf{M}_3\cdots\mathbf{M}_N , \tag{9.14}$$

where each numerical subscript denotes each dielectric layer, and the subscript '1' denotes the top layer.

### Transmission and reflection functions

In order to find the transmission and reflection functions of a slab or a system of slabs, the total fields in Equation 9.12 are expanded to the incident, reflected, and transmitted electric fields as

$$\begin{bmatrix} E_{i\mathrm{I}} + E_{r\mathrm{I}} \\ (E_{i\mathrm{I}} - E_{r\mathrm{I}})\mathrm{Y}_0 \end{bmatrix} = \mathbf{M}_1 \begin{bmatrix} E_{t\mathrm{II}} \\ E_{t\mathrm{II}}\mathrm{Y}_s \end{bmatrix} . \tag{9.15}$$

Expanding the matrix gives

$$E_{i\mathrm{I}} + E_{r\mathrm{I}} = m_{11}E_{t\mathrm{II}} + m_{12}E_{t\mathrm{II}}\mathrm{Y}_s \tag{9.16a}$$

$$(E_{i\mathrm{I}} - E_{r\mathrm{I}})\mathrm{Y}_0 = m_{21}E_{t\mathrm{II}} + m_{22}E_{t\mathrm{II}}\mathrm{Y}_s . \tag{9.16b}$$

Solving for the transmission function $T(\omega) = E_{t\mathrm{II}}/E_{i\mathrm{I}}$ and the reflection functions $R(\omega) = E_{r\mathrm{I}}/E_{i\mathrm{I}}$ gives

$$T(\omega) = \frac{2\mathrm{Y}_0}{\mathrm{Y}_0 m_{11} + \mathrm{Y}_0\mathrm{Y}_s m_{12} + m_{21} + \mathrm{Y}_s m_{22}} , \tag{9.17}$$

and

$$R(\omega) = \frac{\mathrm{Y}_0 m_{11} + \mathrm{Y}_0\mathrm{Y}_s m_{12} - m_{21} - \mathrm{Y}_s m_{22}}{\mathrm{Y}_0 m_{11} + \mathrm{Y}_0\mathrm{Y}_s m_{12} + m_{21} + \mathrm{Y}_s m_{22}} . \tag{9.18}$$

The above derivation is for the electric field polarised perpendicular to the plane of incidence (TE wave), where

$$\mathrm{Y}_0 = \sqrt{\frac{\epsilon_0}{\mu_0}} n_0 \cos\theta_0 , \qquad \mathrm{Y}_1 = \sqrt{\frac{\epsilon_0}{\mu_0}} n_1 \cos\theta_1 , \qquad \mathrm{Y}_s = \sqrt{\frac{\epsilon_0}{\mu_0}} n_s \cos\theta_s . \tag{9.19}$$

It is also valid for the electric field polarised in the plane of incidence (TM wave), provided that

$$\mathrm{Y}_0 = \sqrt{\frac{\epsilon_0}{\mu_0}} n_0 / \cos\theta_0 \,, \qquad \mathrm{Y}_1 = \sqrt{\frac{\epsilon_0}{\mu_0}} n_1 / \cos\theta_1 \,, \qquad \mathrm{Y}_s = \sqrt{\frac{\epsilon_0}{\mu_0}} n_s / \cos\theta_s \,. \tag{9.20}$$

It is worth noting that other expressions for the transmission and reflection functions are available. These expressions include a recursive function for arbitrary dielectric slabs (Orfanidis 2006), an approximate characteristic matrix for arbitrary dielectric slabs (Born and Wolf 1999), a recursive function (Chebyshev polynomials) for periodic slabs (Born and Wolf 1999), and a non-recursive function for periodic slabs (Mojahedi *et al.* 2000). However, the subsequent calculations are based on the characteristic matrix method.

## 9.5 Quarter-wavelength antireflection coatings

Figure 9.4 shows the case of a window with an antireflection layer on one side, where $l_a$ is the coating thickness, and $n_0$, $n_a$, and $n_s$ are the refractive indices of air, coating material, and substrate, respectively. The window is assumed to be semi-infinite so that there is no reflection from the back surface. Through the characteristic matrix method, the optimum coating parameters, $l_a$ and $n_a$, required for a zero reflectance at a particular frequency will be derived in this section.

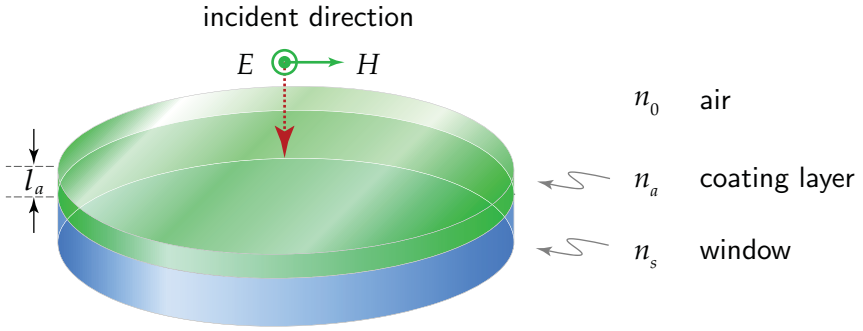


**Figure 9.4. Antireflection-coated window.** The single coating layer has the index of refraction of $n_a$ and the thickness of $l_a$. The transmittivity and reflectivity considered in this section is for the case that the field direction is normal to the surface of a semi-infinite window.

When the field direction is normal to the coated surface, from Equations 9.17 and 9.18 the transmission and reflection functions of the coating layer, independent of the polarisation, are simplified to

$$T(\omega) = \frac{2n_a n_0}{n_a(n_0+n_s)\cos(\omega n_a l_a/c) + i(n_0 n_s + n_a^2)\sin(\omega n_a l_a/c)}, \quad (9.21)$$

and

$$R(\omega) = \frac{n_a(n_0-n_s)\cos(\omega n_a l_a/c) + i(n_0 n_s - n_a^2)\sin(\omega n_a l_a/c)}{n_a(n_0+n_s)\cos(\omega n_a l_a/c) + i(n_0 n_s + n_a^2)\sin(\omega n_a l_a/c)}, \quad (9.22)$$

respectively.

Hence, the reflectance of the coating layer equals

$$\mathcal{R} = |R(\omega)|^2 = \frac{n_a^2(n_0-n_s)^2\cos^2(\omega n_a l_a/c) + (n_0 n_s - n_a^2)^2\sin^2(\omega n_a l_a/c)}{n_a^2(n_0+n_s)^2\cos^2(\omega n_a l_a/c) + (n_0 n_s + n_a^2)^2\sin^2(\omega n_a l_a/c)}, \quad (9.23)$$

and according to the law of energy conservation (assuming no absorption in the coating material), the transmittance is

$$\mathcal{T} = 1 - \mathcal{R} = \frac{4n_0 n_s n_a^2}{n_a^2(n_0+n_s)^2\cos^2(\omega n_a l_a/c) + (n_0 n_s + n_a^2)^2\sin^2(\omega n_a l_a/c)}. \quad (9.24)$$

At $\omega n_a l_a/c = a\pi, a \in \{0,1,2,\ldots\}$, the transmittance becomes minimum and the reflectance becomes maximum, or

$$\mathcal{T}_{\min} = \frac{4n_0 n_s}{(n_0+n_s)^2}, \quad (9.25a)$$

$$\mathcal{R}_{\max} = \frac{(n_0-n_s)^2}{(n_0+n_s)^2}. \quad (9.25b)$$

These expressions equal the transmittance and reflectance at an air-substrate interface without a coating (Fresnel's law).

On the other hand, the reversal of the extrema occurs at $\omega n_a l_a/c = (2a+1)\pi/2$, $a \in \{0,1,2,\ldots\}$, or

$$\mathcal{T}_{\max} = \frac{4n_0 n_s n_a^2}{(n_0 n_s + n_a^2)^2}, \quad (9.26a)$$

$$\mathcal{R}_{\min} = \frac{(n_0 n_s - n_a^2)^2}{(n_0 n_s + n_a^2)^2}. \quad (9.26b)$$

From Equation 9.26, provided that

$$n_a^2 = n_0 n_s, \quad (9.27)$$

the transmittance is unity and the reflectance is zero. In the case that the field is incident in free space, where $n_0 = 1$, the optimal refractive index of the coating is given by

$$n_a = \sqrt{n_s} \,. \tag{9.28}$$

This coating gives a zero reflectance at the frequency

$$f_c = \frac{c}{4 n_a l_a} \,, \tag{9.29}$$

and its odd harmonics. Usually, the optimal frequency $f_c$ is pre-determined, and the coating thickness $l_a$ is selected according to Equation 9.29.

In a real situation Equation 9.28 cannot be satisfied due to the limited number of appropriate coating materials. Thus, a material with the closest index value is often adopted. With such an unmatched index value, the transmission enhancement is still attainable at $f_c$ and its odd harmonics, but in this case the transmittance does not reach unity.

It should be noted that Equation 9.29 can be rewritten in terms of optical thickness as

$$n_a l_a = \frac{c}{4 f_c} = \frac{\lambda_c}{4} \,. \tag{9.30}$$

The optical thickness of the coating layer is a quarter of the optimal wavelength. Thus this kind of antireflection coating is so-called *quarter-wavelength antireflection coating*.

The effect of quarter-wavelength antireflection coating can be visualised as follows. When the electromagnetic wave travelling in a low index layer is reflected off by a higher index layer, its phase is shifted by 180°, or a half wavelength. In the case of an antireflection window, where $n_0 < n_a < n_s$, the wave reflected at either air-coating or coating-window interface therefore experiences a half-wavelength phase shift. Furthermore, the wave traversing a quarter-wavelength coating layer back and forth will have an additional phase shift of a half wavelength. The phase shift due to bulk propagation and the phase shift due to coating-window reflection are summed up to give a full wavelength phase shift. The wave reflected from the air-coating interface with a half wavelength phase shift will then destructively interfere with the wave reflected from the coating-window interface with a full wavelength phase shift. The destructive interference hence nullifies the total reflected wave.

## 9.6 Reflectance and transmittance models

### 9.6.1 Reflectance of quarter-wavelength coated surface

The coating layer influences the field propagation from lower to higher index material and vice versa in a similar way. This can be demonstrated via the reflectance models for a silicon interface in Figures 9.5 and 9.6, for which the propagation direction is from air to a silicon window and from a silicon window to air, respectively. These reflectances are calculated using the squared modulus of Equation 9.18, and only the effect at the air/silicon or silicon/air interface is taken into account without considering reflections inside the silicon window. The coating material has an exact index value of $\sqrt{n_{\text{si}}}$, and

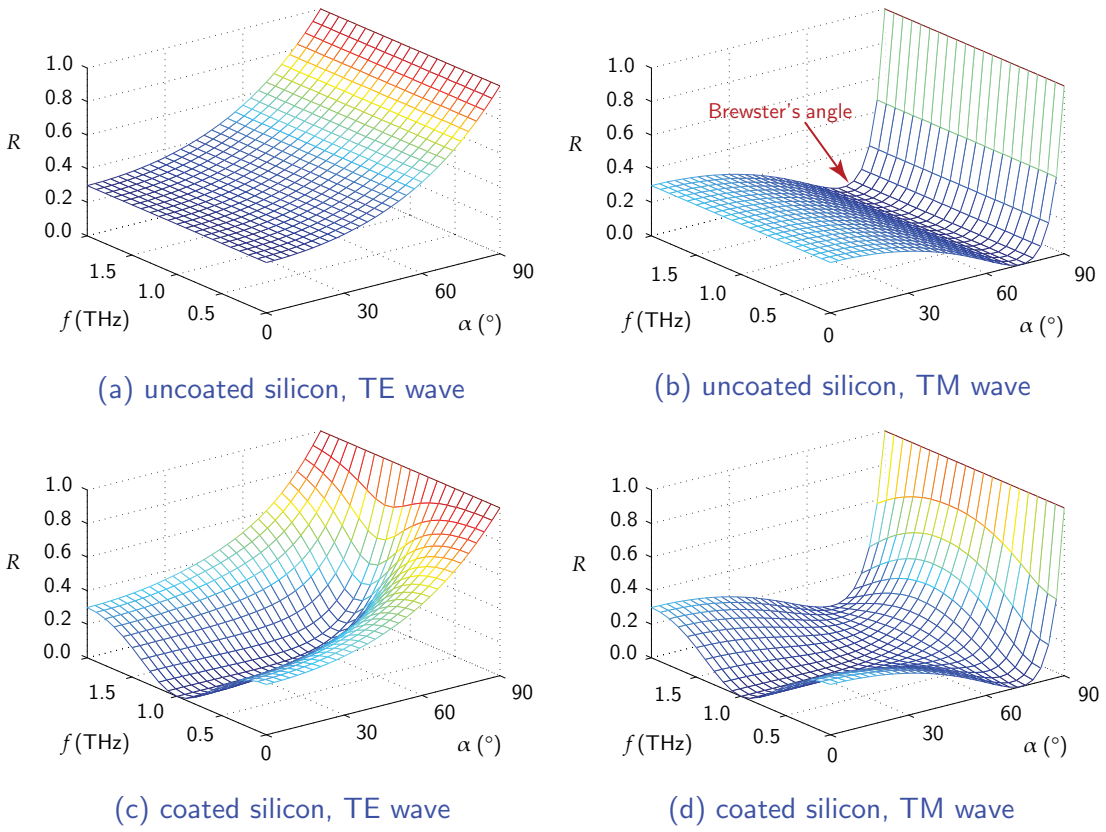


(a) uncoated silicon, TE wave

(b) uncoated silicon, TM wave

(c) coated silicon, TE wave

(d) coated silicon, TM wave

**Figure 9.5. Model reflectance at air-silicon interface.** The reflectance is meshed versus the T-ray frequency, $f$, and the angle of incidence, $\alpha$. The silicon window has a frequency-independent refractive index of $n_{\text{Si}} = 3.418$ and no absorption. The coating material has a refractive index of $n_a = \sqrt{n_{\text{Si}}} = 1.85$, and the coating thickness is a quarter of 1-THz wavelength or $l_a = c/(4n_a \times 10^{12}) = 40.56$ $\mu$m. Brewster's angle for a air-silicon interface at $\alpha_{\text{Brewster}} = 73.69°$ can be seen in both cases of TM wave.

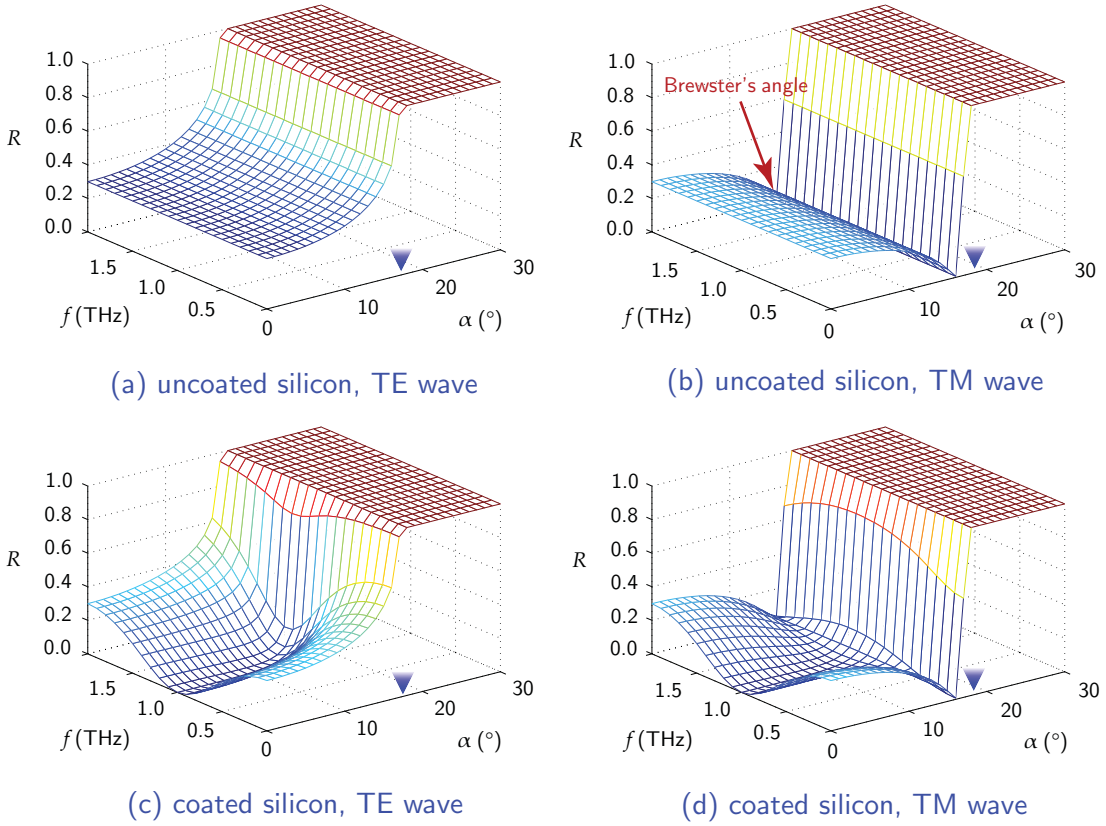


(a) uncoated silicon, TE wave

(b) uncoated silicon, TM wave

(c) coated silicon, TE wave

(d) coated silicon, TM wave

**Figure 9.6. Model reflectance at silicon-air interface.** All parameters are identical to those used in Figure 9.5, excepting that the field direction here is from silicon to air. The critical angle at $\alpha_{\text{critical}} = 17.01°$, marked by the blue arrowheads, and the total internal reflection beyond the critical angle can be seen in all cases.

a thickness of a quarter of 1-THz wavelength. The plots vary with the frequency and angle of incidence, and also depend on the polarisation (TE or TM wave).

Consider Figure 9.5 for which the field propagation direction is from the air to silicon window. In the case of the uncoated window in Figure 9.5(a) and (b), the reflectance is constant over the frequency range for a particular angle of incidence. For TM wave there appears *Brewster's angle*, at which the reflectance is zero. When the window is coated with a perfectly conditioned material, the reflectance, as shown in Figure 9.5(c) and (d), becomes zero at a selected frequency—1.0 THz in this case, and lowered in both wings, for both TE and TM waves. However, the general reflectance characteristic of the coated window is still similar to that of the uncoated one. One feature that is hardly observable from the model reflectance for the coated window is that, as the angle of incidence inclines from the normal, the optimal frequency where the reflectance

becomes zero experiences redshift. This is because a longer apparent optical axis in a coating layer can accommodate a longer wavelength.

A similar effect is observable when the field direction is from the coated window to the air, as shown in Figure 9.6 (c) and (d). The reflectance is zero at a desired frequency and lowered on both sides of the spectrum. However, in this case the zero reflectance is limited by total internal reflection at and beyond the *critical angle*. The total internal reflection blocks the field transmission at all frequencies regardless of the polarisation or the existence of a coating layer.

Nevertheless, these model reflectances are considered at a single surface of the window. In fact there are two additional effects involved in the real situation—the effect of Fabry-Pérot interference introduced by the window, which causes fringes in the spectrum, and the effect of reflectance at the exit face of the window. These effects will be incorporated into a calculation, based on the characteristic matrix method, and will be shown in Section 9.6.2.

### 9.6.2 Transmittance of coated windows

The model transmittance of a window simulated in this section includes the effects from front and back coatings and parallel window surfaces. The window and coatings have the same parameters as those used in Figure 9.5. The transmittance of the uncoated window is shown in Figure 9.7(a). The fringes in the transmittance (green solid line) are caused by Fabry-Pérot interference between the internal reflections between two parallel surfaces of the window. If these reflections are removed, the transmittance will be flattened over the frequency range (red dotted line). When the window is coated on one surface, the transmittance at a desired frequency—1.0 THz in this case—is enhanced from 0.5 to 0.7, as shown in Figure 9.7(b). Obviously, the fringes at 1.0 THz is reduced, as a result of the coating. When the window has coating layers on both surfaces, the transmittance at 1 THz is further enhanced from 0.7 to unity, as depicted in Figure 9.7 (c).

In the real situation, the fringes that plague a spectrum are hard to remove if the window is measured with conventional frequency-domain spectroscopy. However, with THz-TDS this seems to be possible, since a THz-TDS system transmits short coherent T-ray pulses which are temporally resolved at the detector. Once a pulse encounters

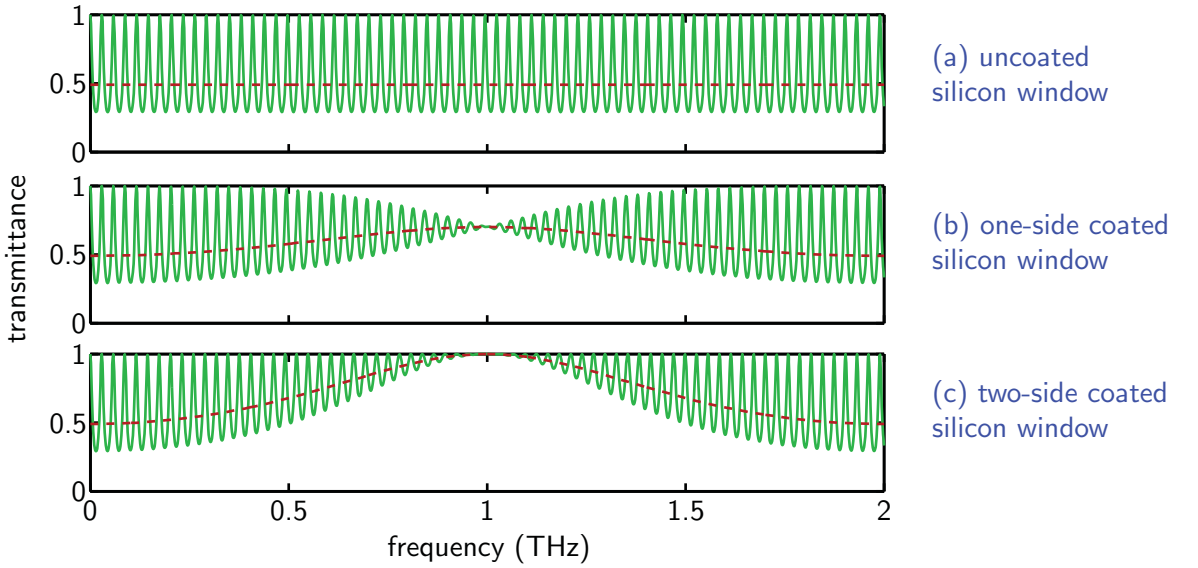


**Figure 9.7. Model transmittance of silicon window at normal angle of incidence.** The thickness of the silicon window is set to 1.5 mm. The coating material is set to have the index of refraction $n_a = \sqrt{n_{\text{Si}}} = 1.85$, and the thickness is a quarter of 1-THz wavelength or $l_a = c/(4n_a \times 10^{12}) = 40.56$ $\mu$m. The green solid lines indicate the transmittance incorporating Fabry-Pérot interference within the silicon window, and the red dotted lines indicate the transmittance without the interference within the window.

internal reflections and takes a longer transmission path, it will be delayed, and can be easily removed via windowing in the time domain if the pulse duration is shorter than the delay time.

## 9.7 Transparent materials for antireflection windows

It has been shown in Section 9.5 that, in the operation of an antireflection window, the interference mechanism dominates the frequency response, and hence the window and coating should be *non-dispersive* and *non-absorptive* in the T-ray frequency band. Though, a limited number of T-ray transparent materials have been reported thus far. Fortunately, the low absorption property of these materials implies that the frequency dependence of the index of refraction is small, i.e., non-absorption implies non-dispersion (Birch *et al.* 1981). Some of the common T-ray transparent materials, including high-purity silicon and low-loss polymers, are discussed below. Further information on the optical constants of these and other low-loss materials for T-ray frequencies can be found in Lamb (1996) and Simonis (1982) and references therein.

**Table 9.1. Optical constants of selected materials.** The data shown are indices of refraction, $n$, and absorption coefficients, $\alpha$, measured at room temperature. The data are compiled from (a) Loewenstein *et al.* (1973) (below 2.1 THz), (b) Grischkowsky *et al.* (1990) (below 2.0 THz), and (c) Fischer (2005) (below 2.8 THz). The numerical discrepancies are possibly due to differences in manufacturing and testing processes. Empty entries mean that data are unavailable.

| Material | (a) | | (b) | | (c) | |
|---|---|---|---|---|---|---|
| | $n$ | $\alpha$ (cm$^{-1}$) | $n$ | $\alpha$ (cm$^{-1}$) | $n$ | $\alpha$ (cm$^{-1}$) |
| $SiO_2$ (Fused silica) | | | 1.95 | <8.0 | 1.95 | <15.0 |
| High-resistivity silicon | 3.4175 | <0.7 | 3.418 | <0.1 | 3.41 | <0.5 |
| Synthetic diamond | | | | | 2.36 | <0.5 |
| Germanium | 4.006 | <0.4 | 4.0 | <3.0 | | |
| Gallium Arsenide | | | 3.59 | <2.5 | | |

### 9.7.1 Float-zone silicon

Typically, high-resistivity silicon plays an important role as a bulk material for T-ray components, such as lenses, beam splitters, or windows. In addition to its desirable physical and chemical properties, silicon's exceptional transparency and non-dispersive properties at T-ray frequencies are the most attractive in general. A high-resistivity (>10 kΩ cm) and high-purity silicon crystal, grown by the float-zone (FZ) method, shows, below 2 THz, an absorption coefficient lower than 0.05 cm$^{-1}$ and a constant index of refraction of 3.418±0.001 (Ohba and Ikawa 1988, Grischkowsky *et al.* 1990, Dai *et al.* 2004). Moreover, the optical isotropy of silicon allows flexible orientation, regardless of the polarisation of the incident T-rays and the crystal orientation (Grischkowsky *et al.* 1990). Its optical properties are shown in Table 9.1 in comparison to other common materials.

### 9.7.2 Low-loss polymers

Many types of low-loss polymers are available, and some are listed in Table 9.2. Comparative to silicon, low-loss polymers are superior in terms of the conformation to the surface. It is possible to mould the polymers to any shape; in particular, polymer films with thicknesses in the order of T-ray wavelengths are viable. However, almost all

**Table 9.2. Optical constants of selected low-loss polymers.** The data shown are indices of refraction, $n$, and absorption coefficients, $\alpha$, measured at room temperature. The data are compiled from (a) Smith and Loewenstein (1975) (at 1.5 THz), (b) Birch *et al.* (1981) (below 1.2 THz), (c) Fischer (2005) (below 2 THz), and (d) Jin *et al.* (2006) (below 2.5 THz). The discrepancies are possibly due to differences in manufacturing and testing processes. Empty entries mean that data are unavailable.

| Material | (a) | | (b) | | (c) | | (d) | |
|---|---|---|---|---|---|---|---|---|
| | $n$ | $\alpha$ ($cm^{-1}$) | $n$ | $\alpha$ ($cm^{-1}$) | $n$ | $\alpha$ ($cm^{-1}$) | $n$ | $\alpha$ ($cm^{-1}$) |
| LDPE | | | 1.5138 | <0.5 | | | | |
| HDPE | 1.518 | 1.4 | 1.5246 | <0.5 | | <5.0 | 1.534 | <3.0 |
| TPX® | 1.447 | 6.0 | 1.4600 | <0.5 | 1.43 | <1.0 | | |
| PTFE | | | 1.4330 | <0.5 | | <1.5 | 1.445 | <3.0 |
| PCTFE | | | | | 1.43,1.50 | <4.0 | | |
| PS | | | 1.5912 | <2.0 | | | | |
| Cycloolefines | | | | | 1.5-1.6 | <0.5 | | |

polymers exhibit a weak birefringence, i.e., the index of refraction that is dependent upon the incident direction and the polarisation (Smith and Loewenstein 1975). Moreover, unlike semiconductors, the optical properties of polymers vary from sample to sample (Fischer 2005), and are dependent on many manufacturing parameters (Smith and Loewenstein 1975). This variability suggests the need to measure the optical properties of each sample prior to its implementation.

In addition to those conventional polymers, two other types of polymers, i.e., picarin ($n \approx 1.52$) and cyclic olefin copolymer ($n \approx 1.52$), have been introduced recently (Sengupta *et al.* 2006). Unprecedented by other polymers, these two polymers have a remarkable transparency in both T-ray and visible (including UV and NIR) frequency regions. This double-transparency property is beneficial for optical-pump/THz-probe experiments (Greene *et al.* 1991, Zielbauer and Wegener 1996). At declining cost, these new polymers are commercially available in many forms.

## 9.8 Coating techniques

Several coating techniques are commonly available for optical components, and coated optical components can be found in a number of daily-used devices, e.g., camera lenses, glasses, screen panels, and so on. Also the coating effect can occur in nature, so-called thin-film interference or *iridescence*, which is visible as colourful patterns. Samples of natural coatings are soap bubbles, oil in water, and heated metals. For optical wavelengths, coating thicknesses of a fraction of micron satisfy the interference condition, and thin film coating technologies, such as a vacuum evaporation or sputtering, and coating materials, such as $MgF_2$, SiO, or ZnS, can support such degrees of thicknesses.

But when it comes to longer T-ray wavelengths, much thicker coating layer(s), up to tens of microns, are necessary to satisfy the interference condition. The coating materials and techniques used in optics are no longer applicable to these wavelengths (Shao and Dobrowolski 1993), because the materials themselves are not transparent when exposed to T-rays, and a deposited material cannot form a thick layer. Thus, researchers have proposed alternative coating approaches suitable for FIR frequencies. Some approaches are as follows:

**Material adhesion** involves preforming a thin film of material with a suitable index of refraction to a desired thickness. This film is then applied to a substrate surface in vacuum to avoid bubbles between layers. They could be attached together by means of (i) a supporting frame with no adhesive (Krumbholz *et al.* 2006, Turchinovich *et al.* 2002), (ii) adhesive (Kawase and Hiromoto 1998), or (iii) thermal bonds (Englert *et al.* 1999, Armstrong and Low 1974).

**Chemical vapour deposition (CVD)** involves a chemical reaction of suitable gases in a controlled chamber, which results in desired materials deposited onto a prepared substrate. The possible deposition techniques for FIR filter fabrication are tetraethylorthosilicate-CVD (DeCrosta *et al.* 1996) and plasma-enhanced CVD (Hosako 2003).

**Spin coating** enables coating of a material on a flat surface via centrifugal force. An amount of a volatile solution is laid onto a substrate, which, afterwards, is spun at a considerable speed to spread out the solution until the desired thickness is

**Table 9.3. Comparison of microlayer fabrication techniques.** The comparisons are given in general terms, and the characters could be different from these for a particular technique.

| Character | Adhesion | Deposition | Spin coating |
|---|---|---|---|
| Proper coating materials | Limited | Less limited | Less limited |
| Fabrication time | Short | Long | Moderate |
| Fabrication temperature | Normal | High | Normal |
| Fabrication equipment | Simple | Complicated | Moderate |
| Durability | Low | High | Moderate |
| Formability | No | Yes | No |
| Uniformity | Low | High | High |

obtained. The thickness of a coating depends on many factors, including the spinning speed, solute concentration, etc (Lawrence 1988).

In general, there is a tradeoff between fabrication complexity and layer coating quality, when selecting the appropriate coating method. CVD definitely requires complex equipment, and the deposition time is directly proportional to the coating thickness. However, the final result is durable and uniform even on a complex substrate surface. Material adhesion, in opposition, is much simpler in terms of fabrication, but a coating cannot be applied to an uneven surface. Furthermore, a coating is prone to peeling off a substrate unless heating is applied to the structure during fabrication (Armstrong and Low 1974, Englert *et al.* 1999). Spin coating might be a compromise in terms of the simplicity and durability. General comparisons among the techniques are given in Table 9.3. In addition, comparisons among many specific methods can be found in Hosako (2004).

## 9.9 Experiments and results

Due to its common use in T-ray systems, high-resistivity silicon is used as the window material in this experiment. For the perfect transmittance, the coating material should have an index of refraction equal to the square root of the silicon's index, or $\sqrt{3.418} = 1.85$. However, an ordinary material with the closest index is a series of polymers, which has the index of approximately 1.5. This discrepancy is tolerable with a slightly lower antireflection performance.

Since the thickness of an antireflection coating for T-rays is in the order of tens of microns, it is possible to use a common PE sheet, which has a thickness ranging from ten to a hundred microns. Using a preformed PE sheet as a coating not only avoids a complex material fabrication technique, but also opens up the possibility of retrofittable and interchangeable antireflection layers in T-ray systems. During an experiment, the coating thickness can be rapidly changed to enhance the transmittance at desired frequencies.

### 9.9.1 Optical properties of materials

Prior to testing for the transmittance of coated windows, the optical properties of bulk materials, which will be used for the window and coating, are measured, as they may possess some characteristic features introduced during the production processes. A silicon wafer that will be used as a window, even though having a high resistivity, may have a high absorption due to impurities. PE sheets often differ in their optical characteristics, since the production process varies for each manufacturer.

#### Silicon window

Supplied by *Siltronix*, the window used in the experiments is an undoped (100) CZ-grown silicon wafer polished on both sides with the thickness of $1.5213 \pm 0.0021$ mm and the diameter of 102 mm. Through transmission-mode THz-TDS, the optical constants in the frequency range from 0.2 to 1.0 THz can be found, as shown in Figure 9.8. The measured index of refraction of the wafer is almost constant and comparable to the value of 3.418 for float-zone silicon reported by Grischkowsky *et al.* (1990). However, the measured absorption coefficient here is two orders of magnitude larger, in particular at low frequencies. Since the wafer is polished to the optical grade on both sides, the scattering effect at the surfaces is negligible. Therefore, the high absorption could be attributed to impurities as a consequence of the ingot growing process.

#### Polyethylene coating

Two LDPE sheets with the total thickness of $95.9 \pm 4.6$ $\mu$m are put together and measured for the optical constants in the T-ray frequency range. A thickness variation in a low-grade PE sheet is relatively large. This can affect the measurement of the optical

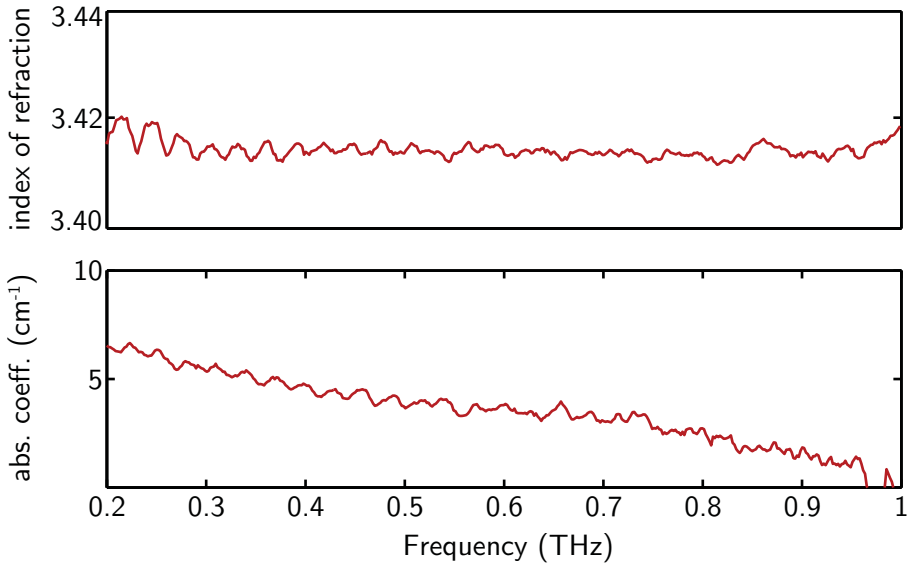


**Figure 9.8. Measured optical constants of silicon.** The index of refraction is constant over frequencies of interest, whereas the absorption coefficient is high at low frequencies. The fringes exist in both the refractive index and absorption coefficient are as a result of Fabry-Pérot interference within the window.

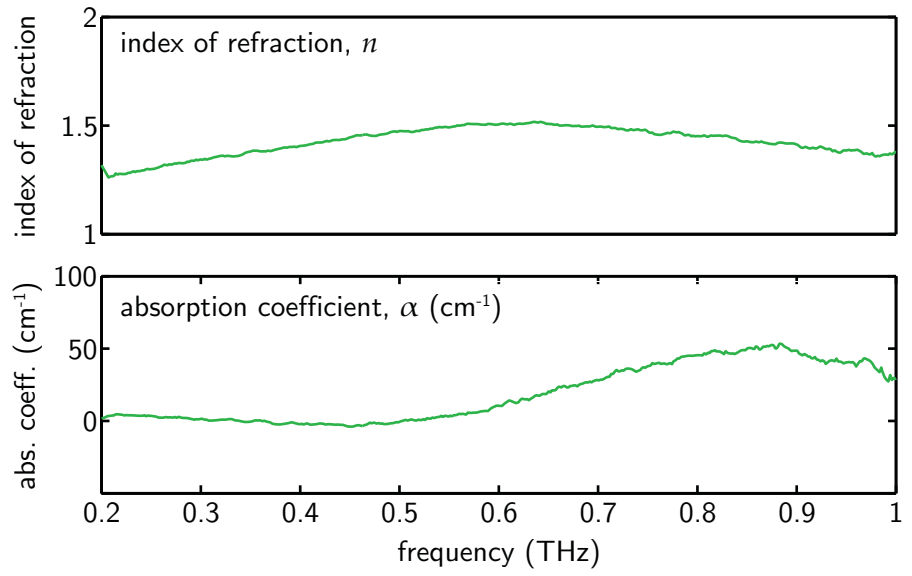


**Figure 9.9. Measured optical constants of polyethylene.** The index of refraction varies strongly with the frequency. The absorption coefficient is small from 0.2 to 0.5 THz, and increases rapidly after 0.5 THz.

constants and, furthermore, the performance of the coating. Figure 9.9 shows the index of refraction and the absorption coefficient of the PE sheet. In contrast with the value found by Birch *et al.* (1981), the measured index of refraction varies over the frequency range, rather than being fixed at 1.51. In addition, the absorption coefficient grows rapidly in the frequency range from 0.5 to 1.0 THz. Impurities, bubbles, and surface scattering could be associated with such a high absorption.

### 9.9.2 Assembling of antireflection windows

In order to allow rapid change of the coating, PE sheets are stuck onto the window via a supporting frame without adhesion, as demonstrated in Figure 9.10. Changing the coating thickness is simply carried out by replacing or adding PE sheets. The antireflection performance is verified for two coating thicknesses, $48 \pm 2.3$ $\mu$m and $103 \pm 10$ $\mu$m. The thicker coating is composed of two polyethylene sheets, one has the thickness of $48 \pm 2.3$ $\mu$m and the other has the thickness of $55 \pm 7.6$ $\mu$m. The coating is applied to both sides of the silicon window. According to the quarter-wavelength formula in Equation 9.29, and assuming the index of refraction of polyethylene is 1.5, the thin coating would be optimal at 1.04 THz, and the thick coating at 0.49 THz.

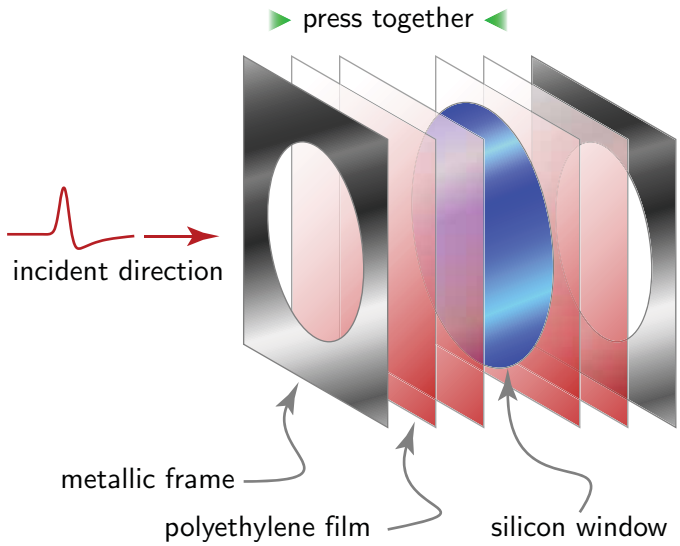


**Figure 9.10. Retrofittable coating system.** Multiple sheets of PE are press fitted together against the silicon window via the metallic frame. Combined together, these PE sheets perform as an antireflection coating for the silicon window. Note that polyethylene sheets cannot support a vacuum due to their porosity.

### 9.9.3 Transmittance of coated windows

The transmittance of the thinly-coated and thickly-coated windows are shown in Figure 9.11 and 9.12, respectively, in comparison with the transmittance of the uncoated window. In either case of coating, the fluctuations after the main T-ray pulse prohibit removal of the reflections in the time domain, and thus the Fabry-Pérot fringes persist in the transmittance spectra. In addition, the overall low transmittance of both coated and uncoated windows is ascribed to the absorption of bulk silicon, grown by the CZ method. The fringes and absorption do not hinder interpretation, as the relative transmittance of the coated and uncoated windows is rather of importance. In the frequency range between 0.7 and 1.0 THz, the thinly- or thickly-coated window exhibits a lower transmittance than that of the uncoated window, because of the intrinsic absorption of the PE sheets that becomes large in this frequency range (see Figure 9.9). The high absorption of PE prevents observation of the antireflection performance between 0.7 and 1.0 THz.

In Figure 9.11 the thinly-coated window shows an enhancement in the transmittance broadly from 0.3 to 0.6 THz, with the maximum at 0.45 THz. The position of the maximum enhancement is in contradiction with the theoretical central frequency at 1.04 THz. For the thickly-coated window, the transmittance in Figure 9.12 exhibits two enhancements at 0.3 and 0.6 THz. Again, these positions are in conflict with the expected central frequency at 0.49 THz and its odd harmonic at 1.47 THz. Even though variations in the coating thickness are taken into consideration, the uncertainties in the central frequencies are still not large enough to justify the measured results. The reason behind these inconsistencies will be discussed in Section 9.9.4.

### 9.9.4 Analysis of measured transmittance

From the previous section, it is obvious that the measured transmittances are far different from expectation. A possible reason is that air gaps might be present between the coatings and the window, since no adhesive nor vacuum is applied between them. In order to prove this assumption, the characteristic matrix method is employed to simulate situations where narrow air gaps exist between the thin or thick coating and the window.

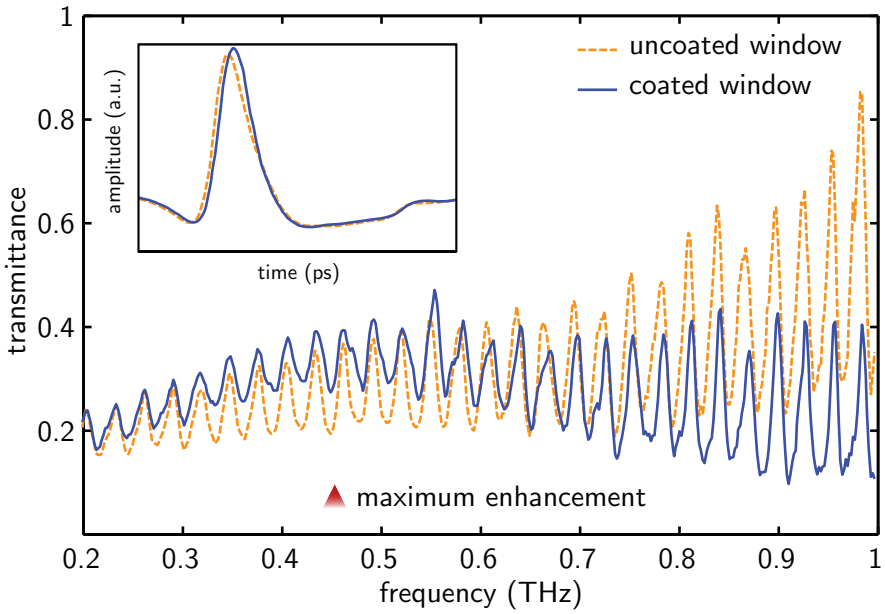


**Figure 9.11. Measured transmittance of thinly-coated window.** The coated silicon window shows the maximum transmittance enhancement at 0.45 THz. The inset shows the main T-ray pulses passing through the uncoated and coated windows. The pulse for the coated window is slightly delayed and intensified as a result of the coating.

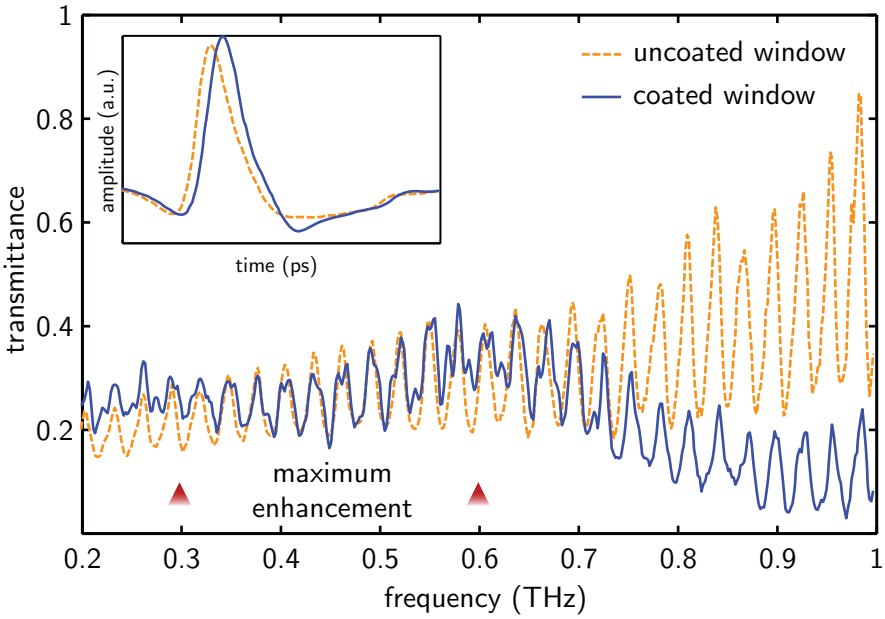


**Figure 9.12. Measured transmittance of thickly-coated window.** The coated silicon window shows the maximum transmittance enhancement at 0.3 and 0.6 THz. The inset shows the main T-ray pulses passing through the uncoated and coated windows. The pulse for the coated window is slightly delayed and intensified, particularly in the high-frequency components, as a result of the coating.

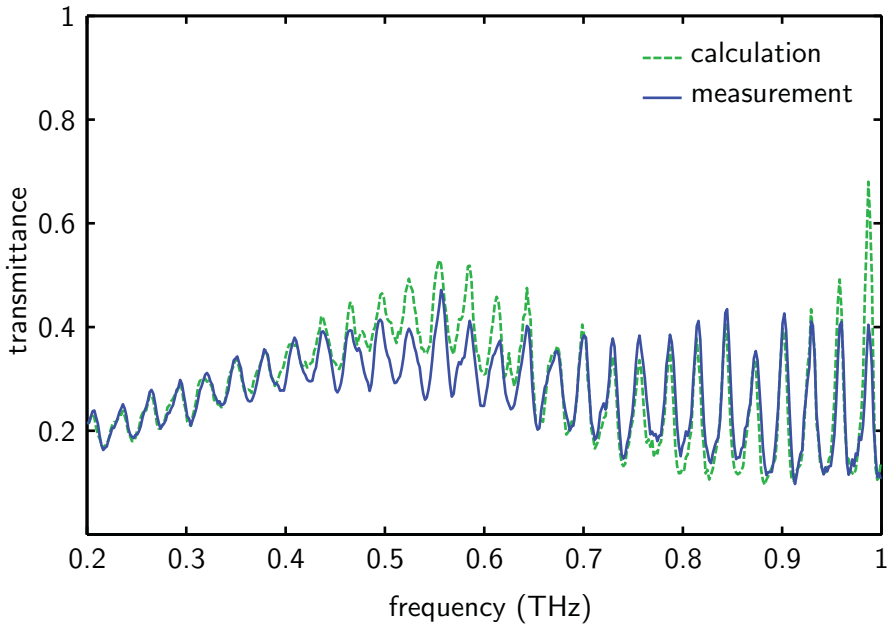


**Figure 9.13. Calculated and measured transmittances of thinly-coated window.** Two air gaps, each of which has the thickness of 45 $\mu$m, are inserted between the coating and the window in the calculation.

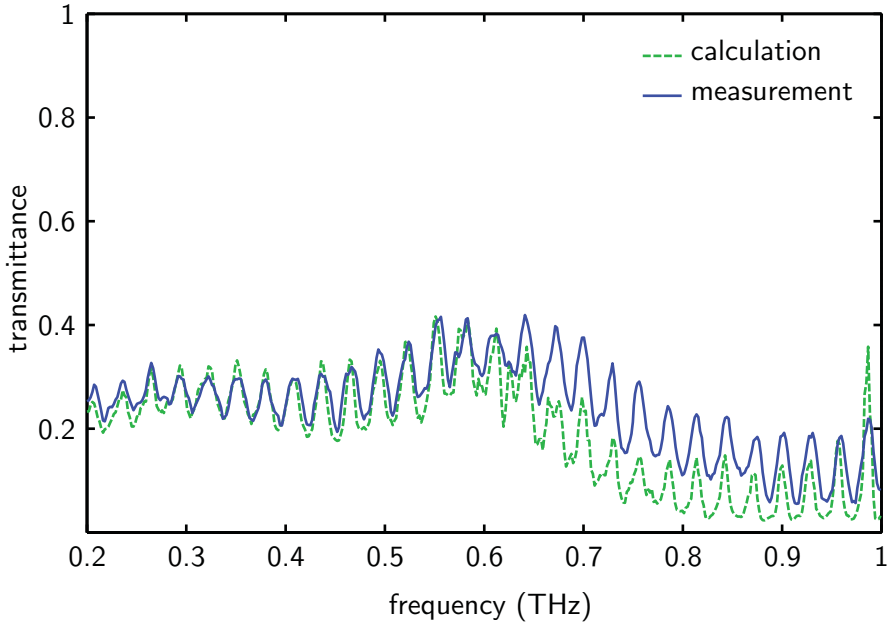


**Figure 9.14. Calculated and measured transmittances of thickly-coated window.** Four air gaps, each of which have a thickness of 65 $\mu$m, are inserted between the coating and the window in the calculation.

Figure 9.13 compares the calculated and measured transmittances of the thinly-coated window. In the calculation, two air gaps are set between the front and back coatings and the window, and the optical constants of the silicon and PE are taken from the experiment in Section 9.9.1. The thickness of the air gaps is varied in steps until the calculated transmittance is close to the measured transmittance. The theoretical thickness of each air gap is found to be around 45 $\mu$m.

Similarly, for the thick coating case, four air gaps are assumed between the four PE sheets and the window. The calculation reproduces the transmittance when the gap thickness is 65 $\mu$m. The comparison between the calculated and measured transmittances for the thick coating is shown in Figure 9.14

The transmittance calculation by using the characteristic matrix method confirms that the implemented retrofitting antireflection introduces the air gaps between the window and the coating. Despite that, the antireflection is still effective, but its operational frequencies are offset from the theoretically designed frequencies.

## 9.10 Conclusion and potential extensions

So far, not many researchers have addressed the problem of window reflections in the T-ray frequency region, in spite of the wide use of windows in THz-TDS systems. In response to that, quarter-wavelength antireflection coatings for transparent windows operated with T-rays have been studied in this chapter. The retrofittable system, allowing rapid interchange of the coating thickness and coating material to accommodate desired frequencies, is also demonstrated.

In the experiment, a silicon wafer, as a window, is coated by PE sheets with various thicknesses. Even though the index of refraction of the PE coating is not perfectly suited to the silicon window, the coating enhances the window transmittance to a promising degree. However, the operational frequencies of the coating deviate from theoretical expectation. Through a characteristic matrix analysis, it is found that the air gaps present between the coatings and the window are responsible for the discrepancy.

A quarter-wavelength antireflection coating, demonstrated with T-rays in this chapter, is effective in a narrow spectral range. A better antireflection performance, in terms of an operational bandwidth, is possible via metamaterial coatings (Biber *et al.* 2004,

Brückner *et al.* 2007), as mentioned earlier. In addition, a further improvement could be attained using graded-index coatings. With this type of coating the EM wave can pass through the window omnidirectionally with virtually no reflection at a very broad frequency range. Graded-index coatings have been realised in the optical regime via nanorod deposition (Gevaux 2007, Xi *et al.* 2007). Furthermore, an optional extension to multilayer coatings, which are effective in dual frequency bands, as proposed by Li *et al.* (1992), is appealing for some applications.

Having discussed the implementation of T-ray antireflection coating in this chapter, in Chapter 10, also in Part III—T-ray optics, we demonstrates multilayer interference filters that guide/block portions of the T-ray radiation. The operation of the filters can be analysed via the characteristic matrix method, discussed earlier in Section 9.4.

Chapter 10

# Quarter-Wavelength Multilayer Interference Filters for T-rays

NUMEROUS applications for T-rays require a frequency-selection technique to filter out an unwanted portion of the frequency band. As T-ray characteristics are quasi-optical, the techniques that have been developed for optics can be applied directly to T-ray frequencies. An interesting technique for frequency selection is based on interference in a multilayer structure. This chapter proposes construction and characterisation of quarter-wavelength multilayer interference filters operated with T-rays, where a particular interest is given to the stop-band attenuation resulting from the filter structure.

## 10.1 Introduction

Modern T-ray systems have opened up the relatively unexplored frequency range lying between the microwave and infrared. Consequently, a range of optical components are required to manipulate T-rays, inasmuch as optical components are required to control visible, infrared, or ultraviolet radiation. These components may comprise lenses, mirrors, parabolic mirrors, beam splitters, filters, polarisers, and so on. Most of the components, which have been proposed, directly adopt principles from optics. This is possible since T-ray characteristics are quasi-optical (Goldsmith 1992).

One of the common wave-manipulating components is a filter, which helps increase SNR in some broadband systems. In the case of an electronic detector with an amplifier, removal of unwanted frequencies with a filter leads to a greater amplifier gain without saturating the amplifier. A number of T-ray filters have been realised to date, due to the requirements of either conventional FTIR (Fourier Transform Infrared) spectroscopy (Griffths and de Haseth 1986) or astronomical observations (Seeley *et al.* 1981). These filters can be categorised into two major types, according to the applied optical power, as active or passive filters. An active T-ray filter offers more flexibility in frequency and/or energy tuning, but at the expense of complexity and cost. A passive filter, on the other hand, is less complicated, but also less flexible in terms of its function.

Several approaches to passive T-ray filters are available, for example, reststrahlen reflection (Turner *et al.* 1965), particle scattering (Armstrong and Low 1974), photonic bandgap crystals (Özbay *et al.* 1994a, Özbay *et al.* 1994b), perforated metal sheets (Renk and Genzel 1962, Ulrich 1968, Winnewisser *et al.* 1998, Winnewisser *et al.* 1999, Winnewisser *et al.* 2000), and interference in a multilayer structure. A multilayer interference filter[13] is an attractive option because of its structural simplicity yet optical functionality. By using alternating thin films of T-ray transparent materials, with a proper index arrangement, full control over a particular frequency band is easily attainable.

This work presents a study of the quarter-wavelength multilayer interference filter. The operating frequency range covers the frequency of most ultrafast T-ray systems, i.e., between 0.1 and 1.0 THz (Abbott and Zhang 2007). Our emphasis is on operation

[13]For simplicity in the following context an interference filter refers to a multilayer interference filter and not other types of filters exploiting a similar interference mechanism. The same structure may be found in other optical functions, and/or called by different names such as multilayer periodic structure, dichroic filter, 1D photonic bandgap structure, 1D photonic crystal, Bragg mirror, dielectric mirror, etc.

in the transmission mode, and the effects of altering the number of filter layers on the transmittance profile. The study of these effects is facilitated by the fact that the sub-millimetre structures allow a rapid change of the layer arrangement. Characterisation of the fabricated filter by THz-TDS delivers a time-domain signal, rarely achievable by other spectroscopic modalities. This evolving time-domain signal reveals significant characteristics of the filter, in addition to the information obtainable from the transmittance profile.

This work is organised as follows: Previous findings on T-ray multilayer interference structures are given in Section 10.3. Section 10.4 provides the principle of quarter-wavelength multilayer interference filters. Section 10.5 shows how the filter response varies as a function of several parameters, including the optical length of each layer, the step between high and low indices of refraction, and the number of periods. The discussion of suitable materials and fabrication methods for the filters is given in Section 10.6. Experimental results for a fabricated filter are given in Section 10.7.

## 10.2 Research objective and framework

### Objective

- To design a series of quarter-wavelength multilayer interference filters, which are operable with THz-TDS systems, i.e., in the frequency range between 0.1 and 1.0 THz or higher. This design is on a par with that of optical interference filters, which are operated at a higher frequency range.

- To fabricate the designed filters from a set of suitable materials by an appropriate fabrication method. The suitable materials imply that they have minimal dispersion and absorption in the T-ray frequency regime. An appropriate fabrication method calls for simplicity, economy, and reliability.

- To characterise these fabricated filters using THz-TDS, in a transmission mode, which reveals time-resolved broadband signals unattainable by any other class of terahertz spectroscopy. Particular emphasis is given to the effects on the spectral response as a function of the number of periods in the filter.

### Framework

The assumptions of the measurement carried out here are that: (i) an interference filter under measurement has parallel and flat surfaces, (ii) the angle of the incident T-ray beam is normal to the surface of the filter, (iii) the incident beam is collimated, (iv) dry air surrounds the T-ray path and the filter, and also fully purges any air gaps within the filter structure, (v) the reference signal is measured under the same conditions as the sample signal, except for the absence of the sample, and (vi) the transverse dimension of the filter is large enough, so that no edge diffraction affects the result.

## 10.3 Review of multilayer interference structures

For decades, FTIR spectroscopy has been widely employed in the study of materials in the frequency range around the MIR (Griffths 1983). Accordingly, multilayer interference structures operative in this frequency range, made of a number of different materials in various arrangements, are widely available. Provided there is no absorption, the structures can be operated either as a filter or mirror dependent on the alignment, as the two functions are complementary. Some multilayer structures used as FTIR mirrors are, for example:

**Zinc sulphide/polyethylene** (Shao and Dobrowolski 1993). Zinc sulphide (ZnS) layers were deposited onto PE sheets, the combination of which performed as a narrow band mirror in the 1.5 to 6.0 THz frequency range ($n_{\mathrm{ZnS}} = 3.0$, $n_{\mathrm{HDPE}} = 1.53$, $n_{\mathrm{LDPE}} = 1.51$, $\kappa_{\mathrm{PE}} < 2 \times 10^{-3}$).

**Silicon/air** (Schiwon *et al.* 2003). Multilayer broadband mirrors were constructed from one to six layers of silicon wafers ($n = 3.418$, $l = 10\ \mu$m) interleaved by vacuum gaps ($n = 1$, $l = 44\ \mu$m). Through FTIR spectroscopy, the mirrors showed a nearly constant reflectance spectrum from 1.2 to 3.9 THz and the optimum reflectance at 2.34 THz for the field incident at 40°. The structure was used to build a resonator cavity.

Other similar multilayer structures are designed for the frequencies between 0.1 and 1.0 THz, and characterised by THz-TDS. A series of these designs are, for example:

**Styrolux$^{TM}$/PE and PE/air** (Turchinovich *et al.* 2002). An all-plastic mirror was constructed from alternation of PE ($n = 1.74$, $l = 200$ $\mu$m) and Styrolux$^{TM}$ ($n = 1.59$, $l = 310$ $\mu$m) films. The mirror showed the high reflectivity at the fundamental frequency of 187 GHz with a FWHM of 16 GHz. Scattering by the rough film surfaces was responsible for a low transmission at high frequencies. Achieving a wider FWHM required two materials with a larger step in the refractive indices, which were realised by PE films ($n = 1.73$, $l = 100$ $\mu$m) and air gaps ($n = 1$, $l = 200$ $\mu$m). The transmittance showed a fundamental stop-band at 386 GHz with a FWHM of 169 GHz. The invention was patented for its quarter-wavelength configuration and for the operation in the frequency range between 5 GHz and 2 THz (Knobloch *et al.* 2005).

**Polypropylene/silicon** (Krumbholz *et al.* 2006). A T-ray omnidirectional mirror was built from five layers of polypropylene ($n = 1.53$, $l = 150$ $\mu$m) mediated by four layers of high-resistivity silicon ($n = 3.418$, $l = 63$ $\mu$m). Characterised by THz-TDS in transmission and reflection modes, the mirror could reflect more than 95% of the incident power with frequencies between 319 and 375 GHz at all incidence angles regardless of the polarisation. The structure provided a higher reflectivity than did the plastic mirror reported by Turchinovich *et al.* (2002). By re-sequencing the layers, the structure shows a sharp transmission peak inside a stop-band (Rutz *et al.* 2006b).

**Alumina/alumina-zirconia** (Rutz *et al.* 2006a). A rigid continuous structure was made by tape casting and sintering of alumina ($n = 3.17, l = 73$ $\mu$m) and alumina-zirconia ($n = 4.16$, $l = 51$ $\mu$m) into 25 alternating layers. Measured in the transmission mode, this ceramic structure provided a stop-band between 0.3 and 0.38 THz in the normal direction, and a common stop-band between 0.32 and 0.38 THz in all directions. However, due to a high loss introduced by zirconia, functioning of the filter or mirror was limited.

**PP/PP+$TiO_2$** (Jansen *et al.* 2007). A flexible mirror with a large step of refractive indices was made of polymeric compounds, i.e., polypropylene ($n = 1.5$, $l = 269$ $\mu$m) and polypropylene with $TiO_2$ additive ($n = 3.4$, $l = 111$ $\mu$m). Both materials were prepared by extrusion. The spectral response of the 5-period mirror showed the centre of the reflectivity at 200 GHz with a FWHM of 150 GHz in all directions and polarisations.

These earlier studies examined materials and fabrication techniques suitable for the operation of the multilayer structures in the T-ray frequency range. The fabricated structures were expected to be used as mirrors for short-range or indoor T-ray communication. Thus, particular interest was given to economic material fabrication, which provided structures with the highest reflectivity and broadest reflection band at any angle of incidence. Our work, on the other hand, studies the dependency of the structure's transmission characteristics on the number of material layers, when the structure is used as a filter. A rapid change in the number of material layers is possible owing to the large scale and retrofittability design of the structure. An elegant equation is derived, showing a logarithmic relation between the number of layers and the attenuation within a stop-band. Furthermore, our work supplements full data of the filter's response in terms of time-domain signals and phase responses. This serves to provide more insight into the operation of the filter, in addition to the spectral transmittance.

## 10.4 Quarter-wavelength multilayer interference filters

A multilayer interference filter is composed of several dielectric layers with different indices of refraction. Cascading these layers to form a periodic structure, as shown in Figure 10.1(a), gives the transmittance profile in the stacking direction similar to that shown in Figure 10.1(b). As the name implies, it is the interference mechanism that controls the shape and position of pass-bands and stop-bands. Particularly, constructive interference is responsible for the pass-bands, whereas destructive interference is responsible for the stop-bands. To achieve any type of interference at any desired frequency, the wave dispersion is the only parameter to be adjusted. This is made possible by means of proper material arrangement, given that each material is nondispersive, i.e., has a constant index of refraction, in the frequencies of interest.

Section 10.4.1 briefly discusses the characteristic matrix method, which is required to analyse the response of a multilayer structure. Section 10.4.2 explains the required quarter-wavelength optical thickness condition.

### 10.4.1 Characteristic matrix method

In order to analyse the response of the described periodic structure, the characteristic matrix method (Hecht 1987) is engaged. In brief, a characteristic matrix for a high-index material layer, in the case that the wave propagation direction is parallel with the stacking direction, is given by

$$\mathbf{M}_H = \begin{bmatrix} \cos\left(\frac{\omega}{c} n_H l_H\right) & j \sin\left(\frac{\omega}{c} n_H l_H\right) / n_H \\ j n_H \sin\left(\frac{\omega}{c} n_H l_H\right) & \cos\left(\frac{\omega}{c} n_H l_H\right) \end{bmatrix}, \tag{10.1}$$

where $n_H$ and $l_H$ are the refractive index and the thickness attributed to a high-index layer. Likewise, a matrix for a low-index layer is

$$\mathbf{M}_L = \begin{bmatrix} \cos\left(\frac{\omega}{c} n_L l_L\right) & j \sin\left(\frac{\omega}{c} n_L l_L\right) / n_L \\ j n_L \sin\left(\frac{\omega}{c} n_L l_L\right) & \cos\left(\frac{\omega}{c} n_L l_L\right) \end{bmatrix}. \tag{10.2}$$

Here, $n_L$ and $l_L$ are the refractive index and the thickness attributed to a low-index layer. When these layers of materials are stacked up to $a$ periods, with the high-index

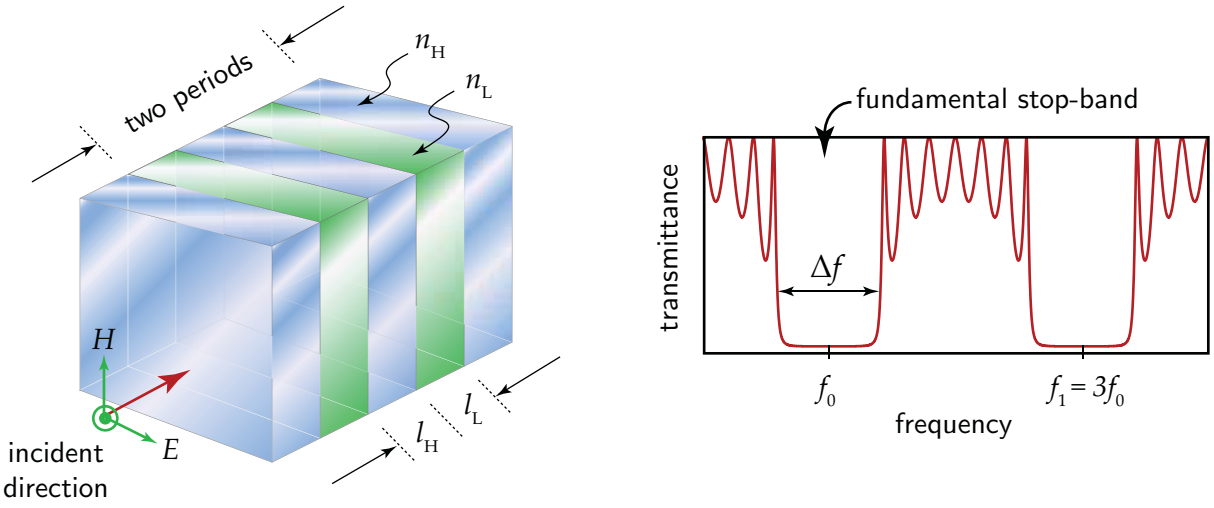


(a) periodic structure, 2.5 periods, $(HL)^2H$ (b) corresponding transmittance

**Figure 10.1. Multilayer interference filter and its transmittance.** (a) The structure comprises a number of dielectric periods. Each period is constructed from high- and low-index dielectric layers with the indices of refraction of $n_H$ and $n_L$, and the thicknesses of $l_H$ and $l_L$, respectively. The periodic structure usually starts and ends with a high-index material, and can be designated by $(HL)^aH$, where $H$ and $L$ symbolise high- and low-index materials, respectively, and $a$ is the number of periods. (b) The transmittance of this periodic structure features spectrally distributed stop-bands. The fundamental stop-band has a central frequency of $f_0$ and an effective width of $\Delta f$.

layers terminating both ends, the resulting characteristic matrix is simply obtainable via matrix multiplications in the proper order,

$$\mathbf{M}_{\text{total}} = \begin{bmatrix} m_{11} & m_{12} \\ m_{21} & m_{22} \end{bmatrix} = (\mathbf{M}_H \mathbf{M}_L)^a \mathbf{M}_H \, . \tag{10.3}$$

The transmission function of the structure in free space is calculated from the total characteristic matrix,

$$T(\omega) \;=\; \frac{2}{m_{11} + m_{12} + m_{21} + m_{22}} \, . \tag{10.4}$$

This transmission function, $T(\omega)$, is related to the transmittance, $\mathcal{T}(\omega)$, via $\mathcal{T}(\omega) = |T(\omega)|^2$.

### 10.4.2 Quarter-wavelength optical thickness

Essentially, due to destructive interference from multiple reflections, the transmittance of a dielectric layer with a refractive index $n$ and thickness $l$ has minima at

$$f_N \;=\; (2N+1)\frac{c}{4nl} \, ; \qquad N = 0, 1, 2, \ldots \, . \tag{10.5}$$

This set of minima can be utilised for stop-bands of the filter. However, a single layer cannot cause wide and deep enough stop-bands. Thus, alternate cascading of a number of layers made of two or more different materials, as illustrated in Figure 10.1, is required. In order to enhance the stop-bands efficiently, the minima of those layers must be at the same spectral position. This is made possible through an optical length equalisation:

$$n_H l_H = n_L l_L = \frac{c}{4 f_0} = \frac{\lambda_0}{4} \, , \tag{10.6}$$

where, again, the index of refraction and thickness of the high-index layer are denoted by $n_H$ and $l_H$, respectively, and those of the low-index layer are denoted by $n_L$ and $l_L$, respectively. From Equation 10.6, the optical thickness, $nl$, of a layer equals a quarter of the wavelength of the first minimum or the fundamental stop-band. Hence, this formulation leads to the term *quarter-wavelength multilayer interference filter* (Hecht 1987).

## 10.5 Effects of structural parameters on filter response

Each parameter of the structural design has effects on the filter spectral response in a unique way. The filter response, characterised by the position/width of the stop-band and the attenuation inside a stop-band, is controlled via these parameters: the optical length of each dielectric layer, the step between high and low indices of refraction, and the number of periods. This section analyses and illustrates the relations between the response of a quarter-wavelength interference filter and these factors.

### 10.5.1 Mathematical relations

From Equation 10.6, the central frequency of the first stop-band of the filter is given by

$$f_0 = \frac{c}{4nl} . \tag{10.7}$$

According to the equation, the optical length $nl$ directly designates the central frequency, $f_0$, of the stop-band. Decreasing the optical thickness causes a blue-shift in the central frequency. Changing $n$ and $l$ in reverse proportion has no effect on the frequency $f_0$.

Another important property of the filter is the width of a stop-band, $\Delta f$. It is influenced by the step between high and low indices of refraction, and is also scaled by the stop-band position. This relation is given by (Orfanidis 2006)

$$\frac{\Delta f}{f_0} = \frac{4}{\pi} \arcsin\left(\frac{n_H - n_L}{n_H + n_L}\right) . \tag{10.8}$$

If the difference between the two indices is small, the inverse sine and thus the width of a stop-band approaches zero. If the difference is large, the inverse sine approaches $\pi/2$, and the stop-band width approaches twice the central frequency. However, in general due to a limit in the material variety, the width of a stop-band is comparable to the value of the fundamental central frequency.

The last filter's property considered here is the attenuation inside a stop-band, in particular the attenuation at $f_N$, where $N = 0, 1, 2, \ldots$. Substituting the quarter-wavelength frequency from Equation 10.7 into Equations 10.1 and 10.2 yields, respectively,

$$\mathbf{M}_H = \begin{bmatrix} 0 & j/n_H \\ jn_H & 0 \end{bmatrix} \quad \text{and} \quad \mathbf{M}_L = \begin{bmatrix} 0 & j/n_L \\ jn_L & 0 \end{bmatrix} . \tag{10.9}$$

The total matrix is therefore

$$\mathbf{M}_{\text{total}} = (\mathbf{M}_H\mathbf{M}_L)^a\mathbf{M}_H = (-1)^a j \begin{bmatrix} 0 & n_L^a/n_H^{a+1} \\ n_H^{a+1}/n_L^a & 0 \end{bmatrix} , \tag{10.10}$$

where, again, $a$ is the number of periods in the filter. Following Equation 10.4, the magnitude of the transmission function at $f_0$ is

$$|T(f_0)| = \frac{2}{n_L^a/n_H^{a+1} + n_H^{a+1}/n_L^a} . \tag{10.11}$$

In the case that the difference between $n_H$ and $n_L$ is reasonably large, the above equation can be approximated to

$$|T(f_0)| \approx \frac{2}{n_H}\left(\frac{n_L}{n_H}\right)^a . \tag{10.12}$$

Taking a base-10 logarithm of the approximation results in

$$\log_{10}|T(f_0)| = a\log_{10}(n_L/n_H) - \log_{10}(n_H) + 0.3 . \tag{10.13}$$

It is obvious that the attenuation in the middle of a stop-band logarithmically depends on the number of periods, $a$. This relation is also applicable to the transmission at $f_N$, where $N = 1, 2, 3, \ldots$ and so on. Also note that the attenuation at these frequencies is independent of the physical thicknesses of the materials.

### 10.5.2 Simulation

The following simulations confirm the analytical expressions presented in Section 10.5.1. The simulations help illustrate the transmittance of the filter affected by changes in the optical thickness, the indices of refraction, and the number of periods. The results are determined on the basis of characteristic matrix analyses. The transmittance is reported in the range of 0 to 2 THz for the case of normal angle of incidence.

Effects of changes in the optical thickness on the central frequency and width of a stop-band are exemplified in Figure 10.2. Obviously, the figure shows an inverse relation between the optical thickness and the central frequency, as described by Equation 10.7. When the optical thickness changes from 300, 150, to 100 $\mu$m, the central frequency changes from 0.25, 0.5, to 0.75 THz, respectively. Also note that the width of a stop-band, $\Delta f$, is scaled in accordance with the central frequency—this relation is explained in Equation 10.8.

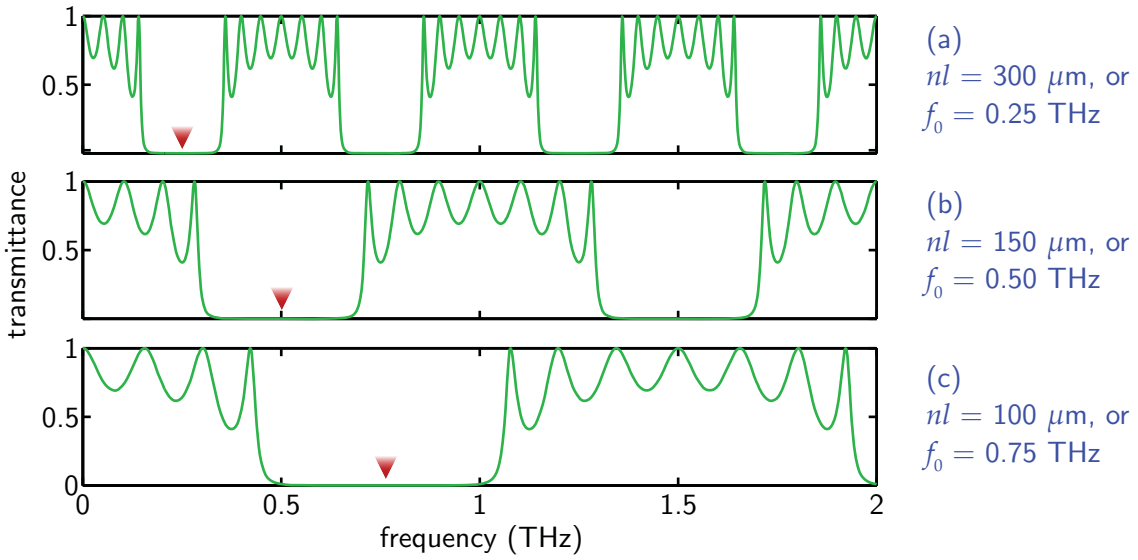


**Figure 10.2. Simulated filter transmittance as a function of optical thickness.** The structure is composed of 3.5 dielectric periods, designated by $(HL)^3H$. The high- and low-indexed materials have $n_H = 3.418$ and $n_L = 1$, respectively, and their thicknesses are determined from the optical thickness. The arrowheads indicate the position of $f_0$.

Figure 10.3 illustrates the transmittance influenced by changes of the materials' indices. Increasing the index difference widens stop-bands, as described in Equation 10.8. An interesting case is when $n_H = 3$ and $n_L = 1$, which allows $\Delta f = f_0$. In addition to the stop-band widening, increasing the index difference intensifies the attenuation inside a stop-band, as explained by Equation 10.13.

Finally, according to Equation 10.13, the number of periods, $a$, dictates the attenuation inside a stop-band. Consider Figure 10.4 where the number of periods evolves from 1.5, 3.5, to 5.5. The attenuation at the middle of a stop-band increases logarithmically, whereas the position and width of a stop-band remain unchanged. In a pass-band, increasing the number of periods results in stronger and more oscillatory transmittance ripples. It is worth noting that the number of layers should be reasonably low to prevent accumulative absorption from bulk material and scattering at material interfaces, which are not considered in the simulation.

## 10.6 Materials and fabrication techniques for the filter

This section provides some background discussion on materials and fabrication techniques, needed for realisation of a T-ray interference filter. Fundamental requirements

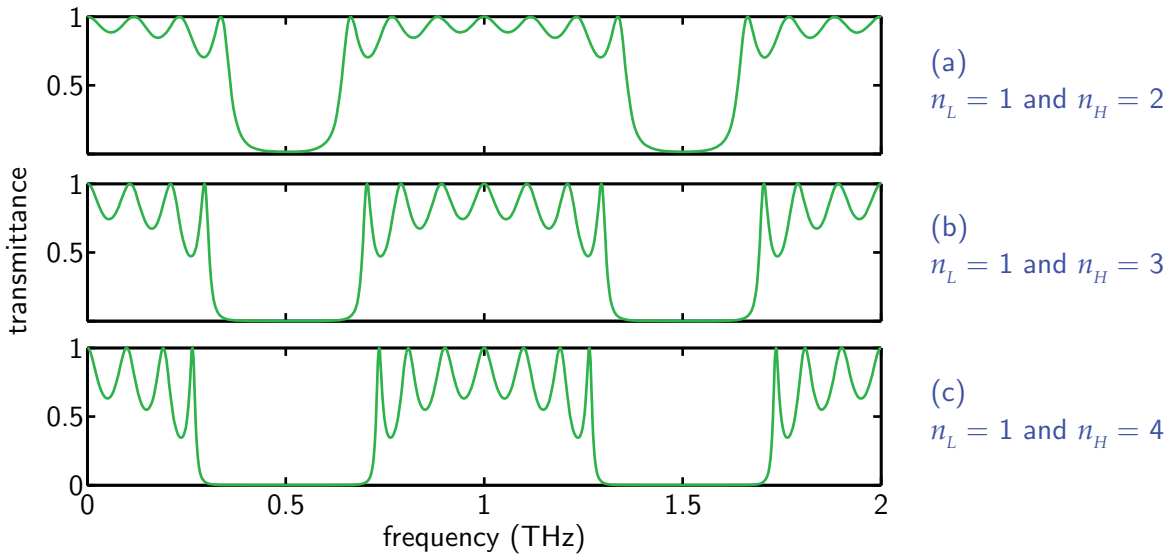


**Figure 10.3. Simulated filter transmittance as a function of refractive indices.** The structure is composed of 3.5 dielectric periods, designated by $(HL)^3H$. The optical length is 150 $\mu$m, or the central frequency is 0.5 THz, and the physical thicknesses are determined from the optical thickness.

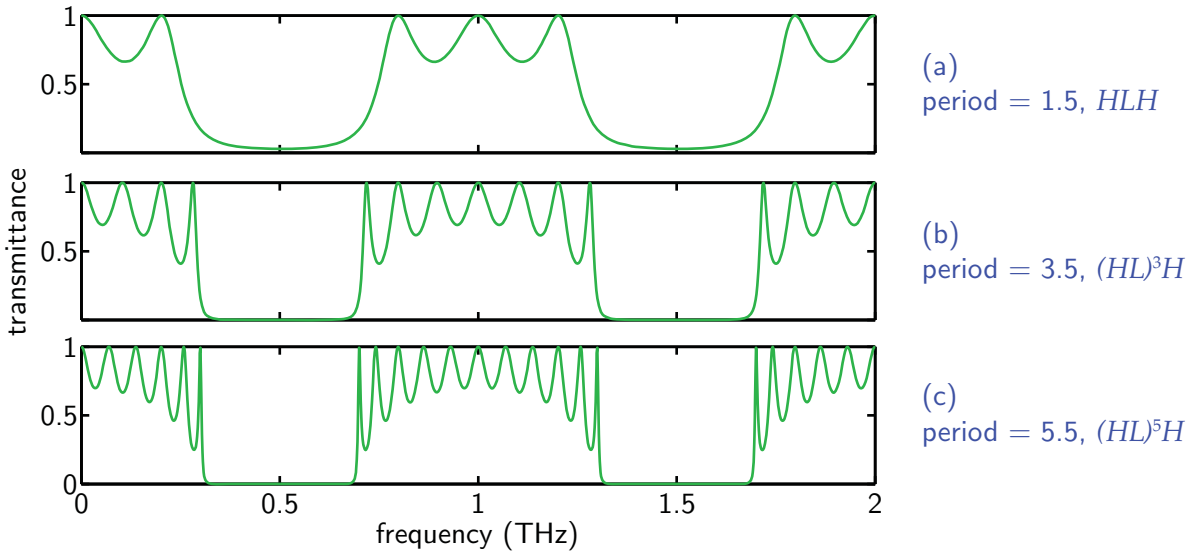


**Figure 10.4. Simulated filter transmittance as a function of the number of periods.** The optical thickness is 150 $\mu$m, or the central frequency is 0.5 THz. The high- and low-indexed materials have $n_H = 3.418$ and $n_L = 1$, respectively, and their physical thicknesses are determined from the optical thickness.

of material properties are similar to those required to realise optic filters, excepting that now the effective frequency range shifts toward the longer wavelength. This results in thicker material layers and completely different fabrication techniques.

### 10.6.1 Transparent materials

As mentioned earlier, a multilayer interference filter exploits the interference mechanism to control the stop-band and the pass-band. High efficiency of the interference mechanism is achievable, provided that each material is non-dispersive and non-absorptive in the T-ray frequency band. The non-dispersiveness of materials facilitates the design and sustains the uniformity of the interference mechanism throughout the frequencies of interest. The non-absorption, including low scattering, of materials avoids energy dissipation, which degrades the transmittance in the pass-band and also heats up the structure undesirably.

In addition to the absorptive and dispersive properties of materials, there are a number of other relevant factors, e.g., mechanical stability, chemical resistivity, thermal conductivity, birefringence, temperature dependency, or optical transparency. Though, the importance of each factor depends on a specific application. At this stage, for ordinary filter tasks, the interest is principally in the absorptive and dispersive properties of the material. In addition, some care is necessary to control mechanical stability and birefringence.

Two dielectric materials, which reasonably satisfy the above requirements and have a large difference in refractive index, are silicon and dry air. The first material, undoped high-resistivity float-zone (FZ) silicon, is known to have a negligible absorption and a constant refractive index of 3.418 at T-ray frequencies (Grischkowsky *et al.* 1990, Dai *et al.* 2004). The second material, dry air, has a unity refractive index and near zero absorption for T-rays. Both silicon and air have no birefringence, and the optical properties of silicon in the T-ray regime are independent of the crystal orientation.

### 10.6.2 Fabrication techniques

From the quarter-wavelength condition in Equation 10.6, it can be seen that the wavelength of T-rays in the submillimetre region requires the dielectric layers to have the

same order of thickness. This thickness requirement excludes most of the conventional methods, used for fabrication of optical components, because those methods are optimised for coating in the order of a few microns. Some other potential fabrication methods are suggested for T-ray components, for example:

**Material adhesion** assembles different dielectric materials by means of either a holder, adhesive, or thermal bond. The applicability of these methods depends on the types of materials in use. Examples of the structures that are assembled by these methods are, for instance, Turchinovich *et al.* (2002) or Krumbholz *et al.* (2006).

**Material deposition** employs a chemical process to deposit desired materials onto a substrate. This technique requires complicated deposition equipment. Furthermore, a practical deposit thickness is often in an order of a few microns, which is too thin for use with T-ray wavelengths. A thicker layer is possible at the cost of deposition time and mechanical instability.

**Hybrid method** utilizes both material adhesion and material deposition in the fabrication. A suitable material is deposited onto a thin film, which is, afterwards, stacked with other deposited films to form a multilayer periodic structure. This method is used by, e.g., Shao and Dobrowolski (1993).

**Air-gap method,** a special case of material adhesion, eliminates the requirement for a second material of different index of refraction by substitution of air or vacuum, which has an index of refraction of approximately unity. In addition to the constant index, this method has an advantage concerning a low effective absorption, since free space has no absorption at all frequencies or can be considered as an all-pass filter. Another advantage is that the problem of unintended air-gaps (Krumbholz *et al.* 2006), present between layers, vanishes. Implementations of this method can be found in, for example, Turchinovich *et al.* (2002) or Schiwon *et al.* (2003). For the above reasons, the air-gap method is also preferred in this work.

Other fabrication techniques suitable for constructing interference filters are, for example, plastic coextrusion or tape casting and sintering of ceramics (Rutz *et al.* 2006a).

For visible light and nearby frequencies, according to Equation 10.6, the thickness of each layer is in the order of submicrons, and thus a rigid substrate is required in order

to support the periodic structure. However, this is not true for T-rays for which the interference layer thickness is around a few tens to a few hundreds of microns. Therefore, all of the layers can be stacked to form a free-standing structure, and a substrate is unnecessary for the T-ray interference filter. This is beneficial because (i) the Fabry-Pérot fringes induced by a thick substrate can be easily removed from the spectrum, and (ii) the overall absorption of the structure is reduced.

## 10.7 Experiments and results

### 10.7.1 Design of the silicon-air filters

A batch of intrinsic FZ silicon wafers is supplied by *Siltronix*. Each wafer is polished on one side, has a resistivity of $> 1$ k$\Omega$, an orientation of (111), and a thickness of $50 \pm 5$ $\mu$m. Due to the Fabry-Pérot effect, or particularly the destructive interference, the transmission of a single wafer has a minimum at $f_0 = c/(4n_{si}l_{si}) = 0.439$ THz, given $n_{si} = 3.418$. This frequency is then set as the central frequency of the fundamental stop-band. The thickness of an air gap, $l_{air} = 170.9$ $\mu$m, is chosen to comply with the quarter-wavelength condition in Equation 10.6. The width of a stop-band is estimated at 0.32 THz, according to Equation 10.8.

The material layers, comprising silicon wafers and air-rings, are fitted together by a HDPE frame, which exerts pressure on the structure via the elastic force of four identical springs. This spring-tight design helps reduce uneven forces at different surface positions and for different numbers of layers. Also it facilitates the replacement and retrofitting of material layers. The layout and design of the structure is given in Figure 10.5.

### 10.7.2 Characteristics of the silicon-air filters

The THz-TDS system, used in characterisation of the filters, is a fibre-coupled T-ray Picometrix 2000, equipped with photoconductive antennae for T-ray generation and detection. The pumping laser is mode-locked Ti:Sa laser (MaiTai, Newport) with a central wavelength of 800 nm, a pulse duration of $<$80 fs, and a repetition rate of 80 MHz. The system produces T-ray pulses with a bandwidth from 0.1 to 1.0 THz and the maximum

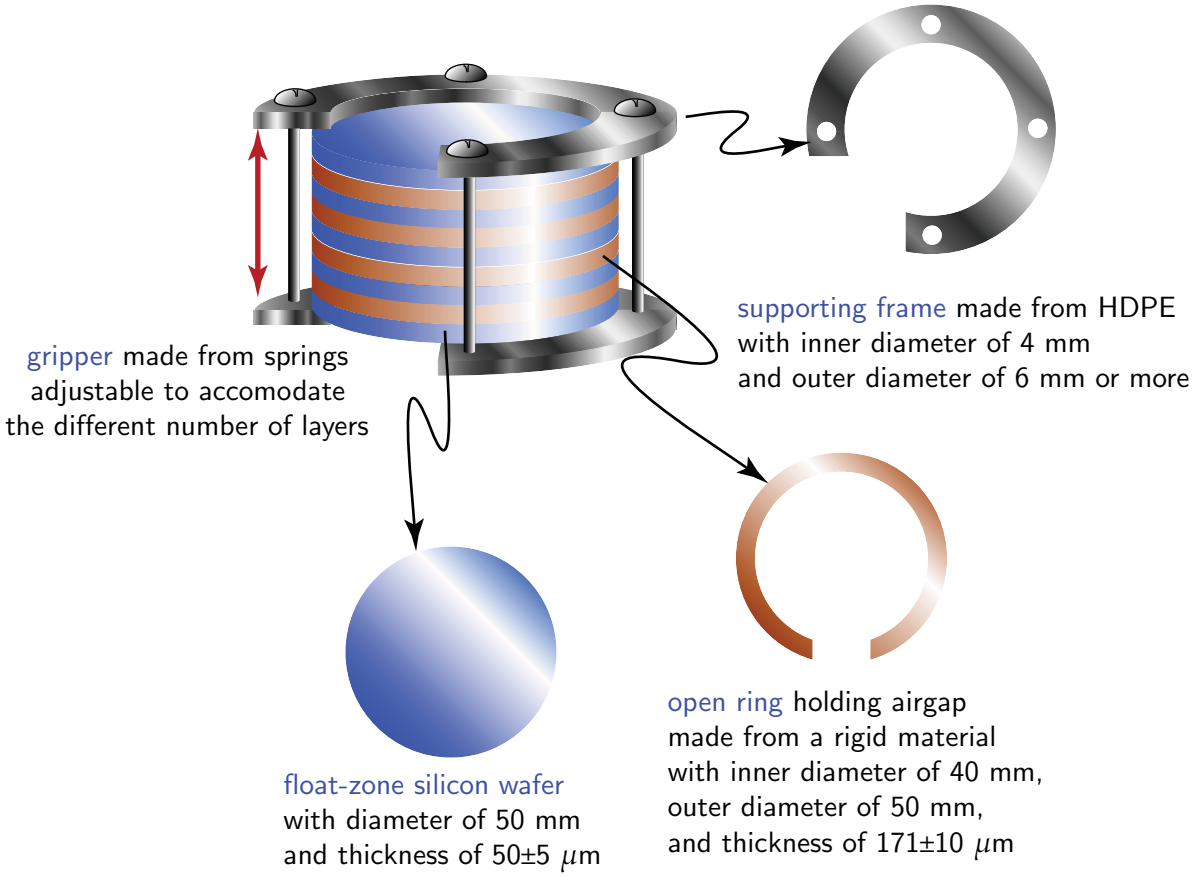


**Figure 10.5. Design of T-ray multilayer interference filter.** The filter is composed of FZ silicon wafers alternating with air gaps, created by open rings. The materials are held together by a supporting frame made from high-density polyethylene (HDPE), and therefore the layers can be readily swapped in and out, or changed. The diameter of the structure is wide enough, so that the T-ray beam can pass through without edge diffraction.

dynamic range of 25 dB. The T-ray beam passing through the filter is well collimated to avoid the difference in beam paths. The measurement for each filter is carried out nine times, and then the time-domain pulses are averaged. Also, the reference signal, measured with the same setting, is collected regularly to compensate amplitude drift effects within the system. For each recorded signal, the temporal window is 555.22 ps with a sampling interval of 33.9 fs. The Fourier transform of the pulse yields a spectral resolution of 1.8 GHz, and the reduction in system's bandwidth is not significant when the filter is in place.

Figure 10.6 shows a set of pulses recorded from the silicon-air interference filters with various numbers of silicon-air periods. Determined from the first zero crossing point, each signal is delayed from its neighbour by 0.5 ps. The greater delays of the pulses are

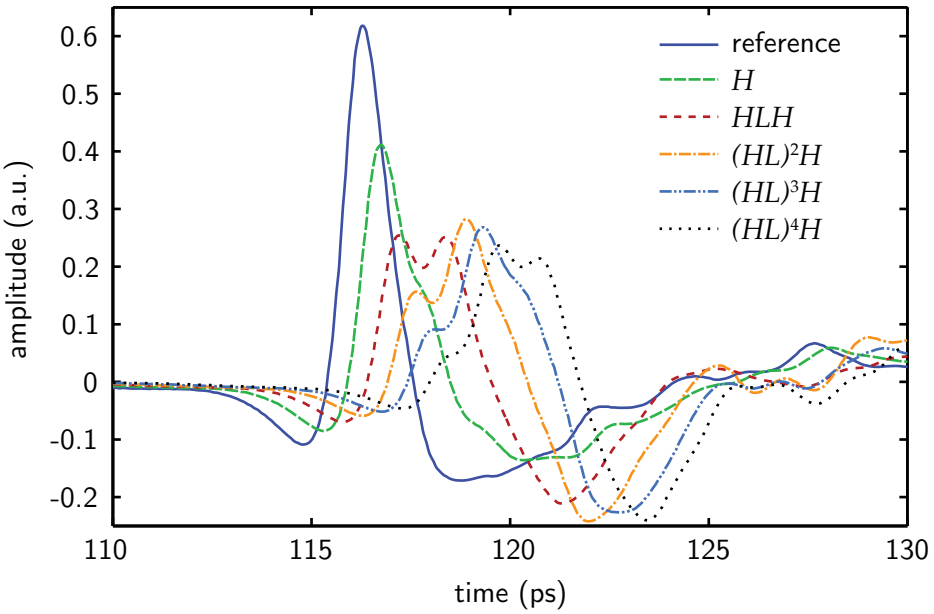


**Figure 10.6. T-ray signals transmitted through interference filters.** Only the signals inside the 20-ps window from the total recording duration of 555.22 ps are shown. The $H$ measurement in fact represents the signal recorded from a single 50-$\mu$m silicon wafer. The pulses are delayed, attenuated, and reshaped by the filters.

attributed to the increasing effective indices of refraction of the structures. The pulses for $(HL)^aH$ structures exhibit very little difference in the maximum amplitudes, which are approximately 40% of the reference amplitude. This is because the filters attenuate the amplitude at the specific frequency range while preserving the rest. However, the pulse shapes among the filters are largely distinctive. A possible likely cause is the spectral ripple in the pass-band, which is shown in the transmittance profiles (Figure 10.7).

The transmittances shown in Figure 10.7 are evaluated from the spectra of the reference, $E_{\text{ref}}(\omega)$, and of the filter, $E_{\text{fil}}(\omega)$, using $\mathcal{T}(\omega) = |E_{\text{fil}}(\omega)/E_{\text{ref}}(\omega)|^2$. From the figure, the first stop-band locates between 0.2 and 0.5 THz, the centre of which is at approximately 0.36 THz, and the FWHM is $\approx$ 0.3 THz. As the period of the filters increases, the attenuation in the middle of the stop-band increases logarithmically, roughly at an order of magnitude per period. This logarithmic relation confirms the theory in Equation 10.13, and is plotted explicitly in Figure 10.8. The filters have ripples in the pass-band, i.e. between 0.0 and 0.2 THz, and between 0.5 to 0.9 THz, which are stronger following the number of periods. Due to the limited dynamic range of the system, it is not possible to render the second stop-band, which is beyond 0.9 THz.

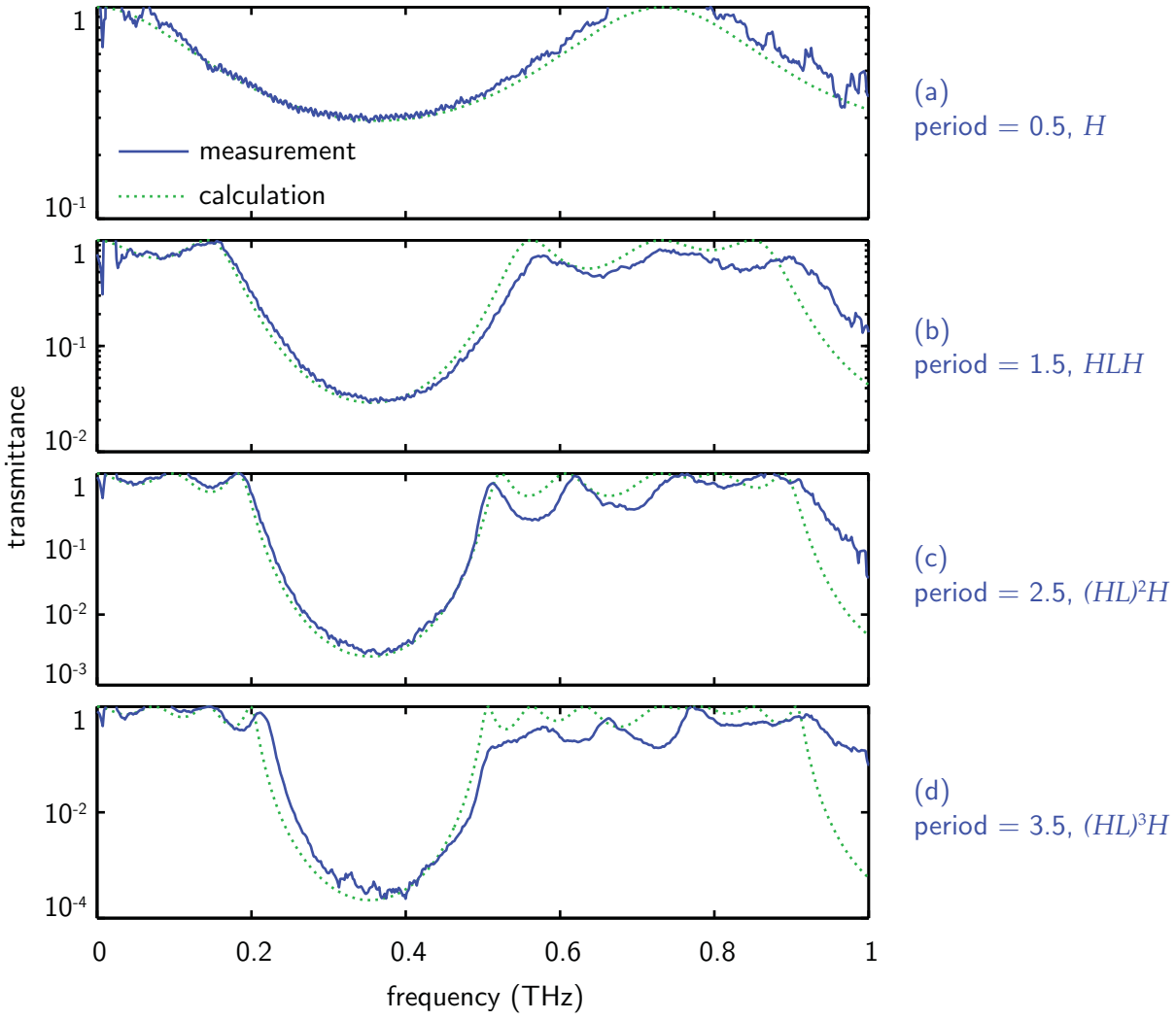


**Figure 10.7. Transmittance of interference filters.** For each filter, the first stop-band resides between 0.2 and 0.5 THz, centered at 0.36 THz. The successive stop-bands at higher frequencies are unresolvable due to the system bandwidth limit. The spectrum inside the stop-band of the $(HL)^3H$ filter is noisy, because the attenuation reaches the noise floor. The spectral transmittance for $(HL)^4H$ is not included, again due to the noise limit. The calculation is based on a characteristic matrix analysis. Notice the different ranges of the vertical scale.

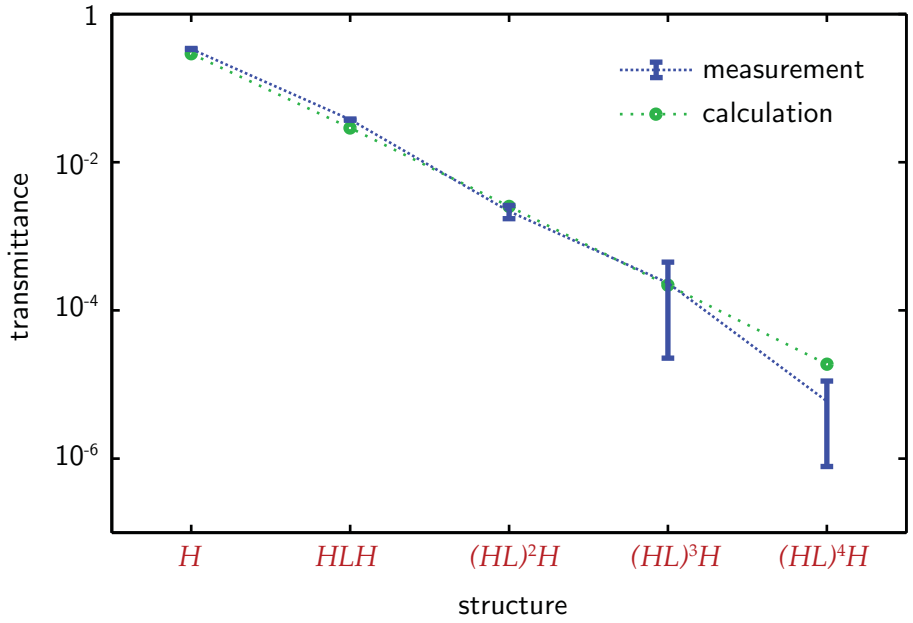


**Figure 10.8. Transmittance of interference filters at 0.36 THz.** The attenuation at the middle of the first stop-band increases logarithmically with the number of periods. The error bars represent one standard deviation either side of the mean—notice that the means appear skewed and the error bars appear magnified to the right hand side because the vertical scale is logarithmic. The calculation is based on Equation 10.13. The dotted lines merely assist interpretation.

The phase response is extracted using $\phi(\omega) = \angle E_{\text{fil}}(\omega) - \angle E_{\text{ref}}(\omega) - \omega L/c$. The $\omega L/c$ factor compensates the free space that occupies the structure's area with the thickness $L = a(l_H + l_L) + l_H$ in the reference measurement. The phase responses of the filters are shown in Figure 10.9. It is clear that the phase is anomalous in the stop-band, in the 0.2 to 0.5 THz region.

In spite of the appearance of the first stop-band, the central frequency of the stop-band deviates from the expectation at 0.439 THz. This is more likely due to uneven surfaces of the air-gap rings, which result in thicker air layers. Hence, in the simulation, an adjustment to the material parameters is performed to compensate the structural thickness uncertainties. Through the fitting, using a characteristic matrix analysis (Hecht 1987), the thicknesses of the silicon wafers and air gaps are estimated at 60 $\mu$m and 220 $\mu$m, respectively, whereas their indices of refraction remain unchanged. The simulation results accompany the measured transmittances and phase responses in Figures 10.7 and 10.9.

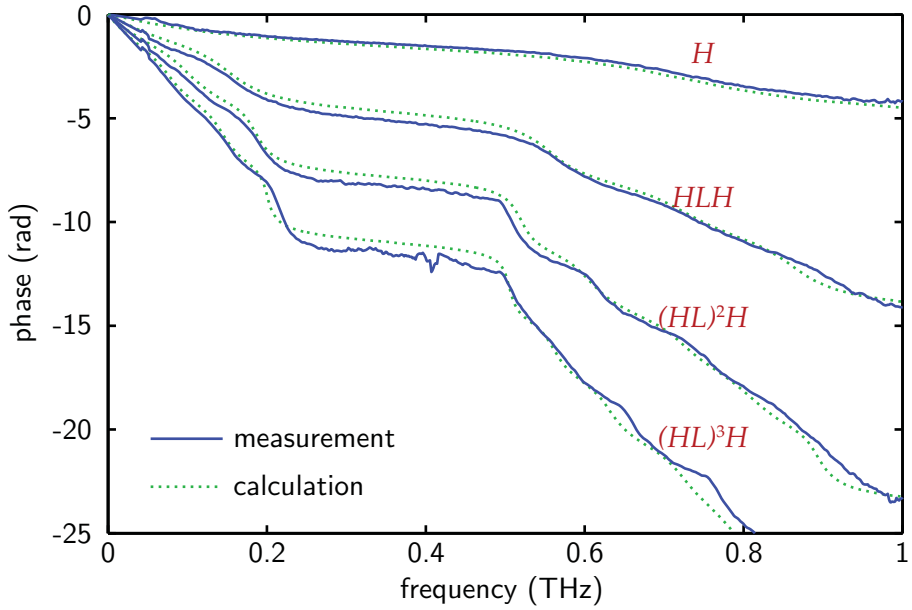


**Figure 10.9. Phase response of interference filters.** The phases are anomalous inside the stop-band, i.e. between 0.2 and 0.5 THz. The spectral phase of $(HL)^4H$ is not included here due to the limit of the system dynamic range. The calculation is based on a characteristic matrix analysis.

## 10.8 Conclusion and potential extensions

A multilayer interference structure has an ability to manipulate the T-ray radiation in a frequency-selective manner. This is the case despite the fact, most of the previous work focuses on its operation as a mirror, or more precisely, the structure is studied for its angle-dependent response to T-rays. Limited previous work presents its filtering characteristics following changes in structural parameters.

In our work, a set of the T-ray interference structures is designed to be operated as filter, in the transmission mode. Exploited in this work is a certain characteristic, namely the dependence of the stop-band attenuation on the number of filter layers. An explicit equation is derived, explaining the dependency in terms of a logarithmic relationship.

Realised according to the design, the filters are made from several ultrathin silicon wafers and air gaps, assembled in a novel retrofittable way. Characterised by transmission THz-TDS, the filters show an obvious stop-band spanning 0.2 to 0.5 THz with its central frequency at 0.36 THz. The transmittance in the stop-band decreases at approximately an order of magnitude per silicon-air period, as predicted by the theory.

A characteristic matrix analysis shows an agreement between the model and the measurements at the estimated thicknesses of the silicon and air gap of 60 $\mu$m and 220 $\mu$m, respectively.

Although the filter produces an apparent stop-band, it is known that the filter response is spectrally periodic. This may not be practical if other responses such as if high-pass, low-pass or band-pass are required. As a potential extension, filter cascading schemes are introduced. They enable construction of an interference filter with an arbitrary response. By cascading a set of multilayer interference filters, it is possible to shape up any desired frequency response. Cascading of filters could be either in a transmission-mode arrangement, where the total transmittance, $\mathcal{T}_{\text{total}}$, is calculated from (Winnewisser *et al.* 1999)

$$\mathcal{T}_{\text{total}} = \mathcal{T}_1 \mathcal{T}_2 \ldots \mathcal{T}_m \,, \tag{10.14}$$

or a reflection-mode arrangement (Shao and Dobrowolski 1993),

$$\mathcal{T}_{\text{total}} = \mathcal{R}_1 \mathcal{R}_2 \ldots \mathcal{R}_m \,, \tag{10.15}$$

where $\mathcal{T}_m$ and $\mathcal{R}_m$ are the individual transmittances and reflectances of each filter, respectively. Arrangement of a filter in a reflection mode is somewhat more difficult than arrangement in a transmission mode, as illustrated by some examples in Figure 10.10.

In the construction of the filter, although float-zone silicon is exceptionally transparent to T-rays, its cost is rather high. A number of other low-loss materials can substitute silicon in construction of the filter, with slightly inferior transparency. Bolivar *et al.*

NOTE:
This figure is included on page 296
of the print copy of the thesis held in
the University of Adelaide Library.

**Figure 10.10. Interference filter cascading in reflection arrangement.** Possible schemes for cascading 2, 3, and 4 interference filters (mirrors) in a reflection arrangement. In practice, the tilted angle of filters can be so small that the polarisation dependence of filter response is negligible. After Shao and Dobrowolski (1993).

(2003) suggests a range of low-loss yet low-cost dielectric materials, including steatite, alumina, titania loaded polystyrene, and zirconium-tin-titanate. The refractive indices of these materials span a wide range, which helps facilitate the design. Recently, in addition to those dielectrics, some polymers are introduced, e.g., picarin and cycloolefins (Sengupta *et al.* 2006). These polymers are transparent to both T-rays and visible light, and thus are attractive for some applications.

This chapter concludes Part III, T-ray optics, which is the last part of the thesis. In the next chapter we summarises each individual chapter from Chapters 6 to 10 in the aspects of its background, methodology, result, future work, and original contributions.

# Chapter 11

# Thesis Summary

THIS chapter concludes the thesis. Chapters 1 to 4 contain review material that embraces THz-TDS hardware, applications, and essential signal processing techniques. Chapters 5 to 10 contain the original contributions, divided into three major parts: signal enhancement and classification, system evaluation and optimisation, and T-ray optics. This chapter focuses on summarising the original contributions reported so far.

## 11.1 Part I—signal enhancement and classification

### Removal of water-vapour effects from THz-TDS measurements: Chapter 5

**Background:** Ambient water vapour is coupled to T-rays via its molecular rotational transitions. In a THz-TDS measurement, this interaction leads to the appearance of sharp resonances in the T-ray spectrum and corresponding fluctuations following the main pulse in the time domain. These water vapour effects can mask the spectroscopic data of the target. An effective solution to the problem is to purge the entire T-ray beam path with dry air or a nonpolar gas, which does not interact with T-rays. This approach, however, is not applicable to all situations.

**Methodology:** Digital signal processing is engaged in tackling the problem. A model of water vapour resonances is precisely constructed from a spectroscopic database, which provides all the essential resonance characteristics. This model is then deconvolved from the measurement data. Theoretically, the deconvolution should completely remove the water vapour effects, but in fact many discrepancies between the model and measurement exist. An elegant procedure allows fine-tuning of the model to the measurement before the deconvolution is carried out.

**Result:** The method has a moderate success with removal of the effects from the experimental data. The quantitative measures demonstrate a significant improvement in all aspects. In the time domain, the fluctuations after the main pulse are remarkably reduced. Yet, in the frequency domain the corresponding spectra contain the distorted resonances that are not removable. The distortion results from either the congestion of the resonances or the noise in the measurement.

**Future work:** An improvement to the proposed method is required to deal with these distorted resonances that cannot be modelled accurately, i.e. the method must be insensitive to the resonance distortion. The method is envisaged for removal of the contaminating responses from the experimental data in the case that the sources of the responses cannot be physically eliminated during the measurement.

**Original contribution:** For the first time, a means of digital signal processing is exploited to eliminate the artefacts introduced by ambient water vapour in THz-TDS measurements (Withayachumnankul *et al.* 2008b).

### Classification of THz-TDS signals with subtle features: Chapter 6

**Background:** A number of materials have unique responses to the T-ray frequencies. These responses manifest themselves as sharp resonances in the frequency domain and fluctuations in the time domain—the unique features that are visually distinguishable. However, some other materials do not produce such fingerprint responses, and in many cases the measured signals available from THz-TDS are nearly inseparable for different materials of the same general class. A method substituting for visual recognition is hence demanded.

**Methodology:** Machine learning, an effective and robust solution to a variety of classification and recognition problems, is involved in the classification of THz-TDS signals. Each THz-TDS signal measuring a sample is decomposed into a set of coefficients via wavelet transform. These coefficients, compactly representing the original signal, serve as the classification features that are relevant to the problem. A linear-kernel SVM, as a classifier, is trained and tested by these features. It is expectable that the trained SVM is capable of classifying similar signals.

**Result:** Using a particular set of wavelet coefficients as classification features, the trained SVM can distinguish two highly correlated groups of signals measuring two types of samples with an exceptional accuracy. The number of wavelet coefficients in use is only a fraction of the number of data points in the original signals. The compact representation of wavelet coefficients effectively wards off the curse of dimensionality usually encountered in classification problems.

**Future work:** The selection of relevant wavelet coefficients is based on trial and error. A more efficient feature selection method is necessary. Furthermore, the classification accuracy can be enhanced by using either adaptive wavelet transform or wavelet packet algorithms to decompose the signals into a set of coefficients serving as classification features.

**Original contribution:** For the first time, a robust machine learning method, together with a wavelet transform, is exploited in order to classify THz-TDS signals that possess broad indistinct features in the frequency domain (Withayachumnankul *et al.* 2005).

## 11.2 Part II—system evaluation and optimisation

### Uncertainty in THz-TDS measurements: Chapter 7

**Background:** THz-TDS is a technique capable of measuring the responses of materials with the T-ray frequencies. Numerical parameter extraction is required to derive the frequency-dependent optical constants of materials from the measurement. Though, the sources of errors exist at the measurement stage and throughout the parameter extraction process. These errors contribute to the uncertainty in the extracted optical constants. So far no analytical method has been developed for characterising the impact of these errors on the optical constants.

**Methodology:** A transmission-mode THz-TDS system is identified for its potential sources of measurement errors that have an influence on the measured optical constants. These sources encompass signal noise, approximations of the physical model, and deviations in sample alignment and thickness measurement. The developed uncertainty model quantifies the impact of these sources on the optical constants by means of the law of propagation of uncertainty. All the analyses and expressions of uncertainty, where applicable, follow an industrial standard recommended by ISO.

**Result:** The MCS method, as a benchmark for the developed uncertainty model, reveals the similarity between the analytical and numerical results for a wide range of situations. The validity of the analytical model is also confirmed by an implementation with experimental data. Though, small disparity between the analytical and numerical results can be observed in some cases. The disparity more likely results from a first-order approximation used in deriving the uncertainty model.

**Future work:** The analysis can be extended to cover other unaccounted sources of error. These sources are, for instance, the nonidealities of the sample and probe beam. A higher-order approximation for the propagation of uncertainty can decrease the difference between the analytical and numerical results, at the expense of complexity and computational time. In addition, other arrangements of THz-TDS, such as reflection-mode THz-TDS, can also benefit from similar analyses.

**Original contribution:** For the first time, the sources of error existing throughout the THz-TDS measurement process are exhaustively identified and quantified, based on the industrial guideline for expression of uncertainty (Withayachumnankul *et al.* 2008c, Withayachumnankul *et al.* 2007b).

### Material thickness optimisation for THz-TDS: Chapter 8

**Background:** In a transmission-mode THz-TDS measurement, a material sample that is too thick or too thin can raise the problem of measurement uncertainty. Although a greater thickness allows T-rays to interact more with bulk material, the measurable SNR rolls off with thickness due to stronger signal attenuation. A sample that is too thin renders itself nearly invisible to T-rays, in such a way that the system can hardly sense the difference between the sample and free space path. It appears that a full analysis of the sample thickness for THz-TDS has not been realised so far.

**Methodology:** The analysis for the optimum sample thickness is carried out through the uncertainty model proposed in Chapter 7. The model, which expresses the variance in the optical constants in terms of the variance in the signal amplitudes, is determined for its saddle point with respect to the thickness. It turns out that the optimum thickness equals twice the inverse of the absorption coefficient or twice the penetration depth. Theoretically, this thickness should result in the minimal uncertainty of the measured optical constants.

**Result:** The derived model for the optimal thickness is supported by the results from the experiments, performed with a number of materials with different T-ray characteristics. For a particular case, the standard deviation in the measured optical constants can be reduced by two orders of magnitude by using a sample with an optimum thickness. However, as the absorption coefficient is typically a function of the frequency, the optimum thickness is also a function of the frequency. Thus, a strategy for selecting the optimum thickness to suit the measurement purpose is also developed.

**Original contribution:** For the first time, it is proved with a rigorous arithmetical derivation that the thickness of a sample used in a transmission-mode THz-TDS measurement should be twice the absorption length in order to minimise the measurement uncertainty (Withayachumnankul *et al.* 2008a).

## 11.3 Part III—T-ray optics

### Quarter-wavelength antireflection coatings for T-rays: Chapter 9

**Background:** Energy loss by reflection becomes significant when the electromagnetic wave propagates through an interface between two dielectrics with a high contrast in refractive index, e.g. from air into a window. Nevertheless, little work to date has addressed this issue in the T-ray frequency range. Although the fundamentals of antireflection coatings can be borrowed from optics, some considerations regarding a coating material that has suitable dielectric properties and a fabrication method that can accommodate a desired coating thickness are necessary.

**Methodology:** A quarter-wavelength antireflection coating is exploited to reduce reflection. High-resistivity silicon is selected as a window material in the experiment as it demonstrates a high contrast in refractive index relative to the index of air. According to the antireflection theory, LDPE has its dielectric properties that are acceptable for coating a silicon window. On top of that, the mechanical properties of LDPE support the desired coating thickness, which is in the order of submillimetres. A frame is used to press coating layers against the window without adhesive.

**Result:** The experiment is carried out using a THz-TDS system operated in the transmission mode. The antireflection coating can effectively enhance the T-ray transmission of the window. However, the absorption at high frequencies of the coated window increases remarkably, probably due to impurities and/or grain sizes in the commercial-grade LDPE films. Furthermore, the characteristic matrix analysis shows that air gaps are present between the coating and the window, resulting in a deviation of the effective antireflection frequencies.

**Future work:** The antireflection performance can be improved by using a coating material that demonstrates a better index matching and lower absorption to T-rays. Better adhesion between the coating and the window offers a better control over the operational frequency of the coating. An improvement can also be expected from a variety of other antireflection coating theories, such as multilayer coatings, graded-index coatings, and metamaterial coatings, which have already been applied in other frequency ranges.

**Original contribution:** For the first time, the windows transparent to T-rays are fabricated to be antireflective based on the theory of quarter-wavelength antireflection (Withayachumnankul *et al.* 2007a).

### Quarter-wavelength multilayer interference filters for T-rays: Chapter 10

**Background:** It is foreseeable that in the near future the requirement for T-ray components, including filters, will increase rapidly following a higher demand for communication channels that will push carrier frequencies towards the subterahertz regime. To date, many types of filters have been realised for T-rays and nearby frequencies. A quarter-wavelength multilayer interference structure is another attractive option for T-ray filters due to its simplicity and functionality.

**Methodology:** Quarter-wavelength multilayer interference filters are designed for the operation in the T-ray frequency band. Two different dielectrics with a high contrast in refractive index and a high transparency are required for the construction of the filters. Float-zone intrinsic silicon and free space are selected in this regard, not only because of their suitable dielectric properties, but also their physical appearances. Both of the materials are put together alternately in the form of periodic layers, supported by a specially designed polymer frame. Their thicknesses are well controlled to encourage the interference in the T-ray frequencies.

**Result:** Measured by a transmission-mode THz-TDS system at a normal angle of incidence, the filter exhibits an apparent stop-band centred at a designated frequency. By increasing the number of layers, the attenuation inside the stop-band increases proportionally. Another consequence of an increment in the filter layers is the occurrence of the ripples in the pass-bands. These results reproduce well using the characteristic matrix calculation.

**Future work:** The spectral response of a quarter-wavelength multilayer interference filter is known to be periodic with respect to the frequency. Thus, this basic design may not be satisfactory when a more intricate frequency response is sought. An approach to modification of the filter response is available. By cascading a number of interference filters having different characteristics, i.e. different stop-band positions and widths, it is possible to create a desired spectral response. Moreover, other dielectrics may substitute for float-zone silicon in order to reduce the cost for high-volume production.

**Original contribution:** For the first time, the quarter-wavelength multilayer interference filters effective for T-ray frequencies are studied for their characteristics with respect to a particular structural parameter (Withayachumnankul *et al.* 2008d).